Department of Chemistry
Faculty of Science
University of Helsinki
Finland

Development of fast, reliable and automated isolation and fractionation methods for nanosized subpopulations of human biomacromolecules

Evgen Multia

DOCTORAL DISSERTATION

To be presented for public examination with the permission of the Faculty of Science of the University of Helsinki, in Chemicum Auditorium A110, A. I. Virtasen Aukio 1, on the 27th of August, 2021 at 12 o'clock.

Helsinki 2021

Supervisor

Professor Marja-Liisa Riekkola

Department of Chemistry

University of Helsinki

Finland

Reviewers

Professor Jonas Bergquist

Department of Chemistry - BMC

Analytical Chemistry

Uppsala University

Sweden

Professor Urpo Lamminmäki

Department of Life Technologies

University of Turku

Finland

Opponent

Ikerbasque Research Professor

Juan M. Falcón-Pérez

Center for Cooperative Research
in Biosciences (CIC bioGUNE)

Basque Research and
Technology Alliance

(BRTA, CIBERehd)

Spain

ABSTRACT

This doctoral thesis describes the development of fast, reliable and automated isolation and fractionation methods for nanosized subpopulations of human biomacromolecules. The focus of the study was on subpopulations of lipoproteins and extracellular vesicles (EVs) that are important in the detection of different diseases, such as atherosclerotic cardiovascular diseases and cancer, and may even possess therapeutic potential. In the thesis, immunoaffinity chromatography (IAC) with selective antibodies immobilized on the monolithic disk columns were utilized for the selective isolation of biomacromolecules from human plasma, while asymmetrical flow field-flow fractionation (AsFlFFF or AF4) was able to fractionate relevant subpopulations of biomacromolecules (e.g., small dense low-density lipoproteins, exomeres, and exosomes) from the isolates. Continuous flow quartz crystal microbalance (QCM) and partial filling affinity capillary electrophoresis (PF-ACE) were employed to study the affinity of the interactions between the antibody and lipoproteins.

The first step was to develop a method to study interactions between antibody and lipoproteins to select a high affinity antibody useful for the isolation of lipoprotein subpopulations by IAC. The interaction data obtained with PF-ACE was analyzed to determine the heterogeneity of the interactions with adsorption energy distribution calculations, while the QCM data was processed with interaction maps. The affinity constants obtained with QCM and PF-ACE agreed well with each other.

Next, the IAC methods were developed to capture EVs of different cellular origins from human plasma using anti-CD9 monoclonal antibody (mAb), while anti-CD61 mAb was exploited to capture platelet-derived EVs. The anti-apolipoprotein B-100 (anti-apoB-100) mAb was exploited to immunocapture apoB-100 containing lipoproteins. The anti-apoB-100 mAb was also characterized by the PF-ACE and QCM studies. Appropriate elution conditions were found for the IAC methods, which has often been an issue with magnetic beads-based immunoaffinity methods.

Since IAC allowed selective isolation of EVs and lipoproteins, a size-based separation to their subpopulations with AsFlFFF was introduced as a successive step. This enabled additional characterization of subpopulations by nanoparticle tracking analysis, western blotting, electron microscopy, capillary electrophoresis coupled with laser-induced fluorescent detection, zeta potential measurements, as well as free amino acids and glucose analysis with hydrophilic interaction liquid chromatography-tandem mass spectrometry.

Finally, IAC was successfully on-line coupled to AsFlFFF, resulting in quick and automated isolation and fractionation of the subpopulations of EVs and lipoproteins. The constructed IAC-AsFlFFF system was able to process reliably 18–38 samples in 24 h with only minor operator involvement, resulting in highly reproducible and gentle fractionation of EV subpopulations in the size range of exomeres and exosomes.

Polymeric monolithic disk columns were utilized for the first time for the IAC-based isolation of EVs and their subpopulations from human plasma, and for the detection of exomeres in CD9$^+$ EVs and CD61$^+$ platelet-derived EVs from human plasma samples. The results demonstrated that CD61$^+$ EVs are potentially taking part in gluconeogenesis based on free amino acids and glucose present as cargo.

PREFACE

First, I want to express my deepest gratitude to my supervisor, professor Marja-Liisa Riekkola, for seeing potential in me, offering me an opportunity to do research in a challenging and fascinating field, collaborate with excellent researchers, and visit interesting places. I thank you for the guidance and encouragement from the bachelor's level all the way to this day.

I would also like to thank all of the co-authors who helped with making this thesis possible. I have been lucky to have so many excellent people and researchers being part of this journey. Professor Torgny Fornstedt, Dr. Patrik Forssén, and Dr. Jörgen Samuelsson from Karlstad University are thanked for their long term collaboration with multiple articles and their hospitality in Sweden. Professor Aleš Podgornik is thanked for his invaluable help with monolithic disk columns and hospitality in Slovenia. Professors Myriam Taverna and Thanh Duc Mai, and Marco Morani are thanked for their collaboration and hospitality in France. Adj. Prof. Heli Sirén is thanked for her patient guidance, discussions, and teaching me how to work with capillary electrophoresis. Heli's support during the first years of the research was crucial. Adj. Prof. Matti Jauhiainen is thanked for his contributions and fruitful discussions regarding antibodies, affinity chromatography, lipoproteins, and other biomolecules. Jari Metso is thanked for his support in the laboratory and his help with size exclusion chromatography. Other members of Minerva Foundation Institute for Medical Research are thanked for their help as well. Adj. Prof. Katariina Öörni is thanked for her contribution, discussions, and help in the study of LDL as well as other lipoproteins. In addition, Dr. Maija Ruuth and other members of Wihuri Research Institute are thanked for their help. Adj. Prof. Marianna Kemell is thanked for the help with the electron microscopy. Adj. Prof. Pia Siljander, Dr. Mari Palviainen, and Dr. Sami Valkonen from the EV core facility are thanked for their contribution and introduction to the field of extracellular vesicles. Other co-authors, Dr. Karl Andersson, Marie Andersson, Dr. Zuzana Krupova, Pierre Defrenaix, Dr. Teodor Aastrup, Samuel Altun, Dr. Daniel Wallinder, and Linus Wallbing are also thanked dearly for their contributions.

Dr. Norbert M. Maier is thanked for his guidance, shared wisdom, and constant support for any research-related issues over the years. Norbert has contributed greatly to my education and to that I become a better scientist by constantly challenging and improving the experimental work, writing, and presentations.

Thanaporn Liangsupree is thanked for help and support during the years. Team working with you in laboratory, conferences, presentations, and writing have been pleasant and inspiring. You were an integral part of the completion of this thesis, and I am extremely happy that you were part of our research team.

Karina Moslova is thanked for the help with everything related to the laboratory and organizational aspects in the laboratory of analytical chemistry. Karina has been an unlimited source of positive and can-do attitude that she transferred to other colleagues. You have amazing organizational skills that helped with saving a lot of time. I am happy that I had an opportunity to work with you and thank you for your contribution and discussions.

Vantaa, July 2021

Evgen Multia

This thesis is dedicated to my son Leo.

TABLE OF CONTENTS

TABLE OF CONTENTS

LIST OF ORIGINAL PUBLICATIONS

This doctoral thesis is based on the publications listed below, hereafter referred to by their Roman numerals [I-IV]:

I   **Multia, E.**, Sirén, H., Andersson, K., Samuelsson, J., Forssén, P., Fornstedt, T., Öörni, K., Jauhiainen, M., Riekkola, M. L. (2017). Thermodynamic and kinetic approaches for evaluation of monoclonal antibody-lipoprotein interactions. *Analytical Biochemistry*, 518, 25-34. DOI: 10.1016/j.ab.2016.10.024

II   **Multia, E.**, Tear, C. J. Y., Palviainen, M., Siljander, P., Riekkola, M. L. (2019). Fast isolation of highly specific population of platelet-derived extracellular vesicles from blood plasma by affinity monolithic column, immobilized with anti-human CD61 antibody. *Analytica Chimica Acta*, 1091, 160-168. DOI: 10.1016/j.aca.2019.09.022

III   Morani, M., Duc Mai, T., Krupova, Z., Defrenaix, P., **Multia, E.**, Riekkola, M. L., Taverna, M. (2020). Electrokinetic characterization of extracellular vesicles with capillary electrophoresis: A new tool for their identification and quantification. *Analytica Chimica Acta*, 1128, 42-51. DOI: 10.1016/j.aca.2020.06.073

IV   **Multia, E.**, Liangsupree, T., Jussila, M., Ruiz-Jimenez, J., Kemell, M., Riekkola, M. L. (2020). Automated on-line isolation and fractionation system for nanosized biomacromolecules from human plasma. *Analytical Chemistry*, 92(19), 13058–13065. DOI: 10.1021/acs.analchem.0c01986

Contribution of the author

Experimental work related to capillary electrophoresis (Paper I), quartz crystal microbalance (Paper I), immunoaffinity chromatography (Papers II and III), and asymmetrical flow field-flow fractionation (Papers II and III). Design and development of the automated on-line isolation and fractionation system and related experimental work (Paper IV). The main responsibility for writing the manuscripts (Papers I, II, and IV) and writing the sections on immunoaffinity chromatography and asymmetrical flow field-flow fractionation (Paper III).

Publications and patent applications not included in the thesis

Gan, N., **Multia, E.**, Sirén, H., Ruuth, M., Öörni, K., Maier, N. M., Jauhiainen, M., Kemell, M., Riekkola, M. L. (2016). Tailor-made approach for selective isolation and elution of low-density lipoproteins by immunoaffinity sorbent on silica. *Analytical Biochemistry*, 514, 12-23. DOI: 10.1016/j.ab.2016.09.005

Forssén, P., **Multia, E.**, Samuelsson, J., Andersson, M., Aastrup, T., Altun, S., Wallinder, D., Wabring, L., Liangsupree, T., Riekkola, M. L., Fornstedt, T. (2018). Reliable Strategy for Analysis of Complex Biosensor Data. *Analytical Chemistry*, 90(8), 5366-5374. DOI: 10.1021/acs.analchem.8b00504

Liangsupree, T., **Multia, E.**, Metso, J., Jauhiainen, M., Forssén, P., Fornstedt, T., Öörni, K., Podgornik, A., Riekkola, M. L. (2019). New and rapid isolation of human LDL particles using monolithic disk columns with tandemly immobilized chondroitin-6-sulfate and anti-apoB-100 antibody. *Scientific Reports*, 9(1), 1-10. DOI: 10.1038/s41598-019-47750-z

Riekkola, M. L., **Multia, E.**, Jussila, M., Liangsupree, T. Method of fractionating a heterogeneous sample and apparatus for such a method. **European Patent Office**, Application number 20192643.3-1020. Patent filed on 25.08.2020. Application filed by Postnova Analytics GmbH.

Liangsupree, T., **Multia, E.**, & Riekkola, M. L. (2021). Modern isolation and separation techniques for extracellular vesicles. **Journal of Chromatography A**, 461773. DOI: 10.1016/j.chroma.2020.461773

LIST OF ABBREVIATIONS

ACE	Affinity capillary electrophoresis
AED	Adsorption energy distribution
AF4	Asymmetric flow field-flow fractionation
ApoB-100	Apolipoprotein B-100
AsFlFFF	Asymmetric flow field-flow fractionation
BGE	Background electrolyte
BSA	Bovine serum albumin
CE	Capillary electrophoresis
CDI	1'-carbonyldiimidazole
CFDA-SE	5-(and-6)-carboxyfluorescein diacetate succinimidyl ester
CHD	Coronary heart disease
CHES	2-(cyclohexylamino)ethanesulfonic acid
CIM	Convective interaction media
CVD	Cardiovascular diseases
Da	Dalton
DAD	Diode array detector
DLS	Dynamic light scattering
DMSO	Dimethyl sulfoxide
DNA	Deoxyribonucleic acid
EDMA	Ethylene glycol dimethacrylate
EDC-HCl	1-ethyl-3-(3-dimethylaminopropyl) carbodiimide hydrochloride
EOF	Electroosmotic flow
EVs	Extracellular vesicles
Exo	Exosomes
FESEM	Field emission scanning electron microscope
GMA	Glycidyl methacrylate
HDL	High-density lipoprotein
HEPES	4-(2-hydroxyethyl)-1-piperazineethanesulfonic acid
HILIC	Hydrophilic interaction liquid chromatography
HPLC	High-performance liquid chromatography
IAC	Immunoaffinity chromatography
IDL	Intermediate-density lipoprotein
ISTD	Internal standard
LC	Liquid chromatography
LDA	Linear discriminant analysis

LDL	Low-density lipoprotein
LIF	Laser-induced fluorescence
Lp(a)	Lipoprotein(a)
mAb	Monoclonal antibody
MALS	Multiangle light scattering
MBD	4-(4-methoxybenzylamino)-7-nitro-2,1,3-benzoxadiazole
MS	Mass spectrometry/meter
MS/MS	Tandem mass spectrometry/meter
MVBs	Multivesicular bodies
MW	Molecular weight
Na_2EDTA	Ethylenediaminetetraacetic acid disodium salt dehydrate
NTA	Nanoparticle tracking analysis
P2VP-b-PEO	Poly(2-vinylpyridine)-block-(ethylene oxide)
PF-ACE	Partial filling affinity capillary electrophoresis
pAb	Polyclonal antibody
PBS	Phosphate buffered saline
PCA	Principal component analysis
RNA	Ribonucleic acid
RFU	Relative fluorescence units
sdLDL	Small dense low-density lipoprotein
SDS	Sodium dodecyl sulfate
SEC	Size-exclusion chromatography
SEM	Scanning electron microscope
SPR	Surface plasmon resonance
Sulfo-NHS	N-Hydroxysulfosuccinimide sodium salt
TEM	Transmission electron microscopy
Tris	Tris(hydroxymethyl)aminomethane
TSG101	Tumour susceptibility gene 101 protein
TWEEN 20	Polyoxyethylene (20) sorbitan monolaurate
QCM	Quartz crystal microbalance
UC	Ultracentrifugation
UF	Ultrafiltration
UV	Ultraviolet
VLDL	Very-low-density lipoprotein

LIST OF SYMBOLS

A	Eddy diffusion [m]
B	Diffusion in longitudinal direction [m^2 s^{-1}]
B_0	Hydraulic permeability [m s^{-1} Pa^{-1}]
C	Analyte concentration in the running buffer [M]
C_s	Mass sensitivity constant [kg Hz^{-1}]
C_r	Mass transfer resistance coefficient [s]
d	Hydration diameter of analyte [m]
d_p	Particle diameter [m]
D_m	Diffusion coefficient of analyte in the mobile phase [m^2 s^{-1}]
ε_b	Porosity in the monolithic column
Δf	Frequency change of the oscillating crystal [Hz]
$\Delta G°$	Gibbs free energy [J mol^{-1}]
H	Theoretical plate height [m]
ΔH	Enthalpy term [J mol^{-1}]
I	Ionic strength [M]
k	Boltzmann constant [1.38*10^{23} J K^{-1}]
k_a	Association rate constant [M^{-1} s^{-1}]
k_d	Dissociation rate constant [s^{-1}]
k_r	Retention factor
K_A	Association equilibrium rate constant [M^{-1}]
K_D	Dissociation equilibrium rate constant [M]
K_d	Dissociation constant [M]
λ	Factor for shape of material packing
L	Column length [m]
$L_{channel}$	Channel length [m]
L_{det}	Length to detector [m]
L_{tot}	Total capillary length [m]
μ	Dynamic viscosity of the fluid [Pa s]
μ^A	Average mobility of the complex [m^2 V^{-1}s^{-1}]
μ_b	Mobility of bound molar fraction of analyte [m^2 V^{-1}s^{-1}]

μ_f	Mobility of free molar fraction of analyte [m^2 V^{-1}s^{-1}]
μ_{tot}	Total mobility of analyte [m^2 V^{-1}s^{-1}]
μ_{ep}	Electrophoretic mobility of analyte [m^2 V^{-1}s^{-1}]
μ_{eo}	Eletroosmotic mobility [m^2 V^{-1}s^{-1}]
Δm	Change in mass on the surface of quartz crystal [kg]
n	Molar amount of the receptor [mol]
η	Dynamic viscosity of the carrier liquid [Pa s]
θ	Fractional surface coverage
Θ_b	Bound fraction of analyte
Θ_f	Free fraction of analyte
ΔP	Pressure drop difference across the monolithic column [Pa]
r	Inner radius of the capillary [m]
R	Gas constant [8.314 J mol^{-1} K^{-1}]
ΔS	Entropy term [J mol^{-1} K^{-1}]
T	Temperature [K]
$t_{0,det}$	Time that analyte needs to reach detector when receptor is not present [s]
t_m	Migration time of analyte [s]
Δt_m	Changes in migration times [s]
u_f	Flow velocity [m^3 s^{-1}]
u	Linear velocity [m s^{-1}]
V	Voltage utilized in the separation [V]
V_a	Axial flow rate [m^3 s^{-1}]
V_c	Cross flow rate [m^3 s^{-1}]
V_{inlet}	Inlet flow rate [m^3 s^{-1}]
V_{outlet}	Outlet flow rate [m^3 s^{-1}]
w	Channel thickness [m]
z'	Focusing point from the channel inlet
γ	Obstruction factor

1. INTRODUCTION

Human biomacromolecules such as extracellular vesicles (EVs) and lipoproteins are heterogeneous nanosized particles that have a crucial role in several physiological and pathological processes, and hence useful in therapeutic and diagnostic applications. EVs have shown potential in cancer diagnosis, and as well as in the diagnosis of angiogenesis, immune response, cardiovascular, and neurodegeneration related diseases.[1] In addition, EVs have the ability to reach specific cells by passing e.g., inter-endothelial junctions or the blood-brain-barrier, and release the cargo inside these cells[2,3] leading to their therapeutic potential in e.g., drug delivery. In addition, EVs of specific origin, such as platelet-derived EVs, have been found to take part in many diseases.[4–6] These EVs are involved in the immune system, inflammation, hemostasis, and thrombosis together with platelets,[7,8] and hold potential to be utilized in therapeutics and diagnostics of various diseases e.g., bleeding disorders, cancer, cardiovascular-related diseases, and wound healing.[8–11] Lipoproteins, on the other hand, play an important role in the development of atherosclerosis. Atherosclerosis develops in the primary phase when low-density lipoprotein (LDL) is retained and accumulated to arterial walls.[12,13] But even within LDL there are subclasses, such as small-dense LDL (sdLDL), that have been found to associate with metabolic disorder,[14] and have an even higher atherogenic effect compared to LDL subclasses with bigger size.[15] New advanced methods and techniques are needed to isolate this kind of specific subclasses/populations that are currently not feasible with conventional isolation techniques from complex biofluids. Multiple limitations of conventional isolation techniques, such as density-based ultracentrifugation (UC), limit their use, but it is also possible to utilize size-, charge-, and affinity-based techniques. Nonetheless, there is a great need for new time-effective, easy-to-operate methods/techniques that have control of the final product. In addition to purity, it is also important to preserve the integrity of the biomacromolecules that tend to be fragile. For more complex biomacromolecules such as EVs, even combination and hyphenation of multiple techniques are necessary to produce subpopulations of adequate purity. The conventional techniques (e.g. UC) have large intra- and inter-batch variations, especially when isolating EVs.[16] Additionally, the UC is expensive, time-intensive, and tedious due to a large amount of manual labor, and has been known to contaminate the EV isolates with lipoproteins and other proteins. This is unacceptable in the therapeutic applications where the isolation technique should be able to handle complex biofluids,

scalable, reliable, and automated, and produce reproducible subpopulations of known characteristics.[16,17]

Immunoaffinity chromatography (IAC) has the advantage of being selective for specific analytes due to the high affinity of antibodies towards the antigen. The IAC with polymeric monolithic columns can overcome the limitations of other affinity-based methods (e.g. magnetic beads) to handle complex biofluids, such as plasma. The polymeric monolithic columns offer a wide pH range stability and reusability. Quartz crystal microbalance (QCM) and partial filling affinity capillary electrophoresis (PF-ACE) are useful tools for screening the suitable ligand candidates and obtaining information on the interactions between the antibody and the analytes. The size-based separation of biomacromolecules by asymmetrical field-flow fractionation (AsFlFFF) gives flexibility with modifiable and optimizable cross-flow that size-exclusion chromatography (SEC) does not have. In AsFlFFF the fractionation parameters can be modified even between runs, while in SEC this would require changing the entire column. Moreover AsFlFFF handles biomacromolecules in a gentle way due to the lack of shear forces from the stationary phase present in the SEC, thus preserving their fragile integrity. The buffer can be exchanged in the AsFlFFF to formulation buffer, which is especially important when producing fractions of biomacromolecules for therapeutic purposes. The AsFlFFF has been also useful in discovering new subpopulations of EVs such as exomeres.[18]

The main objective of this doctoral thesis was to develop fast and easily automated methods/techniques for the reliable isolation of subpopulations of biomacromolecules (EVs and lipoproteins) from minute human plasma volume and to study specific antibody-antigen interactions needed for the isolation.

The specific aims of the thesis were:

- To exploit PF-ACE and QCM to study interactions between anti-apoB-100 monoclonal antibody and apoB-100 containing lipoprotein subpopulations. (**Paper I**)

- To develop a monolithic IAC method to isolate platelet-derived (CD61$^+$) EVs in the size range of exomeres and exosomes. (**Paper II**)

- To compare the monolithic IAC disks immobilized with anti-CD9 and anti-CD61 to UC and SEC as EV isolation techniques. (**Paper III**)

- To utilize AsFlFFF coupled with multiple detectors to study and fractionate exomere and exosome sized EVs pre-isolated with IAC. (**Papers II-IV**)

- To obtain lipoprotein-free EV subpopulation isolates. (**Papers II-IV**)

- To develop an automated on-line IAC-AsFlFFF system for isolation and fractionation exomere and exosome sized EVs, and apoB-100 containing lipoprotein subpopulations. (**Paper IV**)

- To study metabolite (amino acid and sugar) composition of CD9$^+$ and CD61$^+$ EV subpopulations in the size range of exomere and exosome. (**Paper IV**)

2. BACKGROUND TO THE WORK

2.1 Modern techniques in the isolation, separation, and fractionation of human biomacromolecules

This section describes current modern techniques in the isolation, separation, and fractionation of human biomacromolecules. Biomacromolecules can be isolated with different techniques (Figure 1), e.g., with density-based techniques such as ultracentrifugation,[19–22] affinity-based techniques (magnetic particles[23–25] and affinity chromatography[26]), charge-based techniques (cyclical electrical field-flow fractionation,[27,28] ion-exchange,[29,30] ion concentration polarization,[31] electrophoresis,[32,33] and dielectrophoresis[34,35]), size-based techniques (field-flow fractionation,[36–38] filtration,[39–44] deterministic lateral displacement pillar arrays,[45–47] size-exclusion chromatography (SEC),[48–51] and viscoelastic microfluidic systems[52]), microfluidic platforms,[53] acoustic trapping techniques,[54–56] precipitation,[57,58] and hydrophilic interaction chromatography[59,60] from a variety of different body fluids.
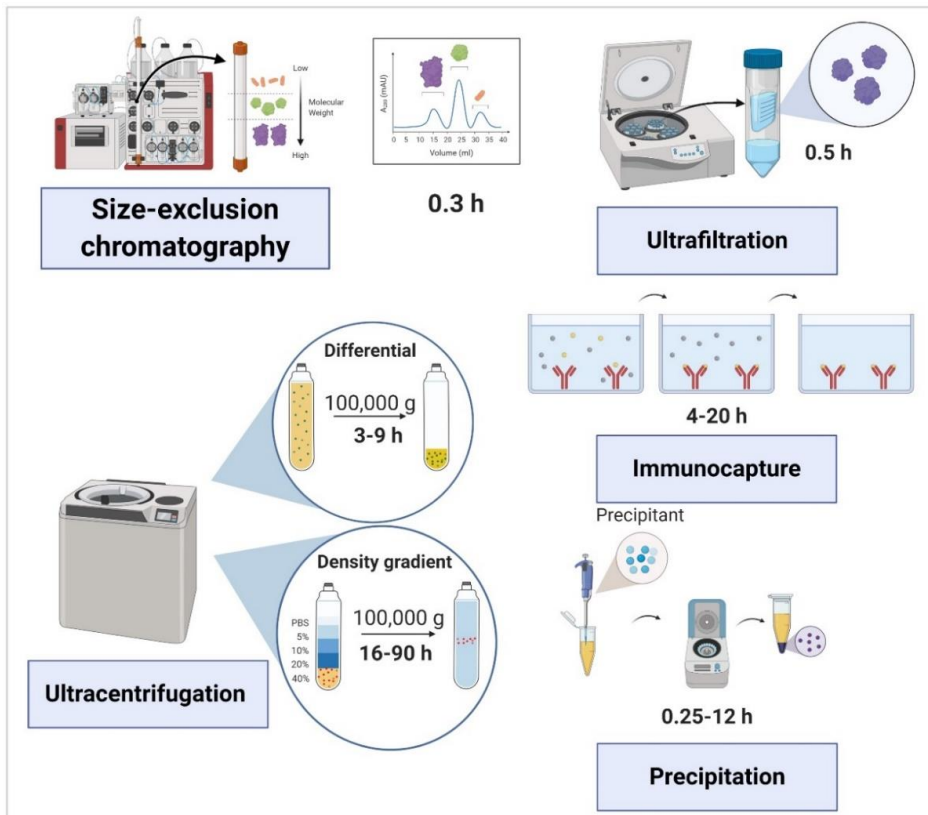
Figure 1. Most common techniques utilized in the isolation biomacromolecules (EVs) and the expected time needed for the isolation. Adapted from [61].

Due to overlapping sizes and densities of the biomacromolecules (e.g., in the case of lipoproteins and extracellular vesicles, and retroviruses, Figure 2), it is often not possible to isolate pure subpopulations of human biomacromolecules with a single technique, thus requiring a combination of techniques.[36,37,62–64] The "golden standard" technique for the isolation of many biomacromolecules is density-based separation with ultracentrifugation. However, the centrifugation has many limitations, such as high cost, time consuming, need for skillful operators and tedious manual labor, prone to batch to batch irreproducibility, and production of a lot of waste. Accordingly it is obvious that there is a need for more automated, fast, selective, and scalable modern techniques.
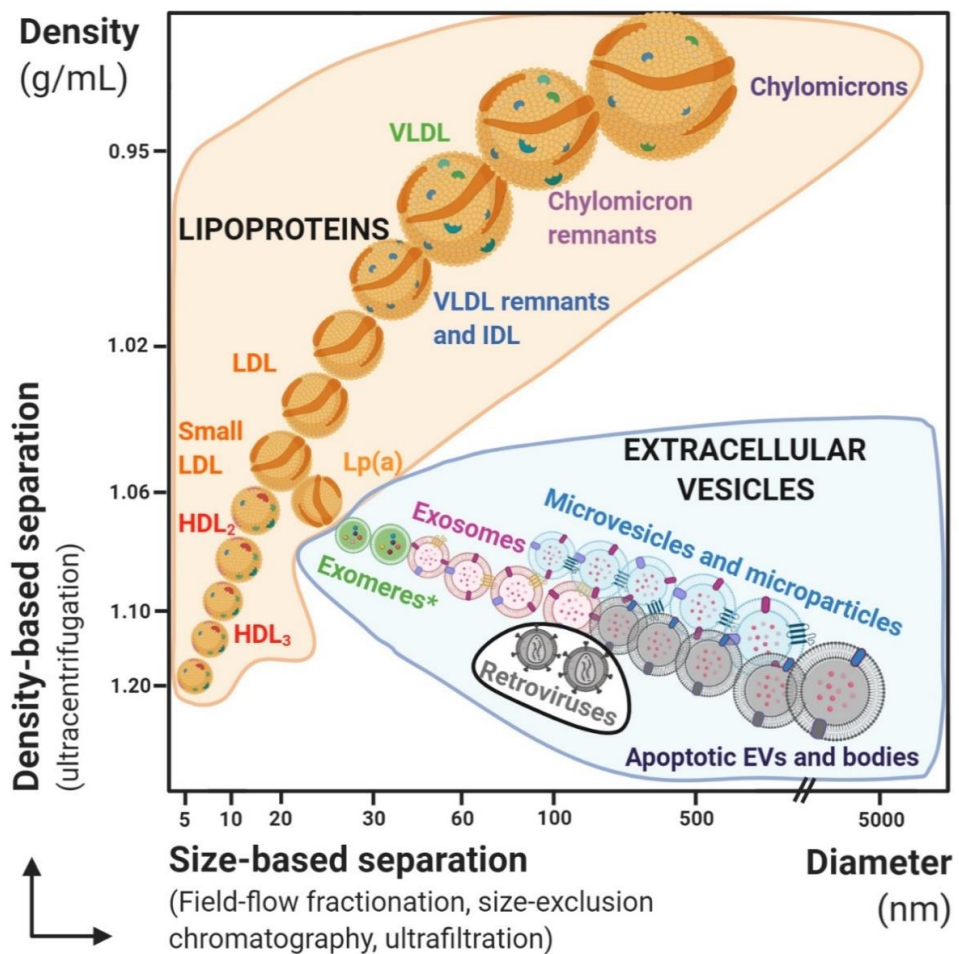
Figure 2. Size and density of different subtypes of EVs, lipoproteins, and retroviruses. The density of exomeres has not yet been determined *. Adapted from [65–67].

Fast and selective isolation of biomacromolecules can be achieved with affinity-based separation techniques such as affinity chromatography. In the affinity chromatography the binding ligand is immobilized to the stationary support.[68,69] The ligand utilizes biological interactions to selectively capture its counterpart (e.g., enzyme captures substrate, antibody captures antigen in immunoaffinity, or vice versa).[68,70,71] Most commonly, the bound biomolecules can be released with non-specific elution by changing the pH of the mobile phase.[68,70] The first specific isolation of an enzyme and its substrate date as early as 1910, when Emil Starkenstein was purifying α-amylase.[70,72,73] The field continued to evolve in the 1930s with purification of antibodies.[72,74–76] In the 1960s other important biomacromolecules such as transfer RNA,[77] nucleotides,[78] strands of nucleic acid,[79] and nuclease[80] were purified. After the first appearance of the term affinity chromatography in 1968,[80] more than 50,000 papers have been published including this term, with the most active growth period being from 1968-90.[26]

Different support materials can be used in the affinity chromatography, e.g., agarose, cellulose and other carbohydrate supports, silica, and a variety of organic polymers such as polymethacrylate and polystyrene.[70] The correct selection of support material is crucial for the isolation of biomacromolecules, since all of the materials have some advantages and disadvantages. Agarose and organic polymers have a wide operating pH range and biocompatibility that for example silica-based supports do not have without the chemical modification of their surface. However, opposite to agarose, silica-based materials have mechanical stability that can be utilized in high performance liquid chromatography (HPLC).[26,70] Over the last 20 years, monolithic supports have increased their popularity in the affinity chromatography and have significant advantages in isolation of biomacromolecules compared to particulate supports.[70,81–85] Especially polymer-based monoliths (ethylene glycol dimethacrylate (EDMA) and glycidyl methacrylate (GMA)), offer good separation efficiency, permeability, low back pressures, and can be utilized for isolation of e.g., viruses and DNA.[70,86–91]

The most applied form of bioaffinity chromatography has been immunoaffinity chromatography (IAC).[26,92–94] Due to strong interactions between the antibody and antigen, it is possible to isolate molecules even from complex biofluids.[70,95–102] For example, combining silica monoliths with the IAC has resulted in successful isolation of CD9+ EVs from human serum samples of lung cancer patients.[103] In this system, monoliths immobilized with antibodies were placed in the pipette tip, and the system could isolate one sample/tip in 30 minutes. In addition, even the 96-well plate format

including the combination of the IAC and monoliths has been used to isolate transferrin from plasma samples up to 20 times/monolith.[104]

The concept behind field-flow fractionation (FFF) was first published in 1966[105] by J.C. Giddings for the separation of macromolecules and colloids. The first publication was followed by many variations of FFF: such as electrical, flow, sedimentation, and thermal. The flow field-flow fractionation (FlFFF) variation (published in 1976[106,107]) has become the most popular and versatile variant. In the FlFFF the cross flow perpendicular to the main flow creates the hydrodynamic field that results in separation of macromolecules based on the differences in their diffusion coefficients.[108,109] The FlFFF has an advantage in being able to utilize almost any solution as a mobile phase, and can be divided into symmetrical and asymmetrical (AsFlFFF/AF4) subtechniques. The AsFlFFF, first published in 1986,[110,111] was actively developed during the following years, and has become the most popular subtechnique since.

The channel in the AsFlFFF consists of two plates separated by a spacer. A permeable membrane at the bottom plate is called accumulation wall.[66,112] The macromolecules are carried by a parabolic flow profile from the channel to detectors and biomacromolecules get separated by the perpendicular cross-flow. The size-based separation of biomacromolecules by the AsFlFFF is more flexible compared to e.g., SEC due to easily modifiable and optimizable cross-flow. Modifications can be done even between runs, while in the SEC this would require changing the entire column.[66] The small biomacromolecules (high diffusion coefficient) remain further from the bottom of the channel, while larger biomacromolecules stay closer to the accumulation wall. Thus in normal mode, smaller biomacromolecules arrive first to the detectors followed by larger ones that is opposite to the order of arrival in the SEC.[66] The advantage of the AsFlFFF for the separation of biomacromolecules is its gentle fractionation, due to lack of shear forces from stationary phase (present in the SEC) deteriorating the fragile biomacromolecules. With the AsFlFFF it is also possible to exchange buffer to formulation buffer, which is important for fractionation of biomacromolecules for therapeutic purposes.[66] The disadvantage of the AsFlFFF might be the dilution of the samples, however this is also the case with the SEC. Another limiting factor, when large volumes need to be processed, might be small quantities of the sample that can be processed due to overloading effects and problems with self-association.[66]

The AsFlFFF has been extensively utilized to study different biomacromolecules such as bovine serum albumin (BSA),[113] DNA,[114] EVs,[18,36,37,112,115–119] ferritin,[120] globulins,[121] lipoproteins,[122] liposomes,[123,124] plasmids,[125] ribosomes,[126] and viruses.[114,120] The EVs have been commonly fractionated utilizing 10 kDa regenerated cellulose membrane and a 350 μm spacer.[66] Zhang et al. [18] discovered an EV subpopulation called exomere utilizing the AsFlFFF in 2018.

Capillary electromigration techniques consist of capillary electrophoretic techniques and electrically driven capillary chromatographic techniques, depending on separation principles. In some cases, these principles are overlapping. These techniques have advantages in high speed, separation selectivity and efficiency, low amount of sample and reagents needed, mass sensitivity, and applicability to microchannel structures.[127–129] Many techniques have been especially useful for the separation and study of biomacromolecules.[130–139] However, the inner wall of fused silica capillary often need to be modified to prevent unwanted adsorption of analytes and sample matrix components, and to eliminate or control electro-osmotic flow.[140–146] This can be done by masking silanol groups of the capillary by coatings (dynamic or covalent), ionic strength, and extreme pH of background electrolyte (BGE).[138,147–149] Polymeric coatings often also increase the repeatability and efficiency of the separation of biomacromolecules.[138,149–153]

In partial filling affinity capillary electrophoresis (PF-ACE) it is possible to analyze samples without immobilizing the ligand, and it also consumes less sample and reagents compared to traditional affinity chromatography. PF-ACE provides relatively fast analysis, and in many cases does not require pre-purified samples.[154,155] The PF-ACE has been successfully utilized to estimate binding constants of complexes[154–158] of different biomacromolecules such as lipoproteins.[135,137,138,159] PF-ACE combined with adsorption energy distribution (AED) calculations offers additional information on the strength and heterogeneity of the interactions.[160–165]

Binding studies can also be conducted with optical or acoustic biosensors. The first enzyme electrode-based biosensor was introduced by L.C. Clark already in 1962.[166] Surface plasmon resonance (SPR) is an optical biosensor with mass sensitivity of pg/mm^2, while quartz crystal microbalance (QCM) has a mass sensitivity of fg/mm^2.[167–169] In addition to high mass sensitivity, the QCM can sense changes in viscoelastic properties and charges of complexes, and allows the possibility to study cell adhesion. QCM can elucidate interactions from weak to high affinity[133,170] and it can be utilized to study the antibody-antigen interactions. With the QCM it is also

possible to study very large biomacromolecules and lipid membranes, viruses, bacteria, and even whole cells.[171–174]

The focus of my study was to develop new methods to isolate, separate, and fractionate pure subpopulations of biomacromolecules, applicable for therapeutic and diagnostic purposes. The emphasis was given to immunoaffinity-based methods due to their selectivity, the size-based fractionation with the AsFlFFF, and the charge-based separation with CE. Combined methods utilizing different separation principles were needed due to heterogeneity and overlap of the biomacromolecule subpopulations in their sizes and densities (Figure 2). Obtaining pure subpopulations of biomacromolecules is important because of the disease promoting nature of specific subpopulations over others. Information on the concentration levels and the composition of the subpopulations can be beneficial for prevention and early detection of different diseases. In addition, subpopulations with high purity can be utilized e.g., in targeted drug delivery.

2.2 Lipoproteins

The main function of lipoproteins is to transport cholesterol, triglycerides, and phospholipids in circulation and other extravascular body fluids. Major lipoprotein subpopulations include high-density lipoprotein (HDL), LDL, lipoprotein(a) (Lp(a)),[175] intermediate-density lipoprotein (IDL), very-low-density-lipoprotein (VLDL), and chylomicrons. Their structures, sizes, and densities are collected in Figures 2 and 3. In addition, the lipoproteins have integrated apolipoproteins (e.g., A, B-100, C, E, and J) that are involved in metabolism and binding of the lipoproteins to receptors for uptake and release.[176,177] For example, LDL contains 80 % lipids and 20 % protein called apolipoproteinB-100 (apoB-100), which is the major apolipoprotein found in the LDL. ApoB-100 is a very hydrophobic biomacromolecule of a size of 512 kDa that is synthesized in the liver.[178,179] Targeting the apolipoproteins in affinity chromatography will result in specific isolation of subpopulations of lipoproteins containing these apolipoproteins.

phospholipid monolayer

apoB-100

free cholesterol

Lipid core:
cholesterol esters
triglycerides

B-100

B-100, E

Associated apolipoproteins	A-I, A-II, A-IV, C-I, C-II, C-III, J		B-100		B-100, E		A-IV, B-100, C-I, C-II, C-III, E

	7-12 nm **HDL**	18-25 nm **LDL**	25-35 nm **IDL**	30-90 nm **VLDL**
Density (g/mL)	1.063-1.210	1.019-1.063	1.006-1.019	0.95-1.006
Protein composition (% mass/mass)	44	20	18	6
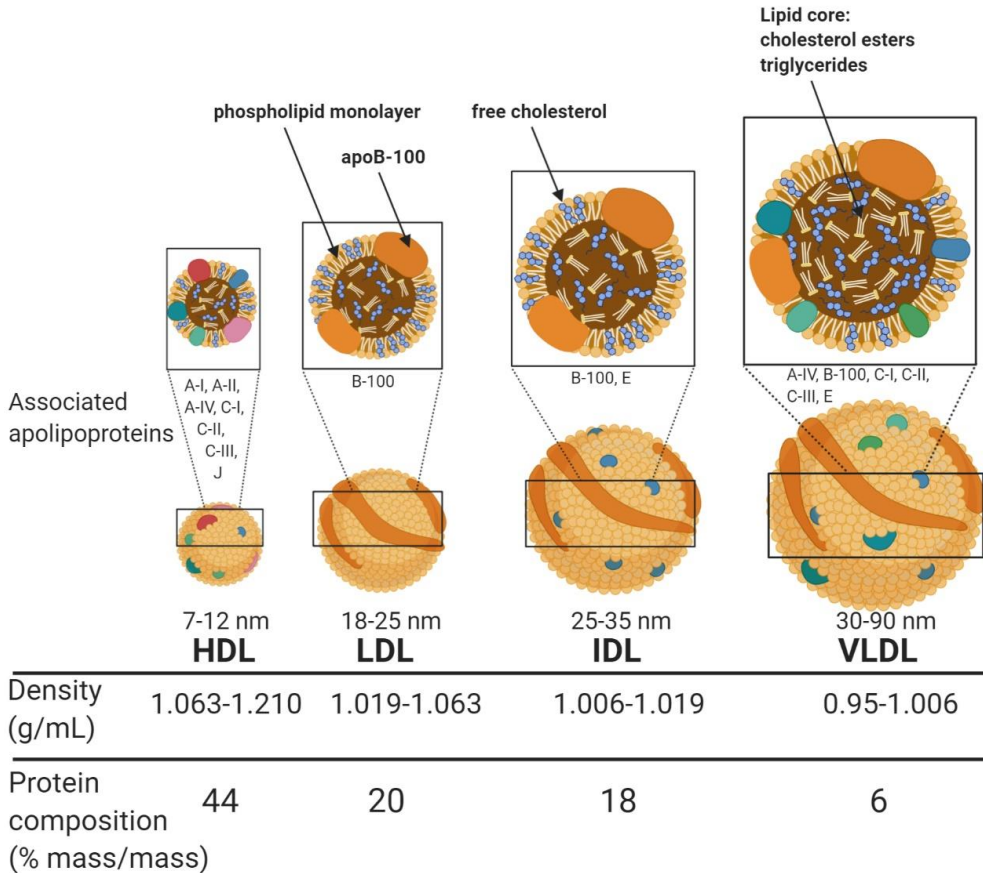
Figure 3. Major lipoprotein subpopulations in human plasma and their properties.

Lipoproteins play an important role in the development of atherosclerosis. The atherosclerosis develops when LDL is retained and accumulated to arterial walls.[12,13] But even within LDL there are subclasses, such as small dense LDL (sdLDL), that have been found to associate with metabolic disorder,[14] and have an even higher atherogenic effect compared to other larger LDL subclasses.[15] However, in the formation of atherosclerosis, not only the size of the LDL matters, but also its concentrations.[180] High concentrations in the blood lead to higher accumulation probability on the intima walls. After accumulation, the LDL can undergo changes due to enzymatic activity and oxidation, leading to aggregation and fusion.[181] Subsequently macrophages form atherogenic foam cells,[182] which together with inflammation, contribute to the progression of the disease.[183,184] Highly atherogenic and proinflammatory LDL complexes have often undergone desialylation, obtained

negative charge, and oxidized.[15] The sdLDL has a favorable size for penetrating the arterial wall in addition to prolonged circulation time that increases the probability for modifications of the sdLDL particle.[15,185,186] Cardiovascular diseases (CVDs) have been shown to correlate with sdLDL and elevated sdLDL cholesterol.[187–191] It has been also demonstrated that sdLDL cholesterol is a better biomarker compared to total LDL cholesterol for coronary heart disease (CHD) in nondiabetic, prediabetic, and type 2 diabetic individuals.[192–194] In addition to atherosclerosis, the elevated sdLDL concentrations have been linked to metabolic syndrome, diabetes, dyslipidemia, and even to chronic kidney disease.[195–199]

2.2.1 LDL subclasses

LDL can additionally be subdivided into 4 subclasses (Table 1), of which small LDL III and very small LDL IV[200,201] can be considered sdLDL. However, direct comparison of the subclasses and their characteristics among different isolation methods is problematic. LDL III is, for example, defined with UC methods to have a density of 1.028-1.060 g/mL, with a stricter limit being 1.028-1.044 g/mL, since LDL IV has been considered to start from 1.044-1.060 g/mL. Based on electrophoretic mobilities measured with gradient gel electrophoresis the size of sdLDL has been determined to be 22-25.74 nm, where 22-24.1 nm was the size limit of LDL IV and 24.2-25.5 nm that of LDL III. Similar size ranges have also been found with HPLC gel filtration, where LDL III was 20.7-23 nm and 16.7-20.7 nm for LDL IV. With ion mobility measurements and NMR, the size of sdLDL has been attributed to a size range of 18-21 nm, but direct comparisons to the gradient gel electrophoresis is not possible.[15]

It has been shown that for sdLDL it takes a longer time before it is cleared from the circulation via LDL receptor.[202,203] In addition to the longer circulation times, modified LDL particles (electronegative, desialylated, glycated, and oxidized) have an increased atherogenicity due to increased aggregation and complex formation probability.[204,205] The sdLDL particles are more glycated and more susceptible to oxidation due to their different lipid composition and lower concentrations of vitamins that have antioxidative properties. The desialylation of the sdLDL increases the time of attachment to the arterial wall.[206–210]

Table 1. Characteristics of the LDL subpopulations based on density, size, and current separation methods. Adapted from[15]. NA - not applicable.

Method	LDL I Large	LDL II Intermediate	Small dense LDL	
			LDL III Small	LDL IV Very small
Ultracentrifugation Density gradient[189] [g/mL]	1.019–1.023	1.023–1.034	1.034–1.044	1.044–1.060
Density gradient[211] [g/mL]	1.025–1.034	1.034–1.044	1.044–1.060	
Iodixanol gradient[212] [g/mL]	1.016–1.028	NA	1.028–1.043	NA
Iodixanol gradient[213] [g/mL]	1.022–1.028		1.028–1.041	
Gradient gel electrophoresis[214] [nm]	26.35–28.5	25.75–26.34	22.0–25.74	
Gradient gel electrophoresis[215] [nm]	26.0–28.5	25.5–26.4	24.2–25.5	22.0–24.1
HPLC – gel filtration[216] [nm]	25.5–28.6	23–25.5	20.7–23.0	16.7–20.7
DLS[217] [nm]	21.5 ± 0.8		20.3 ± 1.1	
Ion mobility[218] [nm]	21.9–23.8	21.1–21.9	20.17–21.1	18.0–20.17
NMR[219,220] [nm]	21.3–22.7	19.8–21.2	18.3–19.7	NA
NMR[221] [nm]	20.6–22.0	20.4–20.5	19.0–20.3	
Homogenous assay[222,223] [g/mL]	NA		1.044–1.063	

2.3 Subpopulations of extracellular vesicles

Extracellular vesicles (EVs) are heterogeneous populations of nanosized membrane-enclosed particles (30-5000 nm) released by most cell types that do not replicate.[224] EVs can be found in cellular microenvironment and the circulation[225], as well as in amniotic fluid, breast milk, cerebrospinal fluid, feces, saliva, semen, and urine.[226] Ectosomes (e.g., micro- and large vesicles, and microparticles) are EVs of ~50-1000 nm that bud out from the plasma membrane, while exosomes (~50-150 nm) are EVs of endosomal origin[1,65], making size-based differentiation of EV subclasses in the isolates highly challenging due to size overlap. Exomeres (~30-50 nm) are a newly discovered particle type[18] that do not have a lipid bilayer, and still unknown biogenesis. However, the results suggest that the biogenesis is associated with the cell's metabolism since the inner cargo of exomeres has been found to contain proteins from endoplasmic reticulum, microtubules, and mitochondria that are involved in glycolysis and mTORC1 metabolic pathways.[18,227] Biogenesis and size ranges of different EVs subtypes are depicted in Figure 4.

The biogenesis of the exosomes involves inward budding of endosomal membranes inside multivesicular bodies,[226–228] which also store[229] the exosomes before they are released outside. The secretion outside the cell happens when the multivesicular bodies merge with the plasma membrane and release the exosomes outside in a process called exocytosis.[226]

The biogenesis of microvesicles or ectosomes on the other hand involves budding from the surface of the plasma membrane, but the microvesicles may still have a different membrane composition compared to the surface, indicating that the biogenesis is not a random event, and that some regulation of the process may take place.[226,229] Since the size ranges of the exosomes (Figure 5) and the microvesicles overlap in the region of 50-150 nm, the differentiation of these EVs with only density- and size-based techniques is not possible.[66] Selective isolation of the EVs of the exosomal size range by affinity chromatography should target common exosomal surface markers such as tetraspanins (CD9, CD63, and CD81).
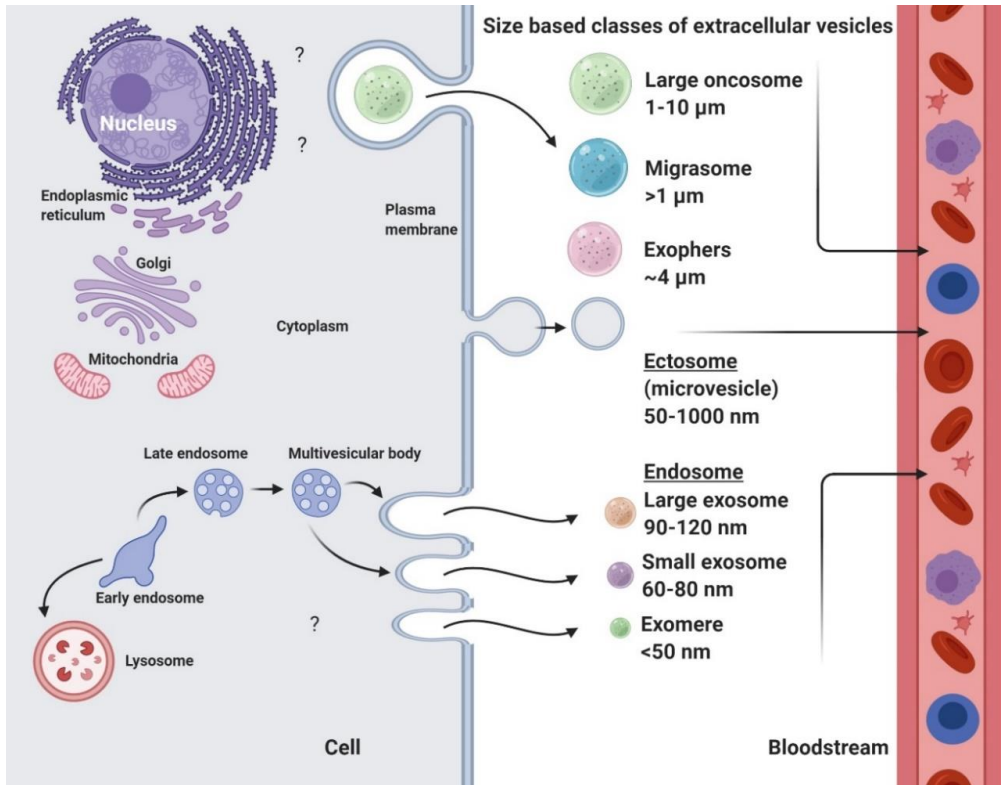
Figure 4. Size-based classes of extracellular vesicles and their biogenesis. Exomere is a newly discovered particle with still unknown biogenesis. Larger vesicles (oncosome, migrasome, exophers) also have unknown biogenesis. The bioactive cargo material of EVs can be from cytoplasm, endoplasmic reticulum, Golgi, mitochondria, nucleus, and plasma membrane depending on their cellular origin. Adapted from [227,228].

Exosomes and EVs in general, isolated for diagnostic purposes, do not need to be of high purity, since the primary goal is to obtain sufficient amount of the biomarker to enable detection or quantification. For therapeutic purposes such as cellular programming, drug delivery, or immunotherapy it is important to have intact, pure, and well-defined subpopulations. EVs carry nucleic acids (RNAs), mediator molecules, and other metabolites to cells and release the cargo upon internalization by the cell,[230] and in this way take part in cell-to-cell communication.[230] The cargo provides a signature of the cell that the EVs originated from, and if this cell is pathologic, it can possibly be detected from the EVs.[226] Thus, cancer-associated material carried by the EVs can be utilized for the development of non-invasive

diagnosis and prognosis of tumor progression and stage of cancer.[65,231] As one potential option to stop the progression of cancer, it has been suggested that tumor-derived EVs could be removed from the patient.[232] However, EVs are not only limited to the cancer diagnosis, as they also have diagnostic potential for angiogenesis, immune response, cardiovascular, and neurodegeneration-related diseases.[1] The therapeutic potential of EVs relies on their ability to reach specific cells by passing e.g., inter-endothelial junctions or the blood-brain-barrier, and release the cargo inside these cells.[2,3]
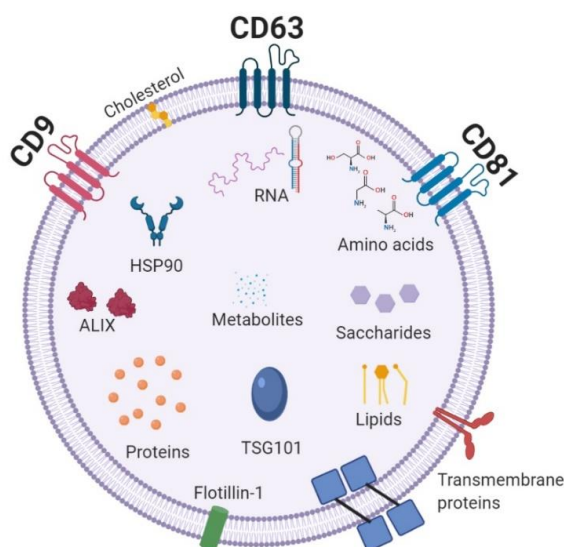
Figure 5. Structure and cargo of an exosome. Adapted from [1].

2.3.1 Platelets and platelet-derived extracellular vesicles

The main function of platelets is to take part in hemostasis and thrombosis, but they are also involved in innate and adaptive immunity, regulation of inflammation, nervous system-related diseases, and cancer. Platelets are non-nucleated particles of 2-5 µm that may carry granule structures (α- and δ- granules), lysosomes, mitochondria, and open canalicular system.[233–236] The multivesicular bodies are the source of origin for α- granules, while δ- granules and lysosomes originate from late endosomes, and upon platelet activation α- and δ- granules release their content by fusing to the surface of the platelet.[237–239] Platelet surface proteins such as CD9,

CD63 (tetraspanins), CD41/61 (integrin αIIbβ3),and glycoprotein VI are also found in the α- granules.[239]

Activated and aging platelets release platelet-derived EVs, which also contain heat shock proteins, integrin CD41/61, as well as tetraspanins CD9, CD63, and CD81.[7,240–243] Platelet-derived EVs work together with platelets in coagulation, and they are by concentration one of the most abundant EVs in human blood with even further concentration increase after platelets get activated.[7,244–246] They are involved in multiple physiological and pathological conditions such as autoimmune diseases, angiogenesis and CVD, cancer, cellular communication, hemostasis and thrombosis.[7,240] Thus the therapeutic and diagnostic potential of platelet-derived EVs could be e.g., in bleeding disorders, cancer, cardiovascular-related diseases, and wound healing.[8–11]

Exosome-sized platelet-derived EVs share common protein markers and proteome with α- granules, leading to a hypothesis that platelet α-granules are the source of platelet-derived EVs.[7,245,247,248] Different compositions of lipid mediators or mitochondrial proteins of larger platelet-derived EVs indicate that they are separate populations with different functions compared to exosome-sized platelet-derived EVs.[248] The negative surface charge of platelet-derived EVs is due to phosphatidylethanolamine and phosphatidylserine.[249] The cargo of platelet-derived EVs depends on the environment of the platelet that the EVs originated from, but usually they have been found to contain chemokines, cytokines, RNAs, as well as growth and transcription factors.[242,250–252]

3. TECHNIQUES

Immunoaffinity chromatography (IAC), asymmetrical flow field-flow fractionation (AsFlFFF/ AF4), capillary electromigration techniques, and continuous flow quartz crystal microbalance (QCM) were the main techniques employed in this thesis (Figure 6). Kinetic affinity studies of the QCM were complemented with rate constant distribution calculations or interaction maps, while adsorption energy distribution calculations were utilized for equilibrium affinity studies with the CE.
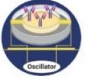
Technique	Antibody	Paper I	Paper II	Paper III	Paper IV
Immunoaffinity chromatography	apoB-100				■
	CD9			■	■
	CD61		■	■	■
Asymmetrical flow field-flow fractionation	apoB-100 *				■
	CD9 *			■	■
	CD61 *		■	■	■
Capillary electromigration techniques	apoB-100	■			
	CD9 *			■	
	CD61 *			■	
Quartz crystal microbalance	apoB-100	■			

Figure 6. Techniques and antibodies utilized in the thesis. * Lipoproteins or EVs were pre-isolated with the IAC.

3.1 Immunoaffinity chromatography with monolithic columns

IAC is an affinity-based liquid chromatographic (LC) technique, where a target antigen (analyte) is bound to an antibody (ligand), usually immunoglobulin G (IgG).[253] In the

IAC, the antibody binds in specific and reversible manner to an epitope[84] of the antigen enabling the isolation and enrichment of antigen even from complex sample matrices such as cell culture medium, urine, serum, or plasma.[26,70,87,88,254,255] The specificity of an antibody to an antigen is determined by its type, e.g., monoclonal antibodies (mAb) recognize single epitopes, while polyclonal antibodies (pAb) recognize can recognize several different epitopes. This is because the pAbs are a mixture of antibodies from different B cells, while the mAbs are produced from a clone derived from a single B cell. The mAbs tend to also be more expensive, but have a higher concentration of antibodies specific towards the wanted epitope,[84,256] being, e.g., more suitable for the isolation of highly specific populations of particles containing the antigen.

In reversible IAC binding process, an antigen-antibody $(A - L)$ complex is formed between the affinity ligand (L) and the analyte (A). The binding and dissociation is described by association (k_a) and dissociation (k_d) constants, while association equilibrium rate constant (K_A) of the process can be calculated by equation (1),

$$K_A = \frac{k_a}{k_d} = \frac{[A-L]}{[A][L]} = \frac{1}{K_D} \qquad (1)$$

where $[A$ - $L]$, $[A]$, and $[L]$ are the concentrations of the analyte-ligand complex, analyte, and ligand. K_D is the dissociation equilibrium rate constant and it has a reciprocal relationship to K_A. The process consists of injection of the sample to the support with immobilized antibody, washing away the compounds not retained by the antibody, eluting the antigen from the antibody, and finally regenerating the stationary support for the next isolation.[257,258] In the IAC the elution is mainly done with non-specific elution by altering the binding conditions. Dissociation of the antigen from the antibody is promoted by changing the ionic strength, polarity or pH of the mobile phase, or antigen mimicking epitope peptide.

Monolithic columns can be utilized for the IAC by immobilizing the antibody on such column. The monolithic columns are suitable for the isolation of biomacromolecules due to reduced mass transfer resistance of convective mass transport, also the binding capacity is not affected by the flow, and there is a possibility for high flow rates with low pressure drop compared to packed particles.[259–261] The backpressure of the monolithic column can be even half of the backpressure generated by a particle-based column of the same parameters.[262]

The Van Deemter equation (2) can be used to describe the separation and performance of monolithic column,

$$H = A + \frac{B}{u} + C_r u \qquad (2)$$

where H is the theoretical plate height, A the Eddy diffusion, B the diffusion in longitudinal direction, C_r the mass transfer resistance coefficient, and u the linear velocity. In addition, $H = L/N$, where L is the column length and N is the theoretical plate number. In this equation it can be seen that lower H values indicate higher efficiency, since a higher theoretical plate number per column length is achieved. Eq. (2) can be expanded into Eq. (3) to take into account experimental parameters,[263]

$$H = 2\lambda d_p + \frac{2\gamma D_m}{u} + \frac{f(k_r)d_p^2 u}{D_m} \qquad (3)$$

such as the factor for the shape of material packing λ, the particle diameter d_p, the obstruction factor γ, the diffusion coefficient of the analyte in the mobile phase D_m, and the retention factor k_r. The following pore size ranges can be classified: macropore ($d_p > 50\ nm$), mesopore ($d_p = 2 - 50\ nm$), and micropore ($d_p < 2\ nm$).[263] A small particle diameter reduces the theoretical plate height significantly according to Eq. (3) due to the decreased effect of mass transfer resistance described by term C_r in Eq. (2). Thus, increased separation efficiency and reduced separation time can be achieved by reducing the particle size in the particle-based columns, but the smaller the particles get, the higher the pressure drop develops. This is not a wanted feature for separating biomacromolecules, shifting the usable particle diameters to mesopores and macropores.[262,263] In addition, the monoliths do not contain areas accessible only by slow diffusion that are found in stagnant fluid in the pores of the particles in the particle-based columns. Thus, interactive sites at the monolithic surfaces are easily accessible for the biomacromolecules by convective flow, further reducing the mass transfer effect.[264] The convective flow allows laminar flow that minimizes the shear forces.[265] High porosity of the monolithic columns allows the low pressure drop described by Darcy's law, and consequently high flow rates,[266]

$$\Delta P = \frac{u_f \mu L}{B_0} \qquad (4)$$

where u_f is the flow velocity, μ the dynamic viscosity of the fluid, L the column length, B_0 the hydraulic permeability, and ΔP the pressure drop difference across the monolithic column. A broader range of properties of the monolithic columns can be described by the Happel equation,[262,266]

$$B_0 = \frac{1}{18\gamma^3} \frac{2-3\gamma+3\gamma^5-2\gamma^6}{(2+4\gamma^5)/3} d_p^2 \qquad (5)$$

where $\gamma = (1-\varepsilon_b)^{\frac{1}{3}}$ and ε_b is the porosity in the monolithic column.

3.2 Asymmetrical flow field-flow fractionation

In AsFlFFF or AF4 only one side of the wall (accumulation wall) of the separation channel is permeable to the flow (Figure 7). The channel inlet is divided into main flow and cross flow that is perpendicular to the main flow. Three mechanisms are possible for retention in the AsFlFFF: hyperlayer, steric, and normal modes. The channel shape can be trapezoidal or rectangular. AsFlFFF utilizes opposing flow relaxation to let the biomacromolecules equilibrate, since the flow cannot be stopped independently of the field as in symmetrical FFF. The sample in AsFlFFF is injected from a separate inlet that comes just after the flow inlet. The sample can, however, be injected from any point between the inlet and outlet and be dispersed widely across the channel, since the carrier liquids from both inlet and outlet are collected into a focusing point before the relaxation.[120] This creates a narrow zone of the sample in the focusing point. The focusing position can be shifted by changing the opposing flow rates:

$$\frac{z'}{L_{channel}} = \frac{V_{inlet}}{V_{inlet}+V_{outlet}} \qquad (6)$$

where z' is the focusing point from the channel inlet, V_{inlet} is the inlet flow rate, V_{outlet} is the outlet flow rate, and $L_{channel}$ is the length of the channel.

Retention time (t_r) in the normal mode depends on the hydration size of the biomacromolecules,[267]

$$t_r = \frac{\pi\eta w^2 d V_c}{2kTV_a} \qquad (7)$$

where η is the dynamic viscosity of the carrier liquid，w is the channel thickness, d is the hydration diameter of the biomacromolecule, V_c is the cross-flow rate, k is the Boltzmann constant, T is the temperature, and V_a is the axial flow rate.

In AsFlFFF only one pump is needed due to only one permeable membrane. Loss of liquid through a membrane generates the cross flow. The trapezoidal channel with decreasing width is designed to compensate the liquid loss generated due to the loss of carrier liquid through the membrane while moving down the channel and to keep the channel pressure constant.[267]
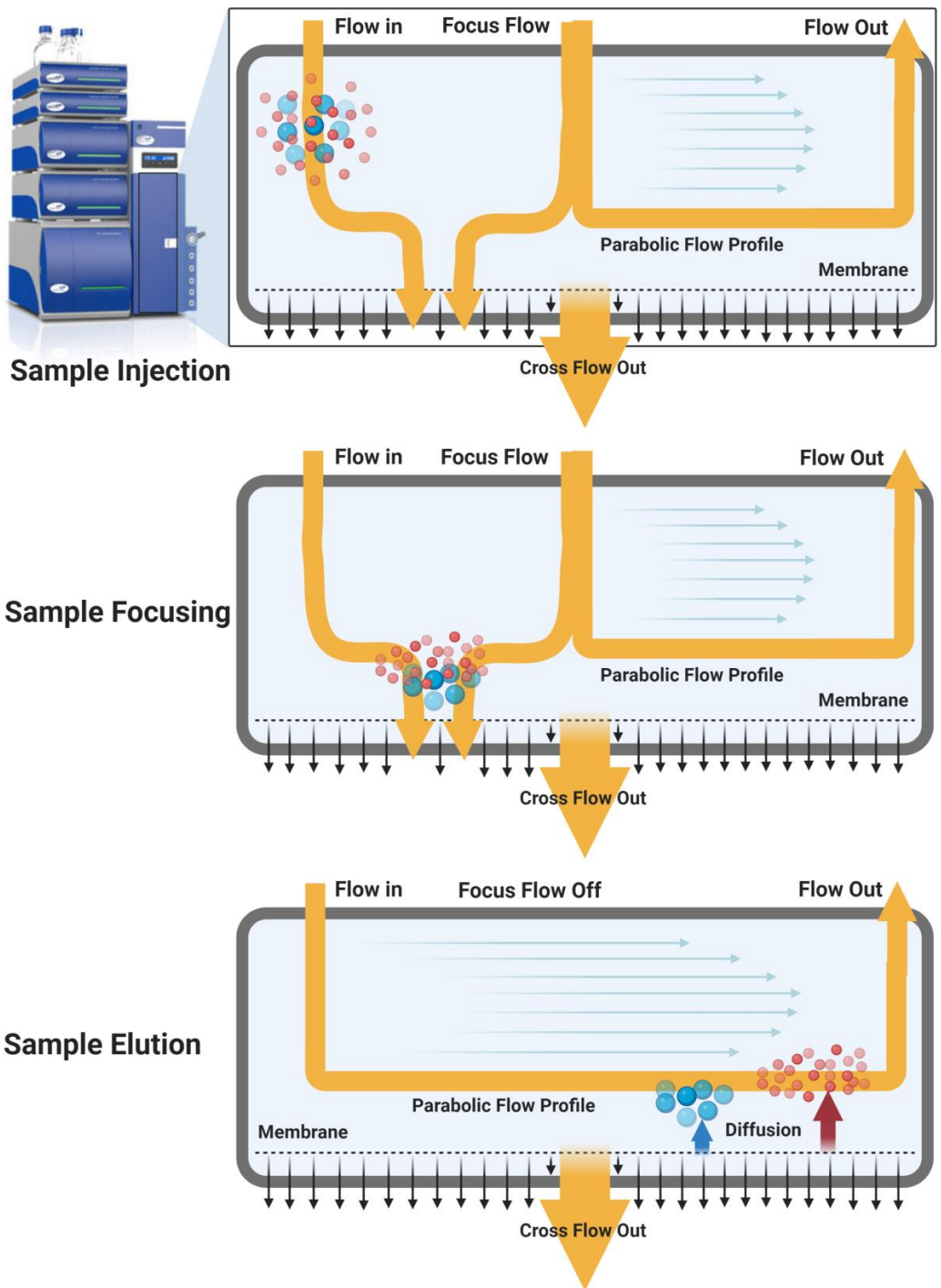
Figure 7. Separation of biomacromolecules in normal mode in the AsFlFFF channel. Adapted from Postnova Analytics.

3.3 Capillary electrophoresis

In capillary electrophoresis (CE), charged biomacromolecules are separated in electrolyte solution (BGE) under a high electric field based on their molecular structure, size, and charge (Figure 8). Fused silica capillaries of diameter 25-100 μm and length of 25-100 cm are used.[127–129]
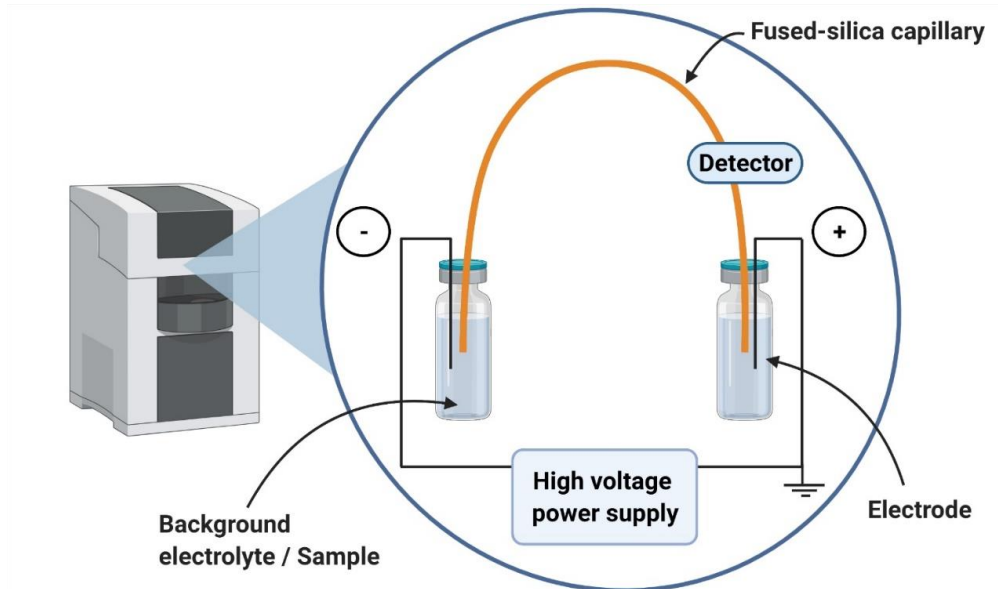
Figure 8. Schematic illustration of capillary electrophoresis instrumentation.

Deprotonation of silanol groups of the fused silica capillary begins above pH 2. A double layer and a potential difference between the capillary wall and the bulk liquid are generated by the interaction of the positive ions of the BGE with the capillary wall. The positively charged diffuse layer advances toward the cathode generating electroosmotic flow (EOF) when voltage is applied. EOF can be exploited in the separation of small molecules but due to the adsorption of proteins to uncoated silica capillary, it is often an unwanted phenomenon during bioseparations. The modification of silanol groups can be done covalently or by charged and neutral surface coating. This allows controlling or even eliminating the EOF by diminishing the surface adsorption. Neutral coatings have been successfully applied to the biological analysis and interaction studies of various proteins. [127–129]

The total mobility of a charged biomacromolecule (μ_{tot}) is a sum of the electroosmotic mobility in the fused silica capillary (μ_{eo}) and the electrophoretic mobility of the biomacromolecule (μ_{ep}), and can be experimentally determined from the migration time of the biomacromolecule (t_m) according to the following equation:

$$\mu_{tot} = \mu_{ep} + \mu_{eo} = \frac{L_{tot}L_{det}}{Vt_m} \tag{8}$$

where L_{tot} is the total capillary length, L_{det} is the length to detector, and V is the voltage utilized in the separation.

Partial filling affinity capillary electrophoresis (PF-ACE) is possible when receptor and analyte have large enough differences in the mobilities so that the receptor can migrate through the analyte zone[268] (Figure 9).
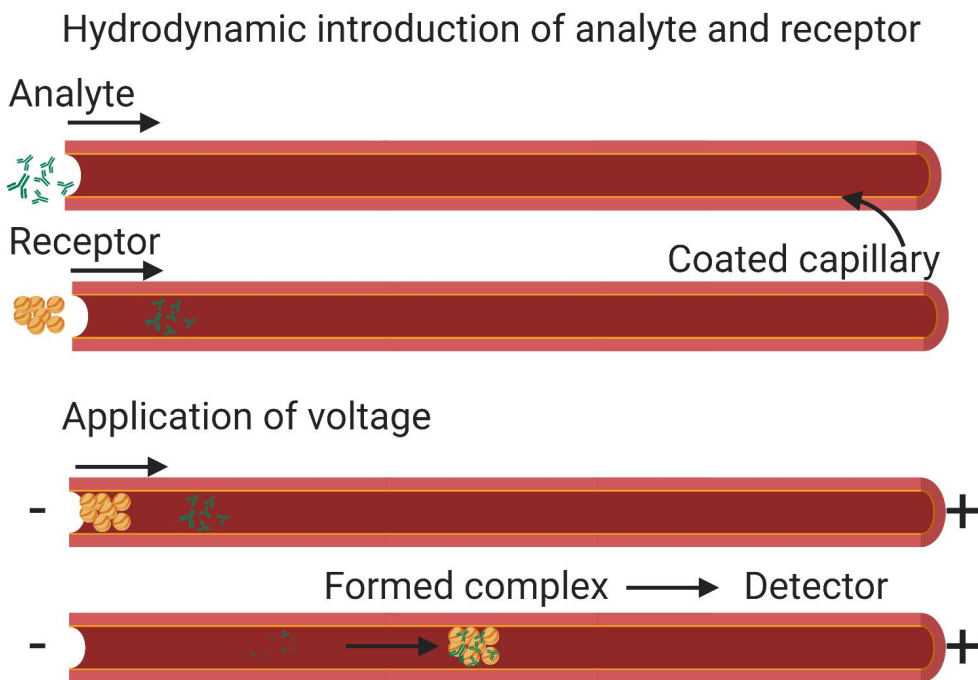
Figure 9. Schematic illustration of the PF-ACE method on a coated silica capillary.

The PF-ACE method can be utilized to determine the affinity constant (K_a) of the formed complex.[155] If the field strength and conductivity stay uniform in the capillary, the affinity constant can be determined:

$$K_a = \frac{1}{K_d} = \frac{\pi r^2 L_{det}}{t_{0,det}} \frac{d\Delta t_m}{dn} \tag{9}$$

where K_d is the dissociation constant, r is the inner radius of the capillary, $t_{0,det}$ is the time that the analyte needs to reach the detector when the receptor is not present, Δt_m is the changes in the migration times, n is the molar amount of the receptor.

3.4 Continuous flow quartz crystal microbalance

Developed in 1957 by G. Sauerbrey,[269] QCM is a mass sensitive technique that utilizes voltage generated by piezoelectric effect of quartz crystal during mechanical stress. The change in frequency upon mass deposition on the surface of the quartz crystal is described by the Sauerbrey equation,[270]

$$\Delta m = -C_s \cdot \Delta f \tag{10}$$

where Δm is the change in mass on the surface of the quartz crystal, Δf is the frequency change of the oscillating crystal, and C_s is the mass sensitivity constant.

According to the equation, the frequency shifts are correlated with changes in the mass on the surface of the crystal. Higher sensitivity can be achieved by cutting the crystal thin, and immobilization of ligands is enabled by coating the crystal surface with gold.[271–273] The basic principle of QCM to study interactions between antibody and biomacromolecules is depicted in Figure 10. After the equilibration, the oscillator undergoes an association of the biomacromolecules resulting in frequency shift followed by a dissociation phase where the interaction is broken. Finally, regeneration of the oscillator returns the frequency back to the base frequency. Collected sensogram at different analyte concentrations can be further analyzed with global fitting algorithms, adsorption energy distribution (AED) calculations,[135] rate constant distribution maps (RCD), as is done in this thesis, or even with a more advanced data analysis tool called adaptive interaction distribution algorithm (AIDA).[274–276]
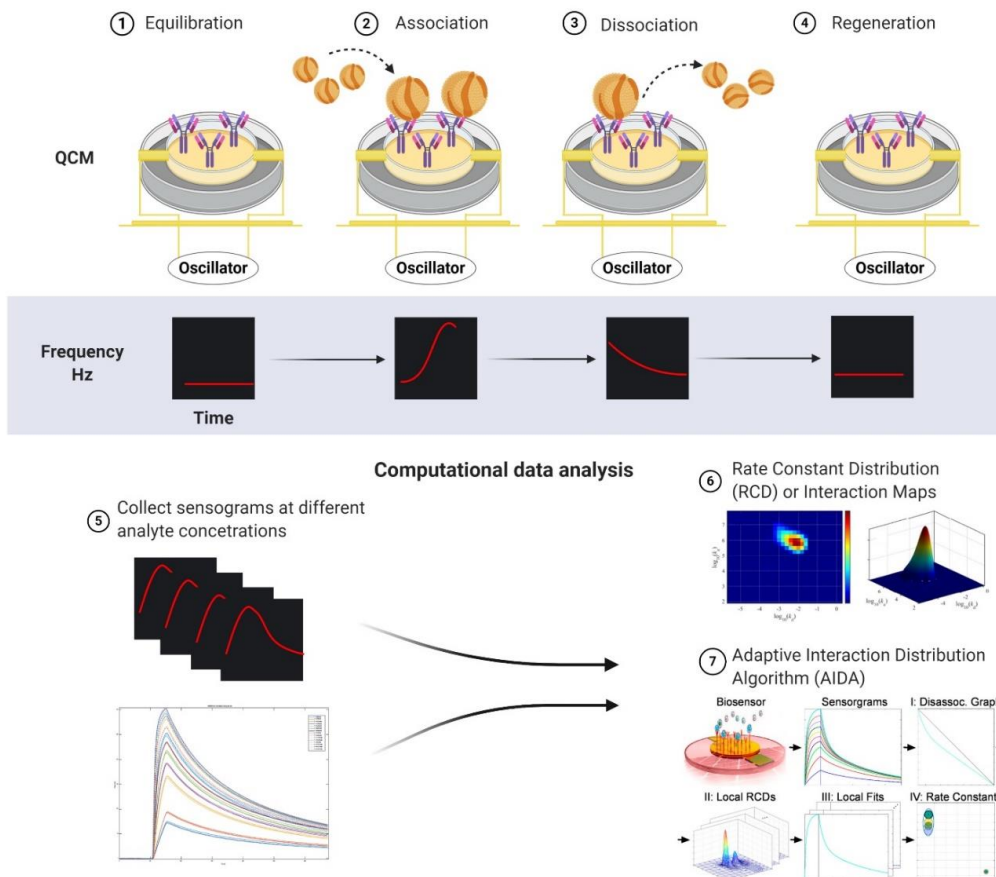
Figure 10. Basic workflow of interaction studies with QCM.

4. EXPERIMENTAL

This chapter collects the lists of antibodies (Table 2), chemicals (Table 3), and materials, instruments, and equipment (Table 4) used in the studies. Detailed information is found in Papers I-IV. Figures in the thesis were created with BioRender.com.

Table 2. List of antibodies

Antibody	Supplier	Paper
Purified Mouse Anti-Human CD61 (clone VI-PL2) antibody	BD Biosciences	II-IV
Purified Mouse Anti-TSG101 Clone 51/TSG101	BD Biosciences	II
CD9 Monoclonal Antibody (eBioSN4 (SN4 C3-3A2)), eBioscience™	Thermo Fisher Scientific	III-IV
Mouse Monoclonal Anti-CD9 Antibody (C-4): sc-13118	Santa Cruz Biotechnology	II
Human monoclonal anti-human-apolipoprotein B100 code Anti-h ApoB 2101 SPTN-5	Medix Biochemica	I, IV
HRP-conjugated sheep anti-mouse IgG antibody	GE Healthcare	II

Table 3. List of chemicals

Chemical	Supplier	Paper
1-Ethyl-3-(3-dimethylaminopropyl) carbodiimide hydrochloride (EDC-HCl)	Aladdin Chemical Reagent Company	I
2-(Cyclohexylamino)ethanesulfonic acid (CHES)	Sigma-Aldrich	III
4-(2-Hydroxyethyl)-1-piperazineethanesulfonic acid (HEPES)	Sigma-Aldrich	I
4-(4-Methoxybenzylamino)-7-nitro-2,1,3-benzoxadiazole (MBD)	Sigma-Aldrich	III
Acetic acid	VWR	III
Acetonitrile (gradient grade, purity ≥99.9%)	Sigma-Aldrich	IV
Ammonia 25% (NH_3)	Riedel-de Haën	I-IV
BCA Protein Assay Kit	Thermo Fisher Scientific	IV
Bovine Serum Albumin (BSA)	Sigma-Aldrich	I-II
Bovine milk	Excilone	III
Buffer solutions: pH 4 (phthalate), pH 7 (phosphate), and pH 10 (borate)	Fisher Scientific	I
Cholesterol CHOD-PAP reagent	Roche	IV
Clarity ECL substrate	Bio-Rad	II
DC Protein assay	Bio-Rad	II, IV
Dimethyl sulfoxide (DMSO)	FF-Chemical Ab	I

Chemical	Supplier	Paper
Ethanolamine	Sigma-Aldrich	I-IV
Ethylenediaminetetraacetic acid disodium salt dihydrate (Na_2EDTA)	Sigma Chemicals	I
Gentamycin sulfate	Lonza	I
Glycine	Sigma-Aldrich	II
Formic acid	VWR Chemicals	IV
HDL_2	Wihuri Institute	I
Human plasma	Finnish Red Cross Blood Service	I-IV
	Excilone	III
Hydrochloric acid (0.1-1.0 M)	FF-Chemical Ab	I-IV
Hydrochloric acid (fuming 37%)	Fluka / Sigma Aldrich	I-II
IDL-VLDL	Wihuri Institute	I
LDL	Wihuri Institute	I
Methanol (99%)	Honeywell	IV
N-Hydroxysulfosuccinimide sodium salt (sulfo-NHS)	Aladdin Chemical Reagent Company	I
ortho-Phosphoric acid	Merck KGaA	I
PageRuler prestain protein ladder	Thermo Fisher Scientific	II
Phosphate buffered saline (PBS) tablets	Sigma-Aldrich	II-IV
PBS 10x	Sigma-Aldrich	III
Poly(2-vinylpyridine)-block-(ethylene oxide) (P2VP-b-PEO)	Polymer Source	I
Pony plasma	Excilone	III
Pony serum	Excilone	III
Sodium acetate	Sigma-Aldrich	III
Sodium azide (NaN_3)	Sigma-Aldrich	I
Sodium carbonate (Na_2CO_3) anhydrous	Sigma-Aldrich Merck KGaA	I-III IV
Sodium chloride (NaCl)	Fisher Chemicals	I
Sodium citrate trihydrate ($C_6H_5O_7 \cdot 3Na \cdot 3H_2O$)	Sigma-Aldrich	I
Sodium dodecyl sulfate (SDS)	Sigma-Aldrich	III
SDS-PAGE (12%)	Thermo Fisher Scientific	II
Sodium hydrogen carbonate ($NaHCO_3$)	Sigma-Aldrich Merck KGaA	II-III IV
Sodium hydroxide (NaOH) (0.1-1.0 M)	FF-Chemical Ab VWR	I-II III-IV
Tris(hydroxymethyl)aminomethane (Tris)	Sigma-Aldrich	III
TWEEN® 20	Sigma-Aldrich	I
Vybrant™ CFDA SE Cell Tracer Kit (dye 5-(and-6)-Carboxyfluorescein diacetate succinimidyl ester, CFDA-SE)	Thermo Fisher Scientific	III

Table 4. Materials, instruments, and equipment

Materials, instruments, and equipment	Manufacturer	Paper
14 position stream selection valve (Cheminert C25Z-31814D)	Vici AG	IV
AF2000 AsFlFFF system	Postnova Analytics	II-IV
AF2000 program	Postnova Analytics	II-IV
AF2000 MT series membrane (10 kDa mass cut-off regenerated cellulose)	Postnova Analytics	II-IV
AF2000 MF spacer (350 µm)	Postnova Analytics	II-IV
Agilent CE ChemStation	Agilent	I
Agilent ^{3D}CE instrument	Agilent	I
CBM-20A modular system controller	Shimadzu	III-IV
Centrifuge (Allegra X-15R)	Beckman Coulter	III
Centrifugal filter units		
Amicon 100 kDa	Merck Millipore	III
Nanosep Omega Membranes 3K	PALL Life Sciences	III
Nanosep® centrifugal devices 10K	PALL Corporation	IV
CIM® CDI -0.34 mL disk	BIA Separations	II-IV
Diode array detector (DAD) (G1315A)	Agilent Technologies	IV
Disk housing	BIA Separations	II-IV
Dynamic light scattering (DLS) instrument (Zetasizer Nano)	Malvern Instruments	II-IV
Exosome Spin Columns (MW 3000)	Thermo Fisher Scientific	III
Filters Supor®-200 membrane filters, 0.2 µm	PALL Life Sciences	IV
MILLEX® Low Protein Binding Hydrophilic LCR (PTFE) membrane filters, 0.45 µm	Millipore	IV
Fraction collector (FRC-10A)	Shimadzu	III-IV
Freeze dryer (Heto PowerDry LL1500)	Thermo Scientific	III
Fused-silica capillaries (i.d. 50 µm)	Optronis GmbH	I
	CM Scientific	III
HPLC system (Agilent 1260 Infinity)	Agilent	IV
Isocratic high-performance liquid chromatography (HPLC) pumps (PN1130)	Postnova Analytics	II-IV
LAS-3000 Imaging system	Fujifilm	II
LNB-Carboxyl sensor chips	Attana AB	I
Microelectric valve actuator (EMHMA-CE)	Vici AG	IV
Microplate reader (Multiscan EX)	Labsystems Diagnostics	II

Materials, instruments, and equipment	Manufacturer	Paper
Millipore water purification system	Millipore SA	I-IV
Direct-Q3 UV purification system	Millipore	III
Model E60 actuator	Vici AG	IV
Multiangle laser light scattering (MALS) detector (Postnova PN3070)	Postnova Analytics	II-IV
Nanoparticle Tracking Analysis (NTA)		
Zetaview	Particle Metrix	III
Nanosight NS300 instrument	Malvern	III
Nanosight model LM14 with blue laser and SCMOS camera	Nanosight	II
Quartz crystal microbalance (QCM) (Attana A100)	Attana AB	I
PA 800 Plus system	Sciex Separation	III
pH meter (pH 7110)	WTW GmbH	I-IV
pH meter (SevenCompact)	Mettler Toledo	III
Plate reader (EnSpire 2300)	PerkinElmer Inc	IV
Polyvinyl Alcohol (PVA) neutral capillaries	Sciex	III
Purging port (PN1610)	Postnova Analytics	II-IV
Scanning electron microscope (SEM) (Hitachi S-4800 field emission SEM)	Hitachi	IV
SEC column (qEVoriginal)	Izon Science	III
SeQuant® ZIC®-cHILIC column (150 mm x 2.1 mm i.d., pore size 100 Å,3 µm particle size)	Merck KGaA	IV
SeQuant® ZIC®-cHILIC guard column (20 mm x 2.1 mm i.d., 200 Å particle size, particle size 5 µm	Merck KGaA	IV
Single board computer (Model B Rev. 2.0)	Raspberry Pi	IV
Six-port medium pressure injection valve (V-45)	IDEX Upchurch Scientific	IV
Solid-state laser induced fluorescence detector	Integrated Optics	III
Solvent degasser (PN7520)	Postnova Analytics	II-IV
Solvent organizer (PIN PN7140)	Postnova Analytics	II-IV
Sputter coater (208HR)	Cressington	IV
Syringe pump (Sp100i)	WPI	II-III
Syringe pump (Kloehn v6)	Postnova Analytics	II-IV
Transmission electron microscope (TEM) (Tecnai 12)	FEI Company	II
Triple quadrupole mass spectrometer (Agilent 6420)	Agilent	IV
UV detector (SPD-20A Prominence)	Shimadzu	II-IV
Ultra HPLC in-line filter (2.0 µm KrudKatcher)	Phenomenex	IV
Ultracentrifuge (Optima TL Table-Top)	Beckman Coulter	I
(Optima XPN-80, 50TI and SW41 rotors)	Beckman Coulter	III
Vacuum-driven filtration system (Millipore Steritop, 0.22 µm)	Millipore	III
Water bath MGW (Lauda K2)	Lauda-Köningshofen	I
Zeta potential measurements (Zetasizer Nano ZS)	Malvern Instruments	IV

4.1 Methods

4.1.1 Preparation of buffers and solutions

Phosphate buffer and phosphate buffered saline (PBS) (Papers I-IV)

The phosphate buffer (I = 20 mM) used in the CE and QCM experiments was prepared by adding 485 µL of phosphoric acid (85%) and dissolving it with 14.16 ml of 1.0 M NaOH to 900 ml of Milli-Q water. The pH of the solution was first adjusted to 7.4 with 1.0 M HCl and then filled to the final volume of 1000 ml with Milli-Q water. To calculate the ionic strength of the buffer, $pK_{a,2}$ of 7.2 was used for phosphoric acid.[277] (Paper I)

For the isolation and fractionation of the biomacromolecules, phosphate-buffered saline (PBS, pH 7.4) was also utilized. It was prepared following the standard procedure, either from 10x PBS solution or PBS tablets. One PBS tablet was dissolved into 200 mL Milli-Q water and filtered through a 0.2 µm membrane filter. (Papers I-IV)

Ethanolamine (Papers II-IV)

1 M ethanolamine solution (pH 9.0) was prepared by adjusting the pH with hydrochloric acid (fuming 37%). (Paper I) 2 M ethanolamine, pH 9.0, was prepared by adding 0.603 mL of ethanolamine in a small amount of Milli-Q water and then 900 µL of fuming 37% HCl was added by placing the pipette tip directly inside the ethanolamine solution. The final solution was prepared by topping up the total volume to 5 mL with Milli-Q water.

Ammonium hydroxide (NH$_4$OH) (Papers I-IV)

The ammonium hydroxide solution (NH$_4$OH), pH 11.3, was prepared by adding 2.26 mL of 25% ammonia and filling it to a final volume of 100 mL with Milli-Q water.

Carbonate-bicarbonate solution (Papers II-IV)

1.06 g of anhydrous Na_2CO_3 was dissolved in 100 mL Milli-Q water to prepare 0.1 M Na_2CO_3 stock solution. 0.8401 g of $NaHCO_3$ was dissolved in 100 mL Milli-Q water to prepare 0.1 M $NaHCO_3$ stock solution. The carbonate-bicarbonate solution was prepared by mixing 90 mL of 0.1 M Na_2CO_3 stock solution with 10 mL of 0.1 M $NaHCO_3$ stock solution. The pH of the solution was adjusted to 11.3 with NaOH.

CE-LIF background electrolyte solution (Paper III)

The capillary electrophoresis - laser-induced fluorescence (CE-LIF) background electrolyte (BGE) was prepared from two stock solutions of 1.5 M Tris and 1.2 M CHES. 1.5 M Tris was prepared by dissolving 1.817 g of Tris base in 10 mL of water and 1.2 M CHES by dissolving 10.447 g of CHES in 42 mL of water. Then, 8 mL of 1.5 M Tris was mixed with 41.09 mL of 1.2 M CHES. Deionized water was then added to a total volume of 50 mL.

Solutions for QCM studies (Paper I)

A phosphate buffer (I = 20 mM) was used to dilute anti-apoB-100 mAb (100 µg/mL) before using the antibody for amine coupling on the surface of LNB-Carboxyl chip. The buffer (10 mM HEPES, 150 mM NaCl, 0.005% Tween 20, pH 7.4) utilized for the immobilization was prepared by dissolving 1.19 g of HEPES with 4.38 g of NaCl and 0.25 ml of 10% Tween 20 in 400 ml of Milli-Q water, followed by adjustment to pH 7.4 with 1.0 M NaOH. The final volume of the immobilization buffer was adjusted to 500 mL with Milli-Q water. The activation reagents, 0.4 M EDC and 0.1 M S-NHS, were both dissolved in Milli-Q water before mixing. The LDL and IDL-VLDL samples (3–110 µg/mL) used in the QCM experiments were diluted in the phosphate buffer (I = 20 mM). A regeneration solution was prepared by diluting 25% ammonia in Milli-Q water to obtain 0.28 M ammonium hydroxide pH 11.5. The immobilization solution of anti-apoB-100 mAb was prepared in the same manner as mentioned above using the phosphate, but the pH was adjusted to 6.4 with 1.0 M HCl.

HILIC-MS/MS mobile phase (Paper IV)

The HILIC-MS/MS mobile phase A was prepared by adding 1 mL of formic acid to acetonitrile (999 mL) and the mobile phase B was prepared by adding 1 mL of formic acid to MQ water (999 mL). All standards and internal standards were prepared in mobile phase B.

4.1.2 Immobilization procedures

Immobilization of anti-apoB-100 mAb on LNB-Carboxyl sensor chip (Paper I)

Immobilization of anti-apoB-100 mAb was done with an amine coupling procedure according to the manufacturer's recommendations with slight modifications. Prior to the immobilization the LNB-Carboxyl sensor chip was pre-wetted ex-situ with 20 µL

of Milli-Q water and thereafter inserted into the instrument and left to stabilize. The immobilization was performed with the analysis buffer (10 mM HEPES, 150 mM NaCl, 0.005% Tween 20, pH 7.4) at the flow rate of 10 µL/min at 25°C. To activate the surface, freshly mixed 0.4 M EDC and 0.1 M S-NHS (1:1, v/v) was injected using automated C-Fast software for 5 min. The surface activation was done once. The amine coupling of anti-apoB-100 mAb (100 µg/mL in phosphate buffer; pH 6.4) was carried out by injecting the solution twice for 5 min. Finally, the remaining carboxyl groups were deactivated with two injections (5 min each) of 1 M ethanolamine solution (pH 9.0).

Immobilization of antibodies on CIM® CDI - 0.34 mL disk (Papers II-IV)

A CIM® CDI -0.34 mL disk, with the pore size of 1.3 µm, was placed in the disk housing and washed with 6.8 mL of Milli-Q water followed by 15 mL of PBS buffer (pH 7.4). The antibody (1 mL of 0.5 mg/mL of anti-CD9 (Papers III-IV), anti-CD61 (Papers II-IV), and 5 mL of 0.5 mg/mL of anti-apoB-100 (Paper IV)) was injected through the housing back and forth using a syringe pump and two syringes at both ends of the column with a flow rate of 0.5 mL/min for 1.5 h at room temperature. The cycle of injecting back and forth was repeated five times daily for three consecutive days. The disk was left over a weekend to ensure maximum antibody immobilization, the disk was then washed with 3 mL of PBS, and the remaining CDI groups were deactivated by passing 1 mL of 2 M ethanolamine (pH 9.0) through the system twice and left overnight with stoppers. The immobilization procedure is depicted in Figure 11. The system was finally washed with 20 mL PBS buffer to remove the excess ethanolamine.
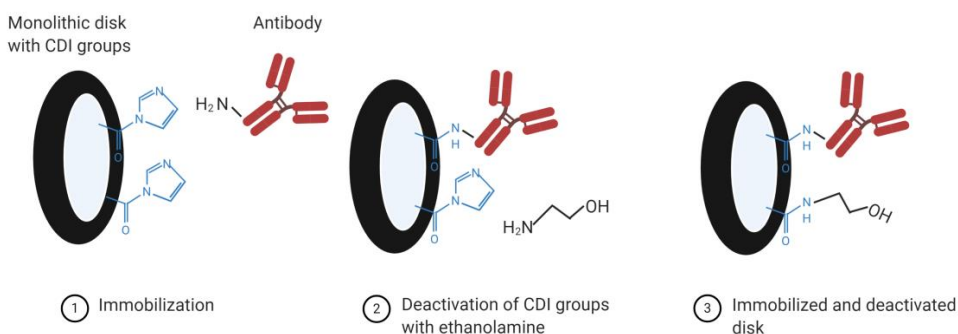

Figure 11. Immobilization of antibodies on CIM® CDI - 0.34 mL disk.

4.1.3 Isolation of biomacromolecules

Isolation of high-density lipoprotein (HDL$_2$) with ultracentrifugation (Paper I)

HDL$_2$ was isolated from serum and plasma samples by sequential ultracentrifugation and KBr was used for density adjustment. After the first isolation of apoB-100 containing lipoproteins at d = 1.063 g/mL (5 °C, 3 h, 500,000 × g), the infranatant fraction was adjusted to density 1.125 g/mL with solid KBr and then centrifuged (5 °C, 18 h, 500,000 × g). The HDL$_2$ was obtained in top fraction. The purity of the isolated HDL$_2$ was checked with FPLC size-exclusion chromatography. The isolated HDL$_2$ was dialyzed against phosphate-buffered saline (PBS, pH 7.4) and stored at −80 °C before analysis.

Isolation and characterization of apoB-100 containing lipoproteins (LDL, IDL-VLDL) with ultracentrifugation (Papers I and IV)

Human LDL (d = 1.019–1.050 g/mL) was isolated by sequential ultracentrifugation in the presence of 3 mmol/L Na$_2$EDTA.[278,279] First, EDTA and 100 µg/mL gentamycin sulfate were added to the plasma sample and the density was adjusted to 1.019 with KBr. Then, the plasma sample was centrifuged at 40,000 rpm (rotor 50.2 Ti, g$_{max}$ 302,000) at +4 °C for 24 h. The IDL-VLDL fraction was collected from the top and the density of the remaining plasma was set to 1.050 g/mL with KBr. The density-adjusted plasma was centrifuged at 40,000 rpm for 72 h and the plasma for further steps was collected on the top of the solution. The collected solution was re-centrifuged at a density of 1.063 g/mL for 24 h, collected and dialyzed extensively against 150 mM NaCl – 1 mM EDTA (pH 7.4) followed by dialysis against phosphate-buffered saline (PBS, pH 7.4).

Isolation of bovine milk-derived EVs with sucrose gradient ultracentrifugation (Paper III)

Whole bovine milk samples were centrifuged at 3,000×g for 30 min at 4 °C (Allegra X-15R, Beckman Coulter) to separate fat from skimmed milk. The whey was obtained after acid precipitation of milk (50 mL) with 5 mL of 10% acetic acid and incubation at 37 °C for 10 min. This was then continued by addition of 5 mL of 1 M sodium acetate, and incubation for 10 min at room temperature, followed by centrifugation at 1,500×g, 4 °C for 15 min and filtration of supernatant using vacuum-driven filtration system (Millipore Steritop, 0.22 µm). The whey supernatants were concentrated by the

centrifugation at 4,000×g and 20 °C using Amicon 100 kDa centrifugal filter units. The obtained retentate was ultracentrifuged for pelleting the EVs at 100,000×g for 1h 10 min at 4 °C (Beckman Coulter, Optima XPN-80, 50TI rotor). The pellets were solubilized in 500 µL of PBS then added to 11 mL of pre-prepared sucrose gradient 5–40% and ultracentrifuged at 200,000×g for 18 h at 4 °C (SW41 rotor). Selected fractions corresponding to flotation densities of EVs' (1 mL) were collected, diluted in 6 mL of PBS and finally centrifuged at 100,000×g for 1h 10 min at 4 °C (50TI rotor). The pellets were re-suspended in 50 µL of PBS and stored at −80 °C.

Isolation of pony plasma/serum and human plasma derived EVs with size-exclusion chromatography (Paper III)

Preparation of plasma: Peripheral blood was collected into EDTA-coated vacutainer tubes. After ten-time inversion, the samples were processed within 60 min of collection. Consecutive centrifugation steps at 2,500×g, 4 °C for 15 min and then at 15,000×g for 10 min were performed followed by filtration of the supernatant through 0.22 µm filters.

Preparation of serum: Whole blood was collected into anticoagulant-free tubes and allowed to clot at room temperature for 45 min. The clot was removed by centrifuging at 3,200×g, 4 °C for 15 min, followed by centrifugation at 15,000×g, 4 °C for 10 min and filtration of the supernatant through 0.22 µm filters.

500 µL of pre-treated plasma/serum was loaded onto a qEVoriginal SEC column (Izon Science) that was washed and equilibrated with PBS. Fraction collection (0.5 mL per fraction) was carried out immediately using PBS as elution buffer. The selected elution fractions were pooled and were subsequently concentrated using 100 kDa Amicon centrifugal filter units. Post-treatment processing with several washing steps with PBS was applied to obtain highly pure EV fractions.

Isolation of human plasma-derived EVs with monolithic immunoaffinity chromatography (Papers II-III)

Monolithic disk columns were injected with diluted human plasma samples (250 µL of plasma diluted to 5 mL in PBS) immobilized with either anti-human CD61 or anti-human CD9 antibodies. Unbound plasma was washed away with 3 mL of PBS. The enriched EVs were eluted with 2 mL of either ammonium hydroxide (NH_4OH, pH 11.3) or carbonate-bicarbonate (pH 11.3) solution. The pH of the isolates (final volume 0.5

mL) was adjusted by addition of 50 µL of 1 M HCl. The monolithic disk columns were equilibrated with 3 mL of PBS before the next sample injection.

Isolation of human apoB-100 containing lipoproteins, CD9^{+}, and CD61^{+} EVs by the on-line immunoaffinity chromatography - asymmetrical flow field-flow fractionation system (Paper IV)

Three separate monolithic disk columns for the IAC were immobilized with anti-apoB-100, anti-CD9, and anti-CD61. The IAC process cycles (Figure 12) for the isolation of apoB-100 containing lipoproteins, CD9^{+}, and CD61^{+} EVs can be found in Table 5. The repetition of the successive experiments is shown in Figure 12 where the regeneration and waiting periods were taken into account for the AsFlFFF to be ready for the next fractionation. The total time for apoB-100 lipoprotein isolation and regeneration of the disk column was 16.5 min (1 mL sample injection, 3 mL PBS wash, elution with 2 mL of NH_4OH, and 3 mL PBS wash). The isolation and regeneration cycle for the EV disks took 51 min. The major difference between the isolations was that EV isolations had a larger sample volume (5 mL) and an additional NH_4OH regeneration step. The carbonate-bicarbonate solution was used to elute the EVs. The flow rate for the apoB-100 containing lipoprotein isolation and elution was set to 0.5 mL/min, whereas it was 0.25 mL/min for the EV isolation. The regeneration step for EV disks before the analysis of the next sample was performed with 2 mL of NH_4OH and 3 mL of PBS at a flow rate of 1 mL/min. No additional regeneration step was needed for the apoB-100 disk, since NH_4OH was already used for the elution. The AsFlFFF run was automatically started after the eluent of the IAC filled the sample loop (500 µL) after the void volume in the six port valve.
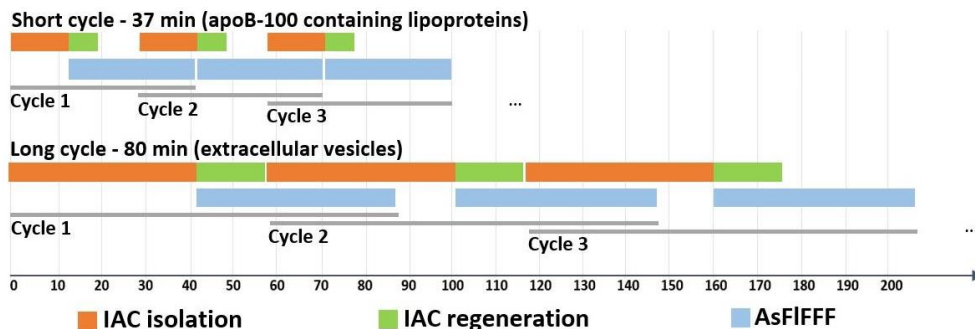
Figure 12. Repeated successive IAC-AsFlFFF analysis cycles. A short cycle was used for isolation and fractionation of apoB-100 containing lipoproteins and long cycle for EVs. An automated injection to the AsFlFFF was done when eluate from IAC was fully transferred to the sample loop of the six port valve.

Table 5. Process cycles used in the IAC.

Isolation program for apoB-100 containing lipoproteins				EV isolation program			
	mL	mL/min	min		mL	mL/min	min
Sample loading	1	6	0.167	**Sample loading**	5	6	0.833
Sample injection	1	0.5	2	**Sample injection**	5	0.25	20
PBS loading	3	6	0.5	**PBS loading**	3	6	0.5
PBS injection	3	0.5	6	**PBS injection**	3	0.25	12
Ammonium hydroxide loading	2	6	0.333	**Carbonate-bicarbonate loading**	2	6	0.333
Ammonium hydroxide injection	2	0.5	4	**Carbonate-bicarbonate injection**	2	0.25	8
PBS loading	3	6	0.5	**PBS loading**	3	6	0.5
PBS injection	3	1	3	**PBS injection**	3	1	3
total			16.5	**Ammonium hydroxide loading**	2	6	0.333
				Ammonium hydroxide injection	2	1	2
				PBS final loading	3	6	0.5
				PBS final injection	3	1	3
				total			51

4.1.4 Fractionation of biomacromolecules

The collected EVs (500 µL) from anti-CD61 or anti-CD9 disk were manually injected to the AsFlFFF (Papers II-III), while the on-line system was utilized for automatic injection of the lipoprotein and EV samples (Paper IV). Optimal conditions for all of the AsFlFFF experiments are listed in Table 6. (Papers II-IV)

For labeling, the EV fractions (300 µL each) obtained with AsFlFFF were frozen and subsequently lyophilized over 3 h at a temperature of −110 °C. Before starting the labeling protocol, the fractions were rehydrated with 30 µL PBS for EVs enrichment. (Paper III)

Table 6. Optimal AsFlFFF conditions for fractionation of apoB-100 containing lipoproteins and EVs.

		Paper II	Paper III	Paper IV Lipoproteins	Paper IV EVs
Mobile phase	Sigma-Aldrich	PBS, pH 7.4	PBS, pH 7.4	PBS, pH 7.4	PBS, pH 7.4
Channel thickness	Postnova AF2000 MT spacer	350 µm	350 µm	350 µm	350 µm
Membrane	Postnova AF2000 MT series Membrane	Regenerated cellulose, 10 kDa mass cut-off	Regenerated cellulose, 10 kDa mass cut-off	Regenerated cellulose, 10 kDa mass cut-off	Regenerated cellulose, 10 kDa mass cut-off
Injection loop		500 µL	500 µL	500 µL	500 µL
Injection step	Time	5 min	5 min	5 min	5 min
	Flow	0.1 mL/min	0.1 mL/min	0.1 mL/min	0.1 mL/min
Detector	Flow	1.0 mL/min	0.5 mL/min	0.5 mL/min	0.5 mL/min
Focus step including 1 min transition time	Time	6 min	6 min	6 min	6 min
	Cross flow	3 mL/min	3 mL/min	3 mL/min	3 mL/min
Separation	Time	5 min	2 min	2 min	5 min
	Cross-flow	Linear decay 3.0 mL/min to 1.0 mL/min	Linear decay 3.0 mL/min to 0.5 mL/min	Linear decay 3.0 mL/min to 0.5 mL/min	Linear decay 3.0 mL/min to 0.5 mL/min
	Time	15 min	1 min	1 min	15 min
	Cross-flow	Linear decay 1.0 mL/min to 0 mL/min	Linear decay 0.5 mL/min to 0 mL/min	Linear decay 0.5 mL/min to 0 mL/min	Linear decay 0.5 mL/min to 0 mL/min
	Time	10 min	15 min	15 min	14 min
	Cross-flow	0 mL/min	0 mL/min	0 mL/min	0 mL/min

4.1.5 Capillary electrophoresis of biomacromolecules

Capillary electrophoresis coating procedure (Paper I)

Unfavorable adsorption of lipoproteins on the negatively charged fused-silica capillary was diminished by coating the capillary inner wall with quaternized double-hydrophilic poly(N-methyl-2-vinyl pyridinium iodide-block-ethylene oxide) (P2QVP-b-PEO) diblock copolymer.[280] P2QVP-b-PEO was dissolved in Milli-Q water to a concentration of 0.1 mg/mL. The coating procedure was slightly modified from previous studies.[142,280] First, an uncoated fused-silica capillary was pretreated by flushing for 15 min, 10 min, and 10 min with 0.1 M NaOH, Milli-Q water, and phosphate buffer (pH 7.4, I = 20 mM) at a pressure of 940 mbar. Then the capillary was flushed for 20 min, 10 min, 25 min, and 5 min with 1 M HCl, 0.1 M HCl, Milli-Q water, and the pH 7.4 phosphate buffer, respectively, at a pressure of 940 mbar. After pretreatment, the voltage of +15 kV was applied for 5 min. The P2QVP-b-PEO coating solution was then applied for 40 min and left for 30 min to react with the silanol groups on the capillary surface. Excess copolymer solution was then rinsed by flushing through the capillary for 60 min at a pressure of 940 mbar. The coating procedure with the polymer solution was repeated twice to ensure the best possible stability of the wall coating. The whole procedure was conducted at 37.0 °C. To ensure the success of the coating, EOF mobility was measured using DMSO with the Williams and Vigh method.[281] The stability of the mobility value was also controlled during the kinetic studies. It was at the level of $10^{-9} - 10^{-10}$ $m^2V^{-1}s^{-1}$.

Partial filling affinity capillary electrophoresis (Paper I)

The partial filling (PF) procedure in the CE was modified from our previous studies.[135,137,139,142,159] Briefly, negatively charged analytes were hydrodynamically introduced to the P2QVP-b-PEO coated capillary. First, slightly negative anti-apoB-100 mAb was introduced in the concentration range of 0.0002 to 0.1 mg/mL for 3 s, followed by injection of the more negative lipoproteins at 50 mbar pressure.[280] Fused-silica capillaries (i.d. 50 μm) had a length of L_{tot} 38.5 cm and L_{det} 30 cm. The lipoprotein concentrations were different for the antibody-antigen studies. The LDL (0.075 mg/mL) was introduced for 2 s, the IDL-VLDL (0.0036 mg/mL) for 8 s, and the HDL_2 (0.20 mg/mL) for 2 s at 50 mbar. When the voltage of -25 kV was applied and detector was in the cathode end, more anionic lipoproteins reached anti-apoB-100 mAb and formed the LDL -, IDL -, and VLDL - anti-apoB-100 mAb complexes. HDL_2 lacking apoB-100, was used as a control to test the specificity of the anti-apoB-100 mAb. The

detection was performed at the wavelength 200 nm. Before each run, the capillary was rinsed for 2 min with the phosphate buffer (pH 7.4). All the experiments were conducted at 37.0 °C. After every second run, the EOF mobility was measured to control the stability of the coating.

Fluorescent labeling of EVs (Paper III)

The fluorescently labeled EVs were prepared using the 5-(and-6)-carboxyfluorescein diacetate succinimidyl ester (CFDA-SE). The CFDA-SE stock solution (10 mM) was prepared in DMSO following the manufacturer's instructions. Prior to the staining, the working solution was diluted to 200 μM in PBS. 20 μL of EVs was mixed with 20 μL of 200 μM CFDA-SE solution (resulting in a final CFDA-SE concentration of 100 μM), and incubated for 2 h in the dark at 37 °C with gentle shaking.

Removal of free label (Paper III)

Labeled EVs were obtained from two different matrix exchange approaches, using either centrifugal filtration Nanosep Omega Membranes 3K or with commercial Exosome Spin Columns (MW 3,000 Da). The first approach (centrifugal filtration) was carried out by addition of the desired buffer to be substituted on the top of the labeled EVs, then centrifugal spinning of the column for approximately 4 min at 5,000×g. This process was repeated four times. In the last step, a buffer volume equivalent to that of labeled EVs was used to maintain the same concentration before and after filtration. The Exosome Spin Column approach was carried out according to the manufacturer's instructions.

CE-LIF of fluorescently labeled EVs and EOF measurement (Paper III)

The fused silica capillary (I.D. of 50 μm, O.D. of 375 μm, effective length (L_{eff}) of 50.2 cm and total length (Lt_{ot}) of 60.2 cm) was pre-conditioned (using a pressure of 172 kPa at the capillary inlet) with the following sequence: water for 10 min, 1 M NaOH for 10 min, 1 M HCl for 10 min and then water for 10 min. The rinsing between two analyses was carried out with 50 mM SDS for 5 min, 1 M NaOH for 5 min, deionized water for 5 min, and finally the running BGE for 5 min using a pressure of 207 kPa. A plug of sample was hydrodynamically injected from the inlet end by applying a pressure of 3.4 kPa for 2 min. The separation was carried out under 25 kV (normal polarity) at 25 °C and the samples were maintained at 5 °C with the sample storage module of the PA 800 Plus equipment. The optimized BGE was composed of Tris/CHES (I = 90 mM, pH 8.4).

The calibration curve was acquired using bovine milk derived EV standards. The EV isolates were diluted with PBS to prepare different initial EV concentrations from 1.65×10^{10} to 1.65×10^{11} EVs/mL before the labeling and matrix removal on spin columns. 20 µL of EVs was mixed with 20 µL of CFDA-SE 200 µM solution (resulting in a final CFDA-SE concentration of 100 µM CFDA-SE), and incubated for 2 h at 37 °C. Then 40 µL of labeled EVs was loaded into EV Spin Columns and recovered in Tris/CHES 90 mM. Calculations for the final concentrations were based on the initial concentrations measured by NTA before the labeling and taking into account a recovery of 75% from the matrix substitution step. EOF mobility was measured with CE-LIF using 4-(4-methoxybenzylamino)-7-nitro-2,1,3-benzoxadiazole (MBD) which is a neutral and fluorescent compound.[282] The EOF marker was dissolved in a DMSO:CH$_3$OH (1:1 v/v) solution to a concentration of 20 mM, and then further diluted to 2 mM in BGE before use.

4.1.6 Characterization of biomacromolecules

Amino acids and glucose extraction from EVs (Paper IV)

CD9$^+$ and CD61$^+$ EV fractions (from IAC-AsFlFFF system) were subjected to preconcentration and salt removal with disposable Nanosep centrifugal devices with 10 kDa molecular weight cutoff membrane filters at 14,000 g for 2 min for each 500 µL fraction at room temperature. The filtrate was discarded. Thereafter, cold acetonitrile (50 µL) was added to the membrane for EV lysis and removal of precipitated proteins. Cold acetonitrile precipitated proteins effectively from human plasma[283] and lysed the lipid bilayer membranes.[284] After vortexing, the filter unit was centrifuged for another 2 min at 14,000 g. The filtrate was then collected, and the ISTD mixture which yielded the final concentration of 1 ppm of amino acids (glycine-2,2-d$_2$, l-phenylalanine-3,3-d$_2$, and l-lysine-4,4,5,5-d$_4$) and 5 ppm of d-fructose-^{13}C$_6$ in Milli-Q water containing 0.1% formic acid was added to the filtrate for HILIC-MS/MS analysis.

Determination of amino acids and glucose by HILIC-MS/MS (Paper IV)

The method used for the determination of amino acids and glucose was based on our previously developed method[285] with some modifications. The column temperature was set to 50 °C. Mobile phase A was acetonitrile with 0.1% formic acid, and mobile phase B was Milli-Q water with 0.1% formic acid. The separation of the target analytes was performed using the following gradient program: 20% B for 15 min (0.4 mL/min), 20–80% B for 5 min (0.3 mL/min), followed by 80–20% B for 3 min (0.3 mL/min). The

injection volume was 3 µL for all samples. The effluent was electrosprayed, ionized (positive and negative mode for amino acids and sugars, respectively), and monitored by MS[2] detection in the multiple reaction monitoring mode (MRM), with the exception of glucose, which was analyzed in the single ion monitoring mode.

Nanoparticle tracking analysis (NTA)

Isolated EV samples were analyzed by Nanosight model LM14 equipped with blue (404 nm, 70 mW) laser and sCMOS camera. The samples were diluted in PBS and three videos of 60 s each were recorded using camera level 14. The data was analyzed using NTA software 3.0 with the detection threshold set at 5 and screen gain set at 10 to maximize the particles tracking with minimal background. (Paper II)

All experiments were carried out with samples diluted in PBS according to input sample concentrations, leading to particle concentrations within the range of 10^7–10^9 particles per mL for optimal analysis. The Zetaview system was equipped with a 488 nm laser. Each experiment was performed in duplicate on 11 different positions within the sample cell with the following specifications and analysis parameters: sensitivity 60, shutter 100, max area 100, min area 5, and min brightness 25. The results were validated while obtaining at least 1000 valid tracks for each run. For data capture and analysis, the NTA Software version 8.05.04 was used. The particle concentrations and size distributions were also determined with a Nanosight NS300 instrument (Malvern, version NTA 3.2 Dev Build 3.2.16) equipped with a 405 nm laser, sCMOS camera type and the NTA software v3.1. The video acquisition was performed using a camera level of 14. Per sample, 3 videos of 90 s with a frame rate of 30 frames/s were captured at 25 °C and subsequently analyzed with a threshold set up at 5. The results were validated with at least 2000 valid tracks for each triplicate. (Paper III)

Protein and cholesterol assays

The amounts of LDL and VLDL-IDL were expressed in terms of the protein concentration. The concentrations including that of anti-apoB-100 mAb were determined by the method of Lowry et al.,[286] DC protein assay, or by the BCA protein assay kit based on bicinchoninic assay (BCA)[287] using BSA as the standard. Molar concentrations of the LDL and the IDL-VLDL were calculated using the molecular weight of apoB-100 (512 kDa). For the anti-apoB-100 mAb, molecular weight of 155 kDa was used. (Papers I-II, IV)

Total cholesterol (free and esterified) concentrations in samples were measured using the Roche Cholesterol CHOD-PAP reagent according to the manufacturer's protocol. The absorbance was measured with an EnSpire multimode plate reader (PerkinElmer) at 510 nm. Calibration curves and sample concentrations were calculated using EnSpire multilabel analyzer version 4.13.3005.1482. (Paper IV)

QCM analysis of anti-apoB-100 mAb – lipoprotein interactions (Paper I)

The measurements started after the waiting period of 20 minutes to stabilize the resonant frequency in the QCM. LDL and IDL-VLDL samples were injected to the surface of chips, monitoring first the association for 50 seconds and then the dissociation for 500 seconds. After each association and dissociation cycle, the biosensor chip was regenerated with injection of 0.28 M ammonium hydroxide (pH 11.5) and re-equilibrated with the analysis buffer.

LDL and IDL-VLDL experiments were all carried out at a flow rate of 50 µL / min with an injection volume of 35 µL. LDL and anti-apoB-100 mAb interactions were studied at temperatures of 25.0, 34.0, 35.0, 36.0, 37.0, 38.0, 39.0, and 40.0 °C. IDL-VLDL and anti-apoB-100 mAb interactions were studied at 37.0 °C. LDL and IDL-VLDL concentrations ranged from 3 to 110 µg/mL. Three repetitions were made to verify the precision of the data. We assumed that the Sauerbrey relation was valid and that the QCM frequency shifts are proportional to the adsorbed amount of solute.[270]

Scanning electron microscopy (SEM) (Paper IV)

Preconcentrated combined fractions of EV subpopulations (produced with IAC-AsFlFFF) were dried on clean polished silicon wafer surfaces. The samples were then coated with a 3 nm Au–Pd alloy using a Cressington 208HR high resolution sputter coater and imaged at 3 kV with secondary electrons.

Transmission electron microscopy (TEM) (Paper II)

The EV isolates produced by the IAC were prepared by negative staining as described earlier.[288] Briefly, EVs were loaded on 200 mesh grids, fixed with 2% PFA, stained with 2% neutral uranyl acetate and embedded in a methyl cellulose uranyl acetate mixture.

Western blotting (Paper II)

Proteins from the IAC isolated EVs were separated by 12% SDS-PAGE and transferred onto polyvinylidene difluoride (PVDF) membranes. A PageRuler prestain

protein ladder of 10–250 kDa was used as the ladder marker. The membranes were then probed with antibodies against TSG101 at 1:500 dilution and CD9 at 1:500 dilution. Proteins of interest were detected with 1:3000 diluted HRP-conjugated sheep anti-mouse IgG antibody and visualized with the Clarity ECL substrate according to the provided protocol.

4.2 Data analysis

Estimation of kinetic rate constants for QCM (Paper I)

Estimation of kinetic rate constants is an inverse problem, i.e., a problem where given the response of the system we want to estimate system parameters. Here we are going to estimate system parameter *distributions* rather than a finite set of system parameter values.

In general, assuming that the total measured response, R_{tot}, of a system can be written as a linear combination of some individual responses r (e.g., R_{tot} is the sum of the responses for all one-to-one interactions for biosensors) we have that

$$R_{tot}(\mathbf{x}) = \sum_{i=1}^{n} a_i \cdot R(\mathbf{p}_i; \mathbf{x}),$$ (11)

where $\mathbf{x}$ is the independent variable(s) for the system, e.g. the analysis time, $\mathbf{p}$ is the system parameter(s), e.g. rate constants, and a is a constant. If we let n in Eq. (11) $\rightarrow \infty$ we get that,

$$R_{tot}(\mathbf{x}) = \int_{\Omega} a(\mathbf{p}) \cdot R(\mathbf{p}; \mathbf{x}) d^m \mathbf{p},$$ (12)

where $\Omega \subseteq \Upsilon^m$ is the considered system parameter space. Eq. (12) is known as an *Inhomogeneous Fredholm Integral Equation* of the first kind with kernel R and our goal is to estimate the function $a(\mathbf{p})$. Assume that we have measured the total response $R_{tot}(\mathbf{x})$ for the system, and discretize Eq. (12), the problem of estimating $a(\mathbf{p})$ can be written as a linear system of the form

$$\mathbf{M}(\mathbf{p}, \mathbf{x}) \cdot \mathbf{a}(\mathbf{p}) = \mathbf{R}_{tot}(\mathbf{x}),$$ (13)

where $\mathbf{M}$ is a matrix and $\mathbf{a}$, $\mathbf{R}_{tot}$ are discrete sample vectors of $a(\mathbf{p})$ and $R_{tot}(\mathbf{x})$, respectively. Eq. (13) is usually an ill-conditioned over- or underdetermined linear system and often the condition $\mathbf{a} \geq \mathbf{0}$ is imposed. In order to get reasonable solutions to Eq. (13) regularization is often used, the most common one is Tikhonov regularization where we instead of Eq. (13) solve the following linear system,

$$\left(\mathbf{M}^T\mathbf{M} + \lambda^2\mathbf{\Gamma}^2\mathbf{\Gamma}\right)\mathbf{a} = \mathbf{M}^T\mathbf{r}_{\text{tot}}, \tag{14}$$

where $\mathbf{\Gamma}$ is a regularization matrix (usually an identity or Laplacian matrix) and λ is a regularization parameter.

For biosensors the kernel R in Eq. (12) can be written,

$$R(t,C;k_a,k_d) = \begin{cases} 0 & , t \le t_0, \\ \dfrac{k_a C}{k_a C + k_d}\left(1 - \exp\left(-(k_a C + k_d)(t - t_0)\right)\right) & , t_0 < t \le t_0 + t_{\text{inj}}, \\ \dfrac{k_a C}{k_a C + k_d}\left(1 - \exp\left(-(k_a C + k_d)t_{\text{inj}}\right)\right) \cdot \exp\left(-k_d\left(t - t_0 - t_{\text{inj}}\right)\right) & , t > t_0 + t_{\text{inj}}, \end{cases} \tag{15}$$

where t (analysis time) and C (analyte concentration) are the independent variables and k_a, (association rate constant) and k_d (disassociation rate constant) are non-negative system parameters. Above t_0 is the time when the injection of the analyte begins and t_{inj} is the injection time. The solution $a(k_a, k_d)$ to Eq. (12) with the kernel in Eq. (15) is known as an *Interaction Map*.[289,290] The Interaction Maps in Paper I were calculated using the TraceDrawer software from Ridgeview Instruments AB, Sweden.

Determination of affinity constants with PF-ACE (Paper I)

To determine the affinity constants for complexes between LDL, ILD-VLDL and anti-apoB-100 mAb, the adsorption energy distribution (AED) calculations were used. First, the LDL or IDL-VLDL fractions, bound to anti-apoB-100 mAb, were established as a function of anti-apoB-100 mAb concentrations. The interactions were studied by injecting anti-apoB-100 mAb with increasing concentrations, followed by a constant LDL or IDL-VLDL concentration and volume. Then the voltage was applied and LDL or IDL-VLDL having more charges than anti-apoB-100 mAb reached the anti-apoB-100 mAb and interacted with it.

The average mobility of the antibody-antigen complex can be described with the following equation,[291]

$$\mu^A = \Theta_f\mu_f + \Theta_b\mu_b \tag{16}$$

where Θ_f and Θ_b are the free and bound fractions of LDL or IDL-VLDL, respectively, and μ_f and μ_b are the mobilities of free and bound LDL or IDL-VLDL to anti-apoB-100 mAb, and μ^A is the average mobility of the complex. Since $\Theta_f + \Theta_b = 1$, the equation of adsorbed fraction can be presented as:

$$\theta_b = \frac{\mu^A - \mu_f}{\mu_b - \mu_f} \qquad (17)$$

Adsorption isotherms and adsorption energy distribution calculations (Paper I)

Adsorption isotherms describe the fraction of analyte adsorbed or in free solution at equilibrium to a constant and specific temperature.[292,293] The Langmuir model that describes adsorption to a limited number of equal adsorption sites can be expressed as:

$$\theta = \frac{K_A C}{1 + K_A C} \qquad (18)$$

where C is the analyte concertation in the running buffer, θ is fractional surface coverage and K_A is the association equilibrium constant. As described above the Langmuir model can only describe one type of interaction. However, many adsorption processes are a result of several different types of interaction such as ion-ion, and hydrophobic interactions. One simple way to model a heterogeneous adsorption process is to use the bi-Langmuir adsorption isotherm. The bi-Langmuir model is just the sum of two Langmuir models, and can be presented as:

$$\theta = \theta_{S,1} \frac{K_{A,1} C}{1 + K_{A,1} C} + \theta_{S,2} \frac{K_{A,2} C}{1 + K_{A,2} C} \qquad (19)$$

Here, indices 1 and 2 denote the first and second adsorption sites, respectively. $\theta_{S,i}$ is the saturation fraction for the i:th site. Observe that $\theta_{S,1} + \theta_{S,2} = 1$. One other way to describe heterogeneous adsorption is to expand the Langmuir adsorption isotherm model into a continuous distribution of independent homogeneous sites across a certain range of adsorption energies as done below,[137,294]

$$\begin{cases} \theta(C) = \int_{K_{A,min}}^{K_{A,max}} f(\ln K_A) \theta(C, K_A) d \ln K_A \\ \theta(C, K_A) = \frac{K_A C}{1 + K_A C} \end{cases} \qquad (20)$$

Here, $\theta(C, K_A)$ is the local adsorption model, and $f(\ln K_A)$ is the adsorption energy distribution (AED). $K_{A,min}$ and $K_{A,max}$ are determined from the inverse maximum and minimum sample concentration used in the CE experiments. In Paper I, the AED is solved using the expectation maximization method, where the integral equation is

iteratively solved.[295] Observe that both the AED in Eq. (20) and Interaction Maps are both *Inhomogeneous Fredholm Integral Equations* of the first kind with kernel $\theta(C, K_A)$, see Eq. (12).

Thermodynamics of the interactions (Paper I)

Linear regression analysis of Eq. (21), called van't Hoff plots can be utilized to determine the temperature independent thermodynamic parameters:

$$\ln K_D = \Delta H/RT - \Delta S/R \tag{21}$$

where K_D is the dissociation equilibrium rate constant, R is the gas constant, T is the temperature, ΔS is the entropy term, and ΔH is the enthalpy term. The interactions can be thermodynamically either entropy driven, enthalpy driven, or have equal contribution of both.[296]

Statistical Analysis (Paper IV)

Different R 3.6.3 statistical analysis tools were used in Paper IV. Skewness and Kurtosis tests for data distribution evaluation, principal component analysis (PCA) for visualization of differences between $CD9^+$ and $CD61^+$ EV subpopulations, and linear discriminant analysis (LDA) for statistical confirmation of these differences, including clarification of the variables involved in the process. Additional studies were also made to evaluate the potential differences between EVs of different sizes (PCA and LDA).[297]

In all of the cases, the concentrations of the free amino acids present in the EVs normalized by the total amount of protein were exploited as input variables for the development of the statistical models. Additional root square transformation was needed to provide normal data distribution of the input variables.

5. RESULTS AND DISCUSSION

The major findings of the research and summary of the research results achieved are presented in this chapter. For the development of fast, reliable, and automated isolation and fractionation methods for nanosized subpopulations of human biomacromolecules, first methods to select appropriate ligands were developed (Paper I). PF-ACE and QCM were employed to study the antibody-antigen interactions between anti-apoB-100 mAb and apoB-100 containing lipoproteins. The PF-ACE gave information on the interactions in solution that reached equilibrium, while QCM gave information on the kinetics of the interactions of immobilized mAb. Adsorption energy distribution calculations were exploited to study interaction heterogeneity and to determine affinity constants for the PF-ACE data, while Interaction maps were for the first time utilized to determine kinetic constants for the QCM data. This information is also important in designing isolation systems based on the IAC, since the antibodies utilized for the isolation of biomacromolecules were covalently immobilized on the monolithic disks via 1,1'-carbonyldiimidazole (CDI) coupling (Papers II-IV).

In addition to the lipoproteins (Papers I and IV), another group of biomacromolecules of interest were the EVs (Papers II-IV). The isolation of the EVs is a challenging task due to their heterogeneity and overlapping size ranges for the EVs of different sources of origin (e.g., co-isolation of ectosomes and endosomes). The matrix of the biomacromolecules poses additional challenges, since it is easier to isolate pure subpopulations of biomacromolecules from cell culture media or urine compared to more complex matrices such as blood plasma or serum. Due to this, the blood plasma was selected as the matrix for the IAC (Papers II-IV), inferring that if the isolation system works for the more complex matrices, it would be suitable for less demanding matrices as well. Further tasks in this thesis regarding the isolation of fragile biomacromolecules were: finding biocompatible chromatographic support material, finding appropriate elution conditions to disrupt the antibody-antigen interactions, and finding a gentle size-based separation technique to complement the affinity-based isolation.

The above-mentioned challenges were resolved by utilizing biocompatible convective interaction media (CIM) monolithic disk columns as stationary phase in the IAC (Papers II-IV). The CIM disks had a pore size large enough for the isolation of biomacromolecules in the size range of 1-200 nm, fitting the size range for the

lipoproteins and the exosome-sized EVs. We also found in Paper I that to disrupt strong antibody-antigen interaction and remove the lipoproteins, highly alkaline elution conditions (pH above 11.3) were needed. These elution conditions are not feasible with silica-based supports unless they are extensively chemically modified to stand for higher pH values. The modified silica-based particles for the isolation of lipoproteins have also been previously studied in our laboratory[298]. However, with the GMA- and EDMA-based polymeric materials utilized in the CIM disks, high pH range could be utilized without deteriorating the support material, thus enabling longer life-time of the isolation system.

Appropriate antibodies were selected to be immobilized on the CIM disks for the isolation of EVs and lipoproteins. Anti-CD61 was exploited to target platelet-derived EVs (Papers II and IV), while anti-CD9 was used to target EVs that have been classically labeled as exosomes (Papers III-IV). Anti-apoB-100 that was characterized in Paper I was beneficial for the isolation of apoB-100 containing lipoproteins. Further size-based fractionation of EV and lipoprotein subpopulations of the IAC isolates were successfully done with AsFlFFF (Papers II-IV). The AsFlFFF was coupled with multiple detectors to elucidate the sizes and to allow further studies of the isolates. NTA, SEM, TEM, and western blot were employed to confirm the successful isolation and morphology of the EVs (Paper II). The IAC isolates were also studied by CE-LIF and compared to those obtained by other popular isolation techniques, such as UC and SEC (Paper III). Subpopulations of EVs were free of lipoproteins (Papers II-IV) that are usually present after isolation carried out by conventional isolation techniques and methods. Finally, the IAC and the AsFlFFF were integrated into an automated IAC-AsFlFFF on-line system. This automated, on-line coupled system proved to be fast and give reproducible isolation and fractionation of lipoprotein and EV subpopulations with on-line characterization by UV, DLS, DAD, and MALS, and fraction collection, allowing further studies to clarify the composition of free amino acids and sugars in subpopulations of EVs by HILIC-MS/MS (Paper IV).

5.1 Studies of antibody lipoprotein interactions by partial filling affinity capillary electrophoresis and continuous quartz crystal microbalance

5.1.1 Lipoprotein and anti-apoB-100 mAb interaction studies by partial filling affinity capillary electrophoresis

PF-ACE was utilized to study the interactions of anti-apoB-100 mAb with LDL (Figure 13A), IDL-VLDL (Figure 13B), and HDL$_2$ (Figure 13C). Based on the electropherogram of HDL$_2$ (Figure 13C) the interaction between HDL$_2$ and the anti-apoB-100 mAb did not result in significant changes in mobility (Figure 13A) since no apoB-100 is present in the HDL$_2$ particles, and the interaction was not expected. This experiment was used as a control to confirm the selectivity of the anti-apoB-100 mAb. The selectivity of the anti-apoB-100 mAb towards apoB-100 containing lipoproteins could be detected even visually from electropherograms (Figures 13 A and B), since P2QVP-b-PEO diblock copolymer coating[280] suppressed the EOF close to zero at the level of 10^{-9} – 10^{-10} m^{2}V^{-1}s^{-1}. The average mobilities (μ^A) of the anti-apoB-100 and LDL or IDL-VLDL complexes were calculated from electropherograms (Figure 13) after deducting the EOF. This resulted in noticeable differences between electrophoretic mobilities of free (μ_f) and bound (μ_b) forms (Figure 14A) that were further investigated with exponential and linear fitting. The free LDL or IDL-VLDL were found at the lower end of the antibody concentration. The maximum value of the electrophoretic mobilities of the forms was reached when the LDL or IDL-VLDL were completely bound to anti-apoB-100 mAb.
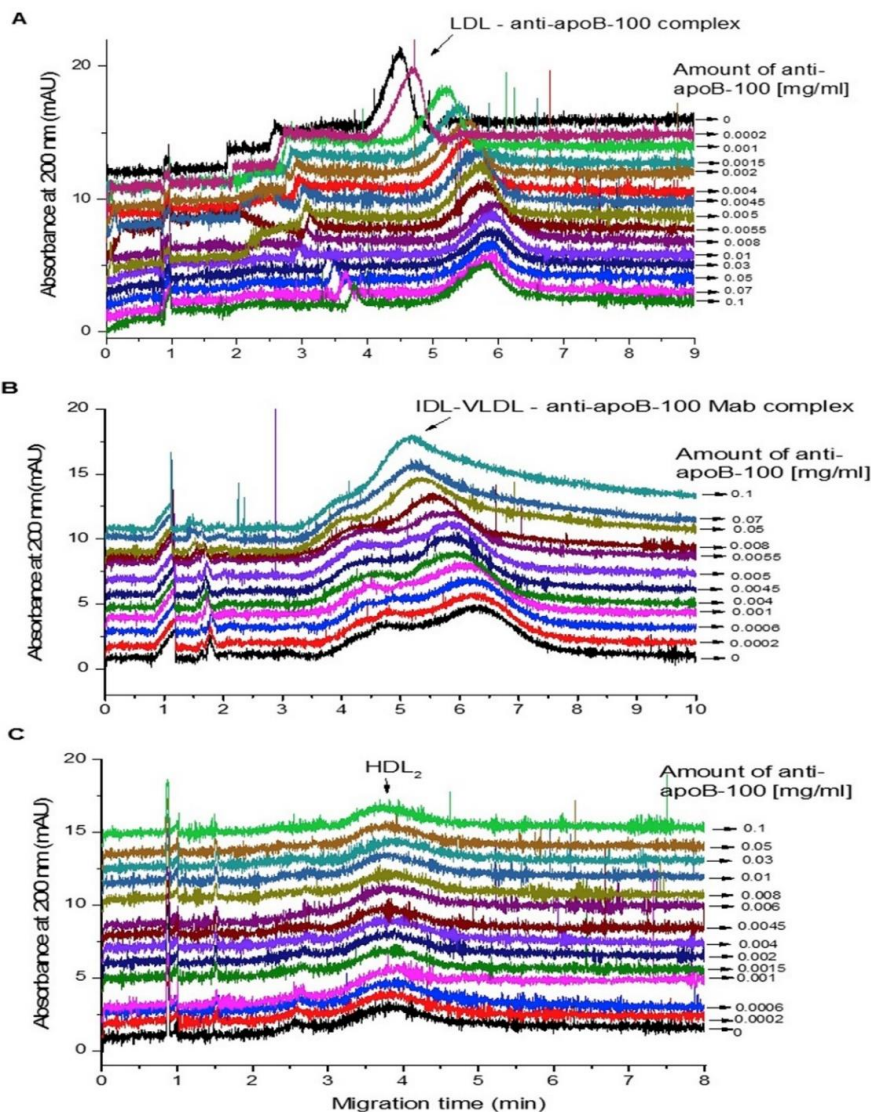
Figure 13. Partial filling affinity capillary electrophoresis electropherograms as a function of concentration of anti-apoB-100 mAb interacting with (A) LDL; (B) IDL-VLDL; and (C) HDL$_2$. Running conditions: -25 kV, the injection time of LDL 2 sec, IDL-VLDL 8 sec, and HDL$_2$ 2 sec, all at 50 mbar, injection time of anti-apoB-100 mAb was 3 sec at 50 mbar, 37 °C, L_{tot} 38.5, L_{det} 30 cm, UV detection 200 nm, BGE phosphate buffer (pH 7.4, I 20 mM), concentrations of LDL 0.075 mg/mL, IDL-VLDL 0.036 mg/ml, and HDL$_2$ 0.2 mg/mL, and anti-apoB-100 mAb concentration ranging from 0.00 to 0.10 mg/mL.

The electrophoretic mobility data was further utilized to form the adsorption isotherm and its corresponding Scatchard plot, and analyzed by AED calculations to provide

information on the heterogeneity of the interactions (Figure 14B). The calculations revealed that while there were minor differences in the antibody's binding affinity between LDL and IDL-VLDL, the interactions were homogeneous when both the lipoproteins and the anti-apoB-100 mAb were free in solution.
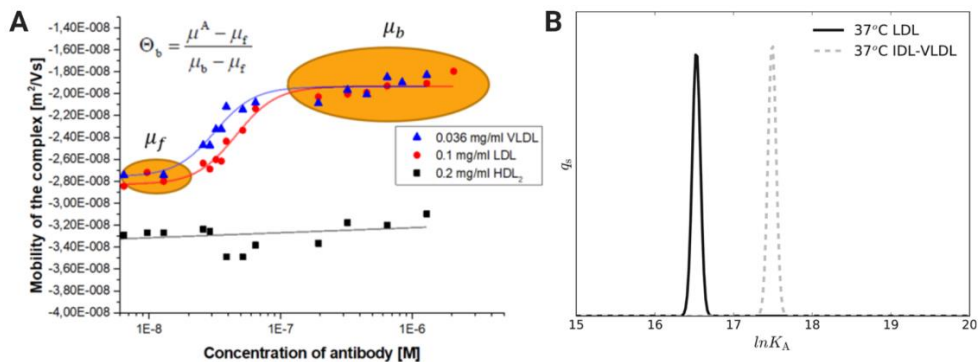

Figure 14. (A) The electrophoretic mobilities of the adsorbed and free fractions (B) AED calculations for LDL, IDL-VLDL and anti-apoB-100 mAb systems at 37 °C.

The temperature of the system was set to 37 °C to resemble the physiological temperature where antibodies bind to lipoproteins in the blood flow. Even though the antibody utilized in this study was produced in mouse against human lipoproteins, PF-ACE could be used to study e.g., how human antibodies interact with animal lipoproteins. Since the aim of this study was to confirm that the strength of the affinity of the antibody was high enough for the isolation of human lipoproteins, the PF-ACE was a valuable technique to support the use of the anti-apoB-100 mAb (Table 7) in the IAC.

5.1.2 Kinetic and thermodynamic study of lipoprotein and anti-apoB-100 mAb interactions with quartz crystal microbalance and interaction maps

To get still further information about the heterogeneity of the interactions, the continuous flow QCM was used. The anti-apoB-100 mAb was immobilized on the surface of the QCM chip while in the PF-ACE system the lipoproteins were flowing freely in a BGE solution. This was an important set up for the future IAC utilization of the anti-apoB-100 mAb, since the anti-apoB-100 mAb would also be immobilized on

the monolithic disk columns used for the IAC. It was found that the interactions did not reach equilibrium (Figures 15 and 16), but showed high affinity as was already shown with the PF-ACE. Thus, a kinetic approach called *Interaction Map*[289,290] (Figures 15-16 A and B) was utilized for interpreting the sensograms (Figures 15-16 C and D). The interaction maps were calculated using the TraceDrawer software from Ridgeview Instruments AB, and confirmed that the LDL - anti-apoB-100 mAb interactions were homogenous with one peak in the interaction map (Figure 15A). The affinity constants were calculated from association and dissociation constants indicated with intense red color in the Figure 15A and B, and were collected in Table 7 for different temperatures. The log K_A at 37°C was 7.96 with QCM, 7.41 with PF-ACE, and 7.64 with SPR (obtained as paid services), which shows both the strong affinity of the antibody towards the LDL and good reproducibility of affinity constants between complementing techniques.
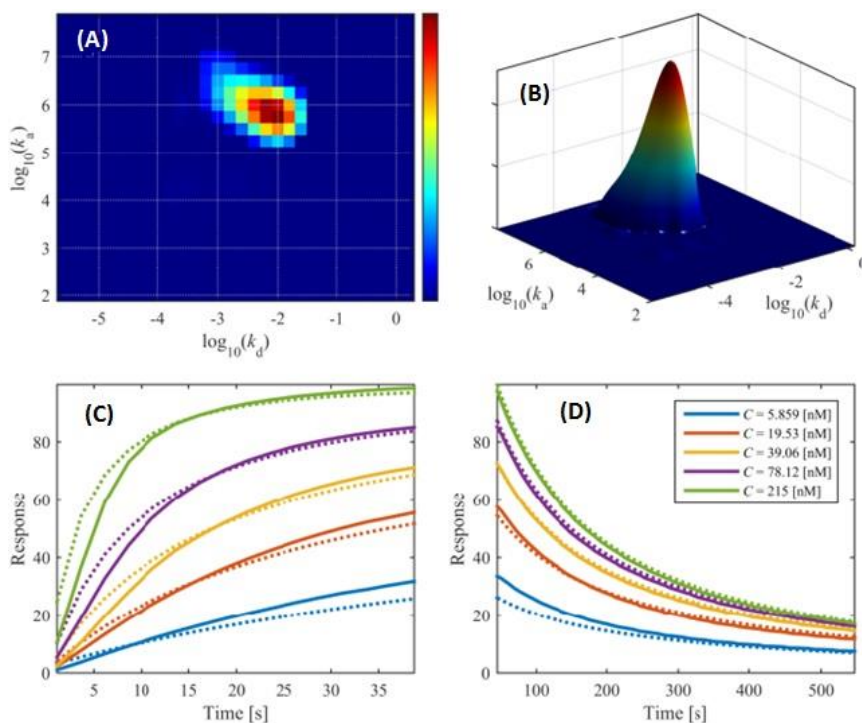

Figure 15. QCM interactions between LDL and anti-apoB-100 mAb at 37 °C presented (A) and (B) as interaction maps, (C) as sensograms and model fits for association, and (D) as sensograms and model fits for dissociation. The dotted curves represent the model fitted sensograms and solid curves those obtained from the experimental data.

Table 7. Effects of temperature on kinetics and affinity data between anti-apoB-100 mAb and LDL interactions obtained by QCM using interaction maps, PF-ACE using AED calculations, and SPR using a 1:1 binding model.

System	Temp. [°C]	K_A [M^{-1}]	log K_A	K_D [nM]	k_a [M^{-1}s^{-1}]	k_d [s^{-1}]
QCM	25	$4.68 \cdot 10^8$	8.67	2.14	$8.13 \cdot 10^5$	$1.74 \cdot 10^{-3}$
	34	$1.45 \cdot 10^8$	8.16	6.92	$7.76 \cdot 10^5$	$5.37 \cdot 10^{-3}$
	35	$1.23 \cdot 10^8$	8.09	8.13	$7.94 \cdot 10^5$	$6.46 \cdot 10^{-3}$
	36	$7.24 \cdot 10^7$	7.86	13.80	$6.92 \cdot 10^5$	$9.55 \cdot 10^{-3}$
	37	$9.02 \cdot 10^7$	7.96	11.09	$8.61 \cdot 10^5$	$9.55 \cdot 10^{-3}$
	38	$7.41 \cdot 10^7$	7.87	13.49	$9.12 \cdot 10^5$	$1.23 \cdot 10^{-2}$
	39	$6.03 \cdot 10^7$	7.78	16.60	$8.51 \cdot 10^5$	$1.41 \cdot 10^{-2}$
	40	$4.57 \cdot 10^7$	7.66	21.88	$8.32 \cdot 10^5$	$1.82 \cdot 10^{-2}$
CE	37	$2.54 \cdot 10^7$	7.41	39.37	ND	ND
SPR *	37	$4.35 \cdot 10^7$	7.64	23.00	$3.92 \cdot 10^5$	$9.01 \cdot 10^{-3}$

ND, not determined. K_A, affinity constant. K_D, dissociation constant. k_a, association rate constant. k_d, dissociation rate constant. * data obtained as paid services.

The interaction map for anti-apoB-100 and IDL-VLDL (Figure 16A) shows additional peak indicating differences in the kinetics, which could potentially be a result of different lipoprotein subpopulations having different association and dissociation rates. In addition, since IDL-VLDL is a mixture of heterogeneous lipoprotein classes with different sizes and molecular weights, the QCM could also detect the different subpopulations due to mass sensitivity. However, more studies would be needed with purified IDL and purified VLDL subpopulations to confirm this. The log K_A at 37 °C was 8.00 for the first interaction and 7.80 for the second, while with PF-ACE it was 7.69 (Table 8). The values were close to those for the interaction between anti-apoB-100 and LDL. This was to be expected, since the apoB-100 is the protein found in both LDL and IDL-VLDL particles and association and dissociation differences might be due to size differences of the lipoprotein subpopulations.

Table 8. Kinetics and affinity data between anti-apoB-100 mAb and IDL-VLDL obtained by QCM using Interaction Maps, and by PF-ACE using AED calculations.

System	Temp [°C]	$K_{A,1}$ [M^{-1}]	log $K_{A,1}$	$K_{D,1}$ [nM]	$k_{a,1}$ [M^{-1}s^{-1}]	$k_{d,1}$ [s^{-1}]	$K_{A,2}$ [M^{-1}]	log $K_{A,2}$	$K_{D,2}$ [nM]	$k_{a,2}$ [M^{-1}s^{-1}]	$k_{d,2}$ [s^{-1}]
QCM	37	$1.00 \cdot 10^8$	8.00	10.00	$5.54 \cdot 10^5$	$5.54 \cdot 10^{-3}$	$6.38 \cdot 10^7$	7.80	15.67	$5.15 \cdot 10^4$	$8.07 \cdot 10^{-4}$
CE	37	$4.94 \cdot 10^7$	7.69	20.24	ND	ND	ND	ND	ND	ND	ND

ND, not determined. Subscripts $_{1 \text{ and } 2}$, represent sites 1 and 2. K_A, affinity constant. K_D, dissociation constant. k_a, association rate constant. k_d, dissociation rate constant.
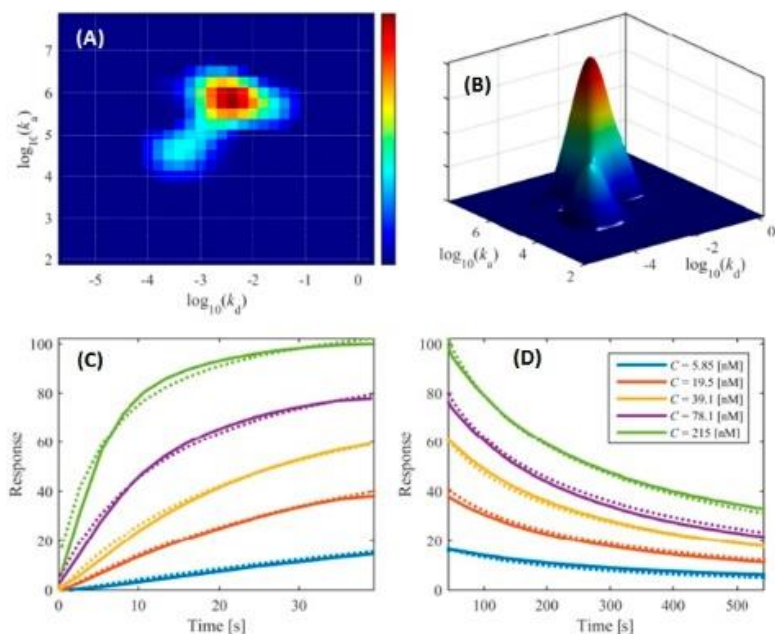
Figure 16. QCM interactions between IDL-VLDL and anti-apoB-100 mAb at 37 °C presented (A) and (B) as interaction maps, (C) as sensograms and model fits for association, and (D) as sensograms and model fits for dissociation. The dotted curves represent the model fitted sensograms and solid curves those obtained from the experimental data.

The QCM data at different temperatures for the LDL were plotted as van't Hoff plot (Figure 17) to obtain information on the thermodynamics of the interactions between LDL and anti-apoB-100 mAb (Table 9). The interactions were found to be predominantly enthalpy driven.
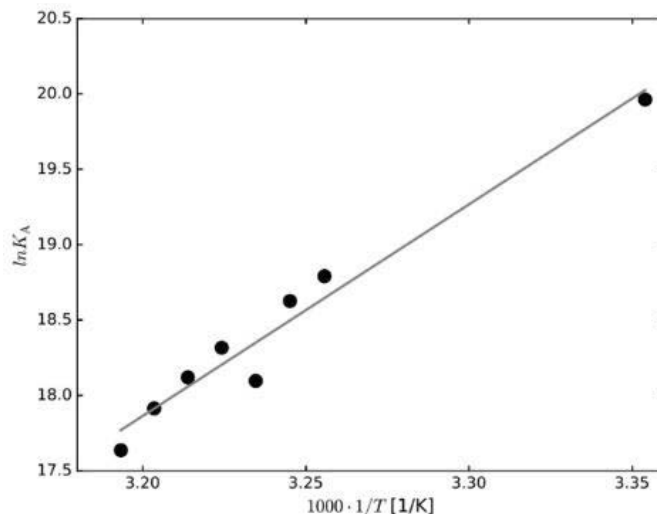
Figure 17. Van't Hoff plot for the interactions between LDL and anti-apoB-100 mAb.

Table 9. The effect of temperature on the derived thermodynamic state functions for the interaction between LDL and anti-apoB-100 mAb measured by QCM.

Temp. [ºC]	$\Delta G°$ [kJ mol^{-1}]	$\Delta H°$ [kJ mol^{-1}]	$\Delta S°$ [J·K^{-1} mol^{-1}]
25	-49.5	-116.7	-225.0
34	-48.0	-116.7	-225.0
35	-47.7	-116.7	-225.0
36	-46.5	-116.7	-225.0
37	-47.2	-116.7	-225.0
38	-46.9	-116.7	-225.0
39	-46.5	-116.7	-225.0
40	-45.9	-116.7	-225.0

Due to the high affinity of the antibody towards both LDL and IDL-VLDL, anti-apoB-100 was selected as the affinity ligand for the following studies where the antibody was immobilized on the monolithic CIM disks and utilized for the isolation of apoB-100 containing lipoproteins from human plasma. Appropriate elution conditions (pH over 11.3) were found for the chip regeneration, which was later applicable also for the removal of biomacromolecules from the monolithic disks in the IAC studies.

5.2 Immunoaffinity chromatography of biomacromolecules

In this thesis, the monolithic CIM disks were selected for the isolation of lipoproteins and EVs by IAC due to their wide pH stability and large pore size, so that even particles that have a diameter of 100 nm could easily pass through the pores. The system was first tested in combination with a syringe pump (Figure 18A) and UV-detector with isocratic sample loading, washing, and elution (Figure 18B). The antibodies utilized in this thesis were covalently immobilized on the monolithic disk utilizing CDI.
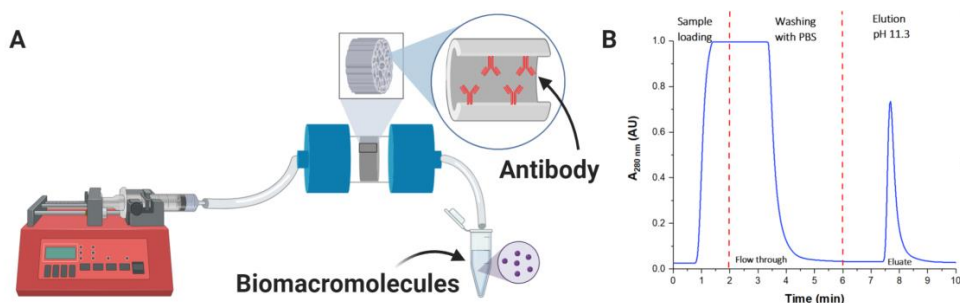

Figure 18. (A) Schematic description of the IAC system and (B) typical isocratic UV-profile of the IAC sample loading, binding, and elution.

The IAC procedure was the following: load the diluted plasma sample to the monolith, wash the non-bound plasma components with PBS, release the biomacromolecules with a solution of pH 11.3 (either ammonium hydroxide or carbonate-bicarbonate solution), and regenerate the column for the next isolation with PBS.

The IAC was first used to isolate platelet-derived vesicles with an anti-CD61 disk from human plasma at different flow rates (Figure 19A) and the isolated platelet-derived EVs were western blotted against common EV markers such as TSG101 and CD9 to confirm that the isolated particles were indeed EVs. In addition, the isolates were imaged with TEM (Figure 19B) showing typical EV morphology. It can also be noted from the TEM that the isolate was dominated by small-sized EVs of under 100 nm.
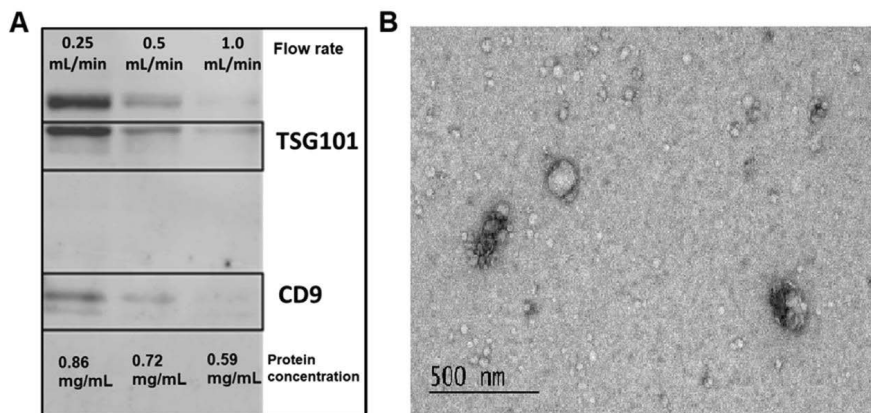
Figure 19. (A) Western blotting and protein concentrations of isolated EVs from plasma with the anti-CD61 disk at flow rates 0.25-1.0 mL/min. (B) TEM morphology of platelet-derived EVs, isolated with anti-CD61 disk. The isolates show vesicles with different diameters and a typical "cup-shaped" EV morphology.

It was found that the protein concentration of the platelet-derived EV isolates depended on the flow rates and to maximize the yield 0.25 mL/min should be preferred. This can also be noticed in the western blot intensities of the TSG101 and the CD9 in Figure 19A. The particle to protein ratio increased a hundred-fold compared to flow through (Table 10). In addition, the isolates from both plasma and from platelet-depleted concentrate derived platelet-free plasma had similar mean sizes indicating a good size reproducibility between different sample matrices.

Table 10. EV isolation yields from plasma and from platelet-depleted concentrate derived platelet-free plasma (PC-PFP). Particle yields and mean sizes were determined with the nanoparticle tracking analysis.

Average	Plasma		Platelet-concentrate derived platelet-free plasma (PC-PFP)	
	Flow through (n=3)	Isolate (n=3)	Flow through (n=2)	Isolate (n=2)
Protein yield (µg mL^{-1})	2637±79	338±72	1147±47	97.7
Mean size (nm)	157±50	174±60	123±61	175±64
Particles (mL^{-1})	9.70±3.26· 10^{10}	1.17±0.41 ·10^{12}	1.51±0.13 ·10^{8}	1.29±0.17 ·10^{9}
Particle:Protein Ratio	3.70±1.32· 10^{7}	3.47±1.02 ·10^{9}	1.32±0.16 ·10^{5}	1.32±0.17 ·10^{7}

5.3 Asymmetrical flow field-flow fractionation of extracellular vesicle subpopulations

The isolates were further fractionated utilizing the AsFlFFF due to its many positive features such as preserving the integrity of the biomacromolecules, this being of importance especially when working with EVs. For example, isolation or fractionation with SEC might deteriorate the EVs due to shear forces from the stationary phase.

The platelet-derived EVs (CD61^{+} EVs) isolated with anti-CD61 disk were manually injected to the AsFlFFF (Figure 20) and the subpopulations of the platelet-derived EVs with size range <130 nm were detected by UV, MALS (Figure 20A) and DLS (Figure 20B) detectors. The size range of isolated platelet-derived EVs corresponded to that of exosomes, which was surprising, since the platelets do not have multivesicular bodies that would produce exosomes. Thus, it was demonstrated with a non-electron microscopy-based method that platelets do indeed secrete exosome-sized EVs to the circulation. Most importantly, we also detected that the platelets secrete EVs of the size of exomeres (<50 nm, 12-17 min) in abundant concentrations based on the UV detector signal. Since platelet-derived EVs originate from α-granules[7,245,247,248] and not from the multivesicular bodies, α- granules might also be the source of origin for platelet-derived exomeres. However, more studies are needed to define the exact mechanism of the biogenesis.

The shape factor (ρ) of CD61^{+} EVs was also determined (Table 11) utilizing the size data obtained with MALS and DLS detectors. Three different size ranges were selected based on the major peak intensities of the flow DLS: <50 nm for exomere-sized, and 60-120 nm for exosome-sized platelet-derived EVs.
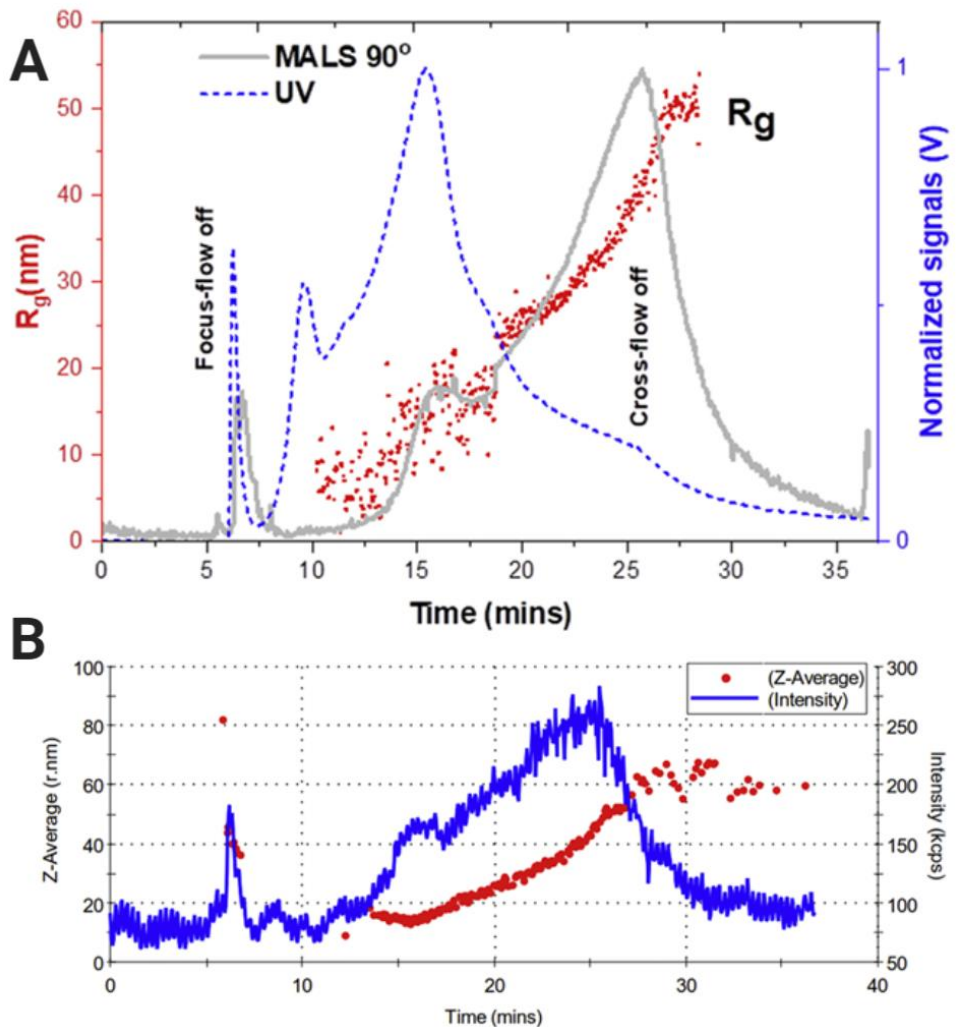
Figure 20. (A) Normalized AsFlFFF-UV (blue dashed line) and AsFlFFF-MALS (grey line) fractograms of isolated CD61$^+$ EVs in PBS, with the root mean square radius of gyration, R_g (red circles). The fractionation conditions utilized were: 350 µm spacer, cross-flow rate of 3 mL/min, detector flow rate 1.0 mL/min, focusing step 5 min, linear decrease in cross-flow to 1.0 mL/min in 5 min, followed by a linear decrease over 15 min to 0 mL/min. The detector flow was applied for 10 min after the cross-flow was off. (B) Raw flow DLS detector signal (blue line) with Z-average or the hydrodynamic radius, R_h (red circles).

Table 11. Shape factor (ρ) of CD61^{+} EVs based on the AsFIFFF fractionation. The MALS detector data was utilized for (D_g) and the flow DLS detector data for (D_h). The hydrodynamic diameter was obtained with Zetasizer software and root mean square diameter of gyration was obtained from the MALS data with the Zimm first order model.

	Exomere-sized	Exosome-sized	
	<50 nm	60-80 nm	90-120 nm
D_g **(nm)**	43.4	64.9	100.5
D_h **(nm)**	45.0	68.5	118.9
ρ= R_g/R_h	0.96	0.95	0.85

Based on the shape factors, the exomere-sized (ρ =0.96) and small exosome-sized (60-80 nm, ρ=0.95) platelet-derived EVs resembled each other in shape even though exosomes have lipid bilayer, opposite to exomeres.[18] Larger exosome-sized platelet-derived EVs on the other hand were closer to ideal homogeneous spheres in shape based on their shape factor (ρ =0.85).

The IAC based isolation was expanded to isolate also the CD9^{+} EVs in addition to the CD61^{+} EVs by immobilizing anti-CD9 on the monolithic CIM disks. The anti-CD9 was selected as an antibody to capture EVs of more "classical" exosome characteristics to compare them to those obtained with the anti-CD61 disk, due to presence of CD9 in the western blots of the CD61^{+} EV isolates (Figure 19A). Both the CD9^{+} and the CD61^{+} EVs were isolated from 250 μL of plasma and fractionated with a quick fractionation sequence with AsFIFFF with an initial plan to reduce the time required for the fractionation. The resulting fractograms (Figure 21) show that the isolates of the anti-CD9 gave two times higher raw DLS detector intensities compare to isolates from the anti-CD61 disk and size ranges of 30-80 nm. Within this size range, the exomere and the small exosome-sized EVs can be found. It was also logical that more of the CD9^{+} EVs were found in the plasma due to CD9 being a common marker for the exosome-sized EVs from different sources of origin, while the CD61^{+} EVs would represent mainly the EVs originating from the platelets. In addition, the platelet-derived EVs have not been commonly detected in the size range of exosomes and below, since they are conventionally found in the size range of microvesicles (50-1000 nm). In addition, both isolates had more particles in the size range of exomeres,

indicating that the blood is an abundant source of exomere-sized EVs. This has not been detected before this thesis, since the studies of exomeres have been mainly concentrating on cell cultures.[18]
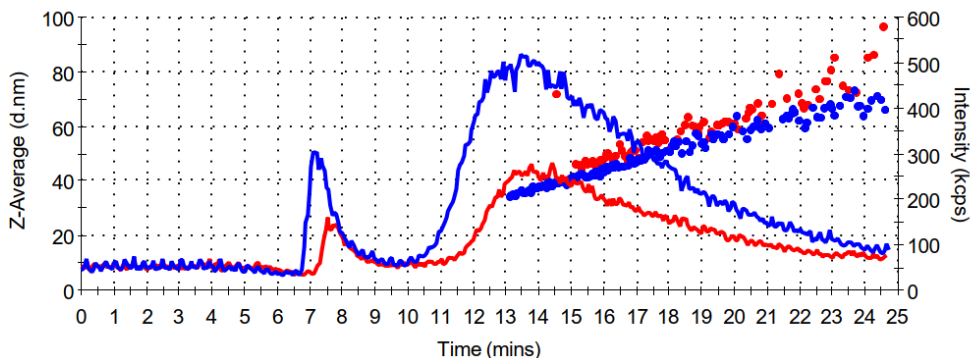

Figure 21. Raw flow DLS detector signal (blue and red lines) with Z-average or the hydrodynamic diameter, D_h (red and blue circles). Red lines and circles represent CD61$^+$ EVs and blue lines and circles represent CD9$^+$ EVs.

Particle yields as determined by the nanoparticle tracking analysis were $26.5 \pm 1.6 \cdot 10^{10}$ mL^{-1} for the CD61$^+$ EVs and $76.1 \pm 3.6 \cdot 10^{10}$ mL^{-1} for the CD9$^+$ EVs, which also complemented the raw DLS detector data showing that there were approximately 3 times more EVs in the isolates from the anti-CD9 disks.

5.3.1 Capillary electrophoresis coupled with laser-induced fluorescent detection of extracellular vesicle subpopulations

A newly developed CE-LIF method for the detection and the separation of EVs was utilized to further study the CD9$^+$ and the CD61$^+$ EVs (Figure 22). The IAC isolation method was also compared to more conventional EV separation techniques such as UC and SEC for samples of different animal and human origin. Three similar EV subpopulations were detected by the CE-LIF (Figure 22) as was detected earlier by the AsFlFFF (Figure 20) for the isolates of the IAC method. Overall, the EV isolates obtained by the IAC had more peaks and higher fluorescence intensities compared to those obtained by other techniques. Significantly (up to 100 times) lower signal in relative fluorescence units (RFUs) was obtained especially when comparing to the EVs isolated by SEC using two times more starting material (500 µL). The highest concentration (based on CE-LIF signal intensity) of the IAC isolated EVs was at 17

min. Other subpopulations were found at 10 and 12 min. The peak at 10-12 min became more intense for the CD9^{+} EVs compared to that for the CD61^{+} EVs. Due to the lack of reference material, it was not possible to draw conclusions on the precise size and charge of the EV subpopulations, but since the peak from 13 min onwards was not found in isolates achieved by other isolation techniques, it could potentially be assigned to the exomere-sized EVs isolated by IAC, since other techniques are not known to isolate the exomere-sized particles with the isolation parameters selected in our study.

The effort was made to get reference material for different sized EVs by combining size fractions of the isolates from the runs shown in Figure 21. Diluted fractions from the fast AsFlFFF method were lyophilized and analyzed with CE-LIF (marked with dashed lines for the exomere-sized EVs of size <50 nm in Figure 22). In addition, we could confirm that the AsFlFFF fractionated EVs were still preserved even after the lyophilization. However, it was noticed that the faster AsFlFFF method was not suitable to separate subpopulations sufficiently compared to the slower one (Figure 20). The effect of the two elution solutions, ammonium hydroxide and carbonate-bicarbonate solution, used in IAC on the LIF were also studied. The CFDA-SE labeling was less efficient with ammonium hydroxide-based EV isolates due to conversion of the CFDA-SE into side products in the presence of ammonium/amine groups. Thus, we could confirm that the carbonate-bicarbonate solution was the best elution solution for labeling purposes.
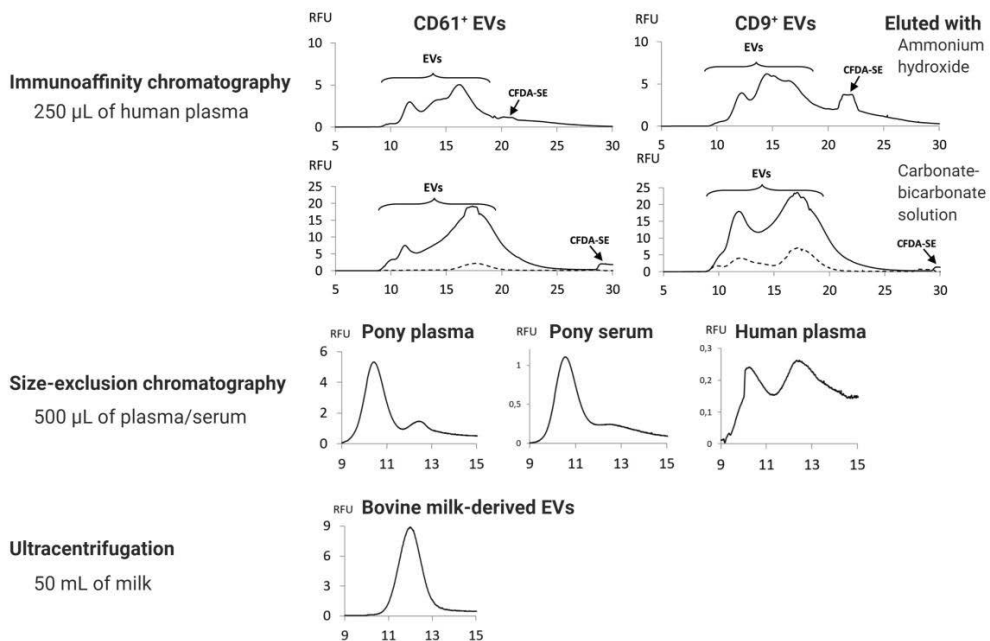
Figure 22. CE-LIF electropherograms for fluorescently labeled EVs (matrix removal with Exosome Spin Columns (MW 3000)). The EVs were purified from bovine milk, pony plasma, pony serum, and human plasma. BGE: Tris / CHES (I = 90 mM, pH 8.4). EVs isolated with the IAC are represented by continuous lines, while the dashed lines represent the EV < 50 nm fractions further fractionated with the AsFlFFF after the IAC elution step. The CE-LIF of the EVs (in PBS) derivatized with the CFDA-SE, using ISF BGE Tris / CHES (pH 8.4). Other CE conditions were: uncoated fused silica capillary with I.D. of 50 µm, effective length (L_{eff}) of 50.2 cm and total length (L_{tot}) of 60.2 cm, applied voltage: +25 kV, and hydrodynamic injection at 3.4 kPa for 2 min. LIF detection with λ_{ex} = 488 nm, λ_{em}: 520 nm.

5.4 Development of on-line immunoaffinity chromatography - asymmetrical flow field-flow fractionation system

Success with the IAC and the AsFlFFF methods led us to further improve the system by combining them on-line (Figure 23) for the isolation and fractionation of subpopulations of the biomacromolecules. This on-line system had an automated sample introduction to the monolithic disk (Figure 23A), including the control of the isolation and washing of the monolithic disk (Figure 23B), injection of the isolated sample to the AsFlFFF for the size-based fractionation (Figure 23C), and characterization by different detectors (Figure 23D).
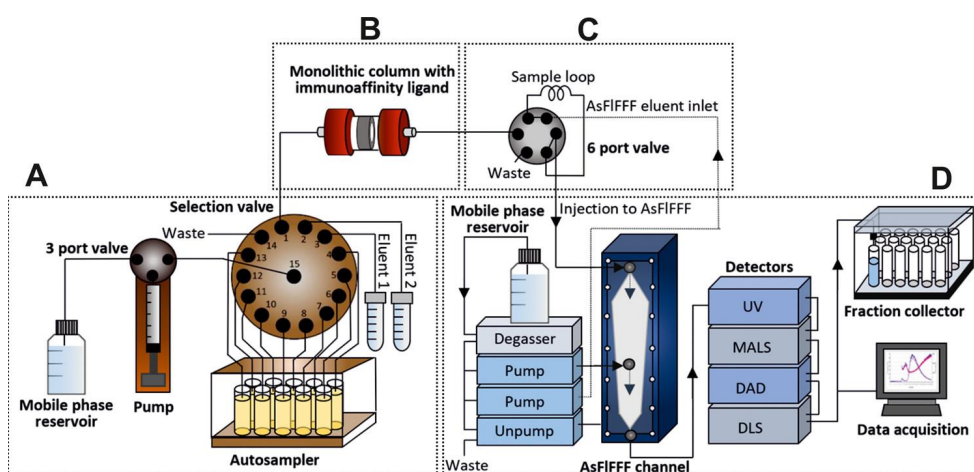
Figure 23. Automated on-line system for the isolation of nanosized biomacromolecules. The system consisted of (A) a selection valve for controlling the isolation process, (B) a monolithic column for the IAC, (C) an automated six port valve for injection to the AsFlFFF, and (D) the AsFlFFF with UV, MALS, DAD, and DLS detectors, and a fraction collector.

The system was designed to isolate and fractionate the EVs and the lipoproteins from one of the most complex biofluids, blood plasma, but the system is also applicable to less complex biofluids. With this automated on-line system aggregation,[122,299] operator dependent errors,[300] oxidation, shear and mechanical stress, and contamination,[301] can be reduced or even eliminated. The automated on-line system allowed significant reduction in time with less man power. In addition, the quality of the data was better, the system was cost-effective, and produced well-controlled final products.

5.4.1 Application of the on-line system to isolation and fractionation of subpopulation of lipoproteins and extracellular vesicles

The initial optimization of the on-line IAC-AsFlFFF system was carried out with the anti-apoB-100 disk that was selected based on studies in Paper I and since it was easier to detect lipoproteins than EVs due to their higher amounts in human plasma. UC-isolated LDL was used for the optimization of the six-port valve timer that connected IAC to AsFlFFF. The time 125 s (Figure 24) was used for all the subsequent experiments. It was already at this stage noticed that the UV peak areas gave good repeatabilities of 0.3-6.6%.
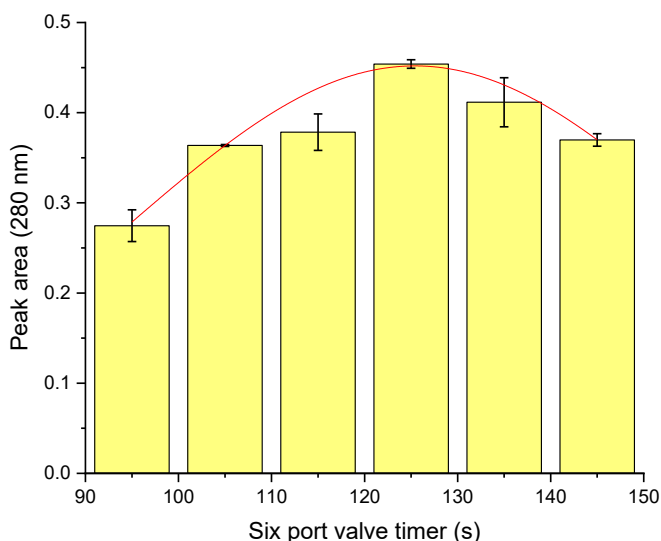
Figure 24. Times for a six-port valve timer of IAC isolated 100 µg/mL LDL eluted in AsFlFFF based on UV 280 nm peak areas (n=25).

Then the next step was to get the best recovery for apoB-100 containing lipoproteins with the focus being on small-dense LDL (sdLDL). UC-isolated LDL (1 mL, c=250 µg/mL) was isolated and fractionated in triplicate (RSD 6.6%) with the IAC-AsFlFFF system by the anti-apoB-100 disk. The density range of these LDL isolates were 1.019–1.050 g/mL, they excluded very small sdLDL that can be found at the densities

of 1.050-1.063 g/mL.[189,222,223] The IAC-AsFlFFF isolated and fractionated LDL (Figure 25A, 10-15 min) had a hydrodynamic diameter size range of 24-28 nm confirming that the sdLDL and especially very small sdLDL were no present in the UC-isolated sample (the size range for sdLDLs is according to different techniques 16.7-25.8 nm[214–217]). The DAD detector could also detect carotenoids (11-18 min) that were present in the core of the LDL (430-500 nm).[299] This emphasized the importance of DAD in the IAC-AsFlFFF system as a quality control detector for the EVs, since the conventional isolation methods often yield EVs with LDL contaminants. Fractionated LDL isolates were also assayed with DC protein assay and showed 99.6% recovery, and the samples contained 0.43 ± 0.01 mg of cholesterol.

The system applied to isolating the apoB-100 containing lipoproteins from human plasma (Figure 25B) gave excellent RSDs for UV peak areas (0.84%, n=3) and size ranges covered all apoB-100 lipoproteins (LDL, IDL, and VLDL) and excluded other lipoproteins such as HDL. Most importantly the system was able to isolate sdLDLs from the human plasma (retention time 11-12 min).
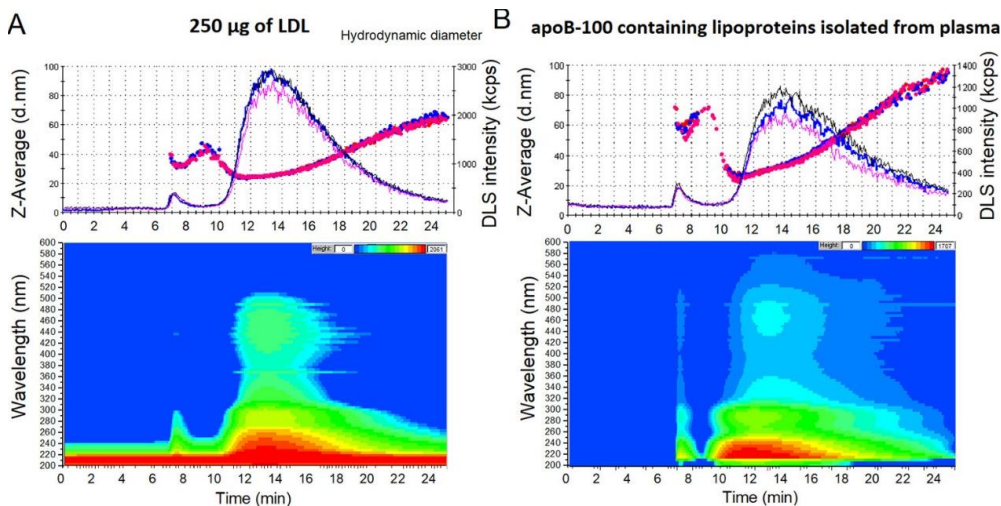
Figure 25. IAC-AsFlFFF analysis profiles after fractionating the anti-apoB-100 monolithic disk isolates. Technical replicates (*n* = 3) of raw flow DLS data, the hydrodynamic diameter (dots as Z-Average) on the top, and isoabsorbance plot of selected runs in the bottom, (A) of preisolated LDLs by UC and (B) apoB-100 containing lipoproteins isolated from human plasma.

The sdLDL fraction can be used e.g., for further functional studies where the intact particles are needed. The carotenoids were also present in a broader area in the

isoabsorbance plot indicating that also bigger particles (IDL and VLDL) in size up to 95 nm contained carotenoids (Figure 25B, 10-15 min).

The on-line system was then applied to study subpopulations of EVs (Figure 26). Two separate disks were prepared: anti-CD9 and anti-CD61. The CD9 antibody was utilized to isolate the CD9^{+} EVs in the size range of exosomes,[1,302,303] while the CD61 was used to isolate the platelet-derived CD61^{+} EVs. Based on our results with anti-CD9 and anti-CD61 disks from Papers II and III, we divided the subpopulations to the following size groups: <50 nm for the size range of exomeres,[18] and 50–80 and 80–120 nm for the size ranges of exosomes. These size ranges were suitable in IAC for the monolithic disk columns that had a pore size diameter of 1.3 μm.

We could immediately identify that our EV fractions did not contain contaminating lipoproteins since no carotenoids were detected by the DAD as shown in Figure 26A. The concentrations of EVs in the exosomal size range were higher for the isolates of the anti-CD9 disk (Figure 26B). Both the CD9^{+} and the CD61^{+} EVs also contained significant concentrations of exomere-sized EVs (<50 nm). The on-line system could reproducibly (RSD of UV-peak areas for CD9^{+} EVs were 2.9% and CD61^{+} EVs 4.2%) isolate and fractionate the EV subpopulations, which were also detected with FESEM (Figure 26C) with size ranges that agreed with hydrodynamic radiuses obtained by the DLS detector (Figure 26A). Surprisingly, the exomere-sized EVs that have been reported to contain low amounts of tetraspanin CD9 and integrins like CD61[18] were detected from both plasma isolates in relatively high amounts. The reason for this was that the samples in the other studies originated from cell lines and cell cultures, whereas in this work, the monolithic IAC disks isolated every type of exomere-sized CD9^{+} and CD61^{+} EVs that ended up in the blood circulation. Thus, the results show relatively high exomere-sized EV concentrations for both of the disks utilized in the thesis. The fractionated samples were pooled to their assigned size ranges and their zeta potentials were studied (Figure 27). We found that the CD9^{+} < 50 nm EVs had a mean charge of −14.1 mV, while for the exosome-sized subpopulations 50-80 nm and 80-120 nm, the corresponding values were -16.2 mV and -16.9 mV, respectively. The CD61+ < 50 nm subpopulation had a mean charge of −15.1, and −14.2 mV for the exosome-sized subpopulations of 50–80 nm, and −16.6 mV for 80–120 nm. The results agreed with the zeta potentials reported by other groups for the cell culture exomeres and exosomes, fractionated by AsFlFFF.[18]

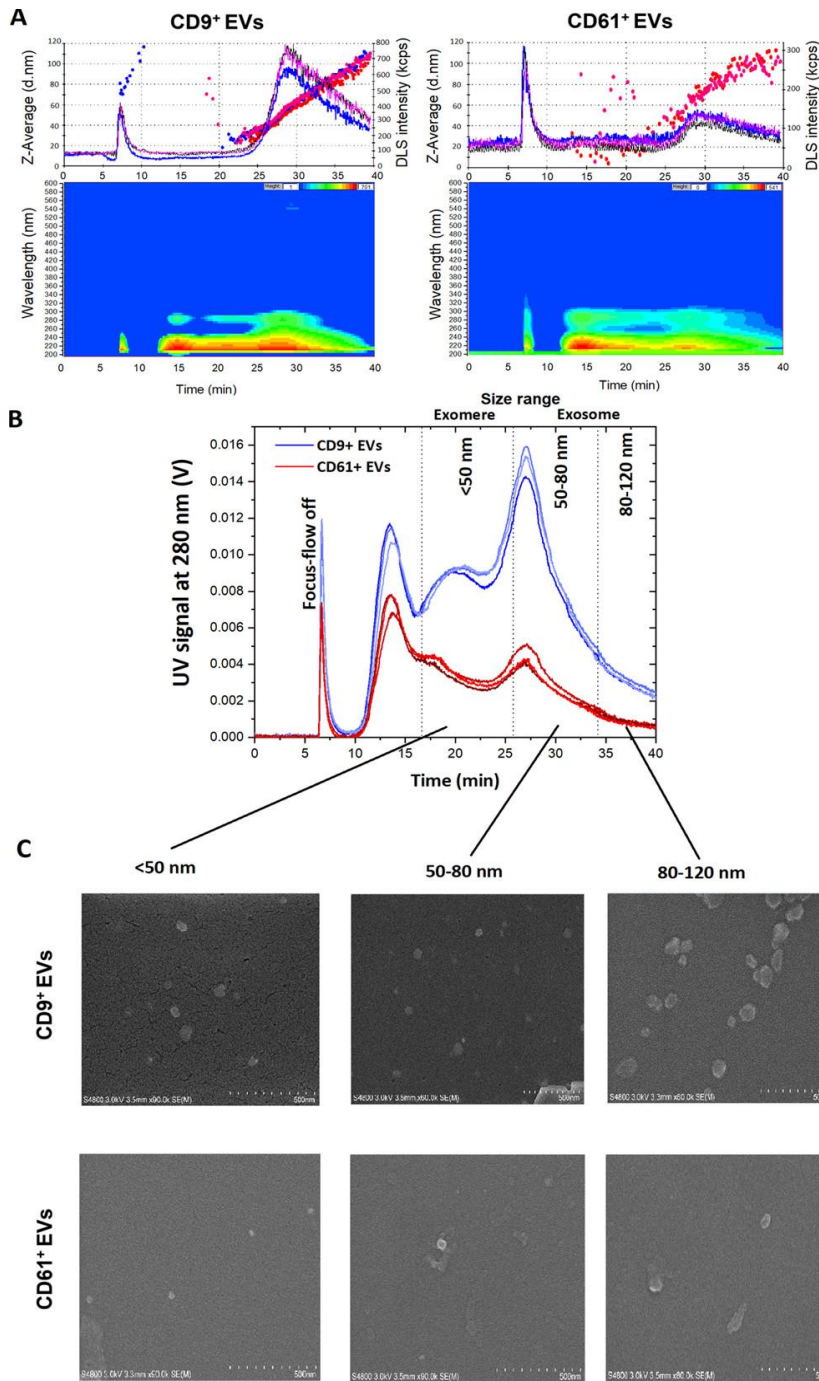**Figure 26.** IAC-AsFlFFF analysis profiles after fractionating the CD9+ and CD61+ EV isolates. Technical replicates (n = 3) of raw flow DLS data, the hydrodynamic diameter (dots as *Z*-Average) on top, and (A) isoabsorbance plot of the selected run at the bottom. (B) Overlaid UV spectra (280 nm) from the technical replicates, and (C) FESEM morphology of fractionated subpopulations for CD9+ and CD61+ EVs.
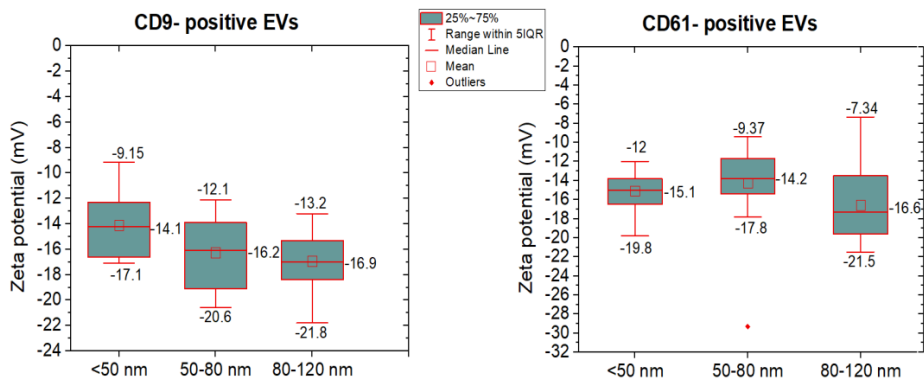
Figure 27. Zeta potential of the CD9^{+} and the CD61^{+} EV subpopulations.

The IAC-AsFlFFF system proved to be faster and more selective for the isolation and fractionation of subpopulations of lipoproteins and EVs compared to conventional isolation techniques and methods,[66] most of which are not even capable of isolating the subpopulations. The system was able to process 38 lipoprotein samples / 24h and 18 EV samples / 24h with the optimized time program. The MALS and DLS detectors coupled on-line with the AsFlFFF were able to give real time size information of the fractions, the UV detector was used for concentration, and DAD for qualitative information on the contaminants. The system was also highly repeatable, with low oxidation, contamination, and sample losses, resulting in productivity increase for the instruments and the personnel. The quality of the data was also improved significantly compared to the systems used in Papers II and III.

The isolated CD9^{+} and CD61^{+} EV subpopulations were studied further to find out the composition of the free amino acids and glucose found inside the subpopulations. EVs carry amino acids and other small metabolites[304] that are involved in physiological activities, and thus the analyzed concentrations might have diagnostic relevance in addition to fundamental understanding of the role of the EVs in the physiology. The study was done by extracting the free amino acids and glucose and analyzing them with HILIC-MS/MS (Figure 28). The differences between the CD9^{+} and the CD61^{+} EV subpopulations are found in Figure 28A. From the free amino acids, Ser was the most abundant. Ser is known to be important in the membrane lipid synthesis of e.g., sphingolipids and phosphatidylserine that have also been found in exosomal membranes.[305,306] The small exosomes (50-80 nm) of the CD61^{+} EVs contained the highest concentrations of free amino acids compared to the other subpopulations of the CD61^{+} EVs. For the CD9^{+} EVs the highest concentrations were

found in the large exosomes (80-120 nm). In addition, regardless of antibody used for the isolation, the Ser content of the exomere-sized EVs (<50 nm) was smallest, supporting the finding (Zhang et al.[18]) that exomeres do not have a lipid bilayer.

With the principal component analysis (PCA, Figure 28B) it was found that there were clear differences between the $CD9^+$ and the $CD61^+$ EVs. While with linear discriminant analysis (LDA, Figure 28C), with 93% samples correctly classified, it was found that the differences between the $CD9^+$ and the $CD61^+$ EVs were due to the following amino acids: Ala, Gly, Lys, Phe, Ser, Thr, and Val. The $CD9^+$ EVs had lower levels of Ala, Gly, and Thr, compared to the $CD61^+$ EVs. This suggested that the $CD61^+$ EVs may take part in gluconeogenesis, since amino acids Ala, Cys, Gly, Ser, and Thr can be directly converted to pyruvate.[307] The Ala and the Gly are also important in immune response inhibiting apoptosis,[308] and act as anti-inflammatory and immunomodulatory agents.[309] Since the $CD61^+$ EVs originated from platelets, these findings further support their potential role in the inflammation and the immunity-related tasks after being released from platelets into the circulation. Irrespective of the origin of the EVs, the small exosome-sized EV subpopulations (50-80 nm) contained Ala, Gly, Ser, and Thr (Figure 28D), suggesting that these subpopulation sizes are preferred in the gluconeogenesis related tasks.

Even further analysis of differences between subpopulations among the $CD9^+$ and the $CD61^+$ EVs were investigated (Figures 28E-H). Here as well we detected differences with the PCA (Figures 28 E and G) and the LDA models, with samples 90% (for $CD9^+$) and 100% (for $CD61^+$) classified. In the $CD61^+$ EVs Cys, Gly, Phe, Ser, and Thr were those free amino acids contributing to the differences between the subpopulations (highest levels in the 50-80 nm subpopulation), while Asn, Cit, Glu, Lys, Phe, and Ser were the amino acids contributing to the $CD9^+$ EVs (highest levels in the 80-120 nm subpopulation). The differences between compositions of the subpopulations also reflect their distinct origins.

The glucose levels of the EVs were also studied. All $CD61^+$ EV subpopulations contained glucose in the concentration range of pmol/mL and are also possibly involved in the gluconeogenesis based on their free amino acid composition. In the $CD9^+$ EVs, glucose was found only in the 50-80 nm subpopulation, which was also the preferred size for the gluconeogenesis based on the free amino acid composition (Figure 28D). With on-line IAC-AsFlFFF it was thus possible to isolate and fractionate the exomere- and the exosome-sized EVs for further studies. The on-line system is a viable tool for the study of the role of EV subpopulations in human physiology. The

fractions can potentially also be produced for therapeutic purposes. Additional applications are linked to the biomarker and composition studies of different biomacromolecules.
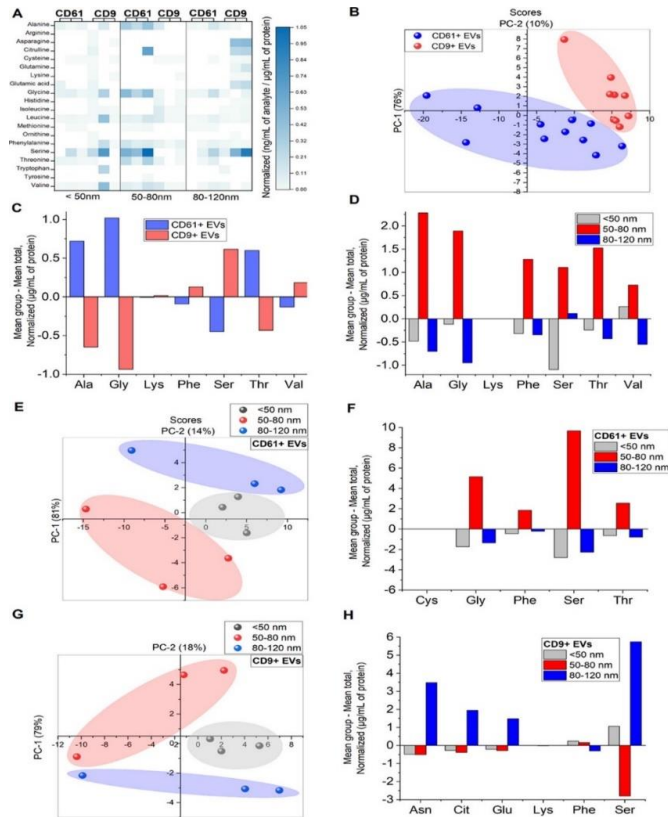
Figure 28. Multivariate analysis of amino acids found in the CD61⁺ and the CD9⁺ EV subpopulations. (A) Heat map visualization of amino acids corresponding to their normalized concentrations (ng/mL per µg/mL of total protein). (B) Scoring plot of PCA analysis showing differences between CD61⁺ and CD9⁺ EVs. (C) Discriminant analysis of differences between amino acids found in CD61⁺ and CD9⁺ EVs. (D) Discriminant analysis of differences between amino acids found between different sizes of combined EV subpopulations. (E) Scoring plot of PCA analysis revealing differences between subpopulations of different sizes of CD61⁺ EVs. (F) Discriminant analysis of differences between amino acids found between CD61⁺ EV subpopulations. (G) Scoring plot of PCA analysis revealing differences between subpopulations of different sizes of CD9⁺ EVs. (H) Discriminant analysis of differences between amino acids found between CD9⁺ EV subpopulations.

6. CONCLUSIONS

The aim of this doctoral thesis was to develop methods and techniques for the isolation of subpopulations of lipoproteins and EVs from human plasma. Antibody-antigen interactions (immunoaffinity) were exploited to capture these biomacromolecules, by utilizing carefully clarified antibody-antigen interaction information. The final target was to have fast, reliable, and versatile methods that can be easily automated for minute sample amounts.

PF-ACE and QCM were employed to study interactions between the anti-apoB-100 monoclonal antibody and apoB-100 containing lipoprotein subpopulations. The PF-ACE was combined with AED calculations and the QCM with Interaction Maps to successfully study the affinity, kinetics, and thermodynamics of the anti-apoB-100 mAb and apoB-100 containing lipoprotein complex formation. With the thermodynamic studies we could demonstrate that LDL and the anti-apoB-100 Mab interactions were enthalpy-driven. The interaction maps were for the first time used to visualize the QCM data, and they provided insight into the association and dissociation phenomena behind the antigen-antibody complex formation at different temperatures. It was found that the dissociation rate constant increased 10-folds from 25 °C to 40 °C. No temperature effect on the association rate constant was noticed. The interaction maps could distinguish two distinct kinetic parameters for the interaction of IDL-VLDL and the anti-apoB-100 Mab. PF-ACE with the AED calculations confirmed that the interactions were homogenous with only a single site adsorption model needed to explain the complex formation. In addition, the results obtained with PF-ACE agreed well with those achieved with QCM, indicating that both techniques are reliable in the biomolecular interaction studies.

Next step was to develop IAC method to isolate platelet-derived (CD61$^+$) EV subpopulations. For the first time polymeric monolithic disk columns were used for the IAC-based isolation of the EVs and their subpopulations from human plasma. The anti-CD61 CIM disks enabled fast isolation, carried out in under 10 min at a flow rate of 1.0 mL/min with 5 mL of diluted plasma sample. However, lower flow rates were found to be optimal, since they resulted in higher yields. It was also possible to regenerate the disk for even hundreds of isolations reducing the relative cost of the disk. For higher EV yields, the monolithic disk can be loaded with a higher amount of the antibody or a better optimization scheme is needed to select the best plasma sample volumes and flow rates. For some specific applications of the EV isolates, an

additional concentrating step will be needed. The isolates were studied further with AsFlFFF combined with MALS and flow DLS detectors, and for the first time the evidence for the existence of platelet-derived EVs in the size range of exomeres and exosomes (<100 nm) was obtained.

After successful implementation of the IAC for the EV isolation, the technique was compared with UC and SEC. The isolated CD9^{+} and CD61^{+} EVs in the size range of exomeres and exosomes were labeled and characterized with the newly developed CE-LIF method. The mass/charge-based separation of EVs was achieved by CE-LIF. The EV isolates obtained by IAC gave more peaks and higher fluorescence intensities compared to those achieved by other techniques. Especially the EVs isolated by SEC, having two times more starting material (500 µL of plasma), gave significantly (up to 100 times) lower signal in relative fluorescence units (RFUs). The IAC isolates also had higher RFUs compared to those isolated by UC.

Positive results achieved with IAC and AsFlFFF inspired us to successfully combine these techniques into an automated on-line IAC-AsFlFFF system for isolation and fractionation of exomere- and exosome-sized EVs, and apoB-100 containing lipoprotein subpopulations. The system was equipped with DAD that could e.g., detect if the EV subpopulation isolates were lipoprotein-free. With the on-line coupled IAC-AsFlFFF it was possible to have fast, reliable, and reproducible isolation and fractionation of challenging biomacromolecules from human plasma with a high purity and high yields of subpopulations. The system could process 18-38 samples in 24h with only minor operator involvement. In addition, AsFlFFF allowed gentle fractionation of lipoproteins and EVs. We could detect EV subpopulations in the size range of exomeres and exosomes, based on DLS and MALS data and confirmed by FESEM. The system was also able to fractionate sdLDL from other LDL subclasses. The surface charges of exomere-sized EV subpopulations were in agreement with the zeta potentials found in the literature for exomeres. Finally, the pooled EV fractions were subjected to metabolite (amino acid and sugar) composition analysis for CD9^{+} and CD61^{+} EV subpopulations. The statistical analysis with PCA and LDA revealed that there were significant differences between the origins of EVs and between subpopulations. The on-line IAC-AsFlFFF system is applicable for the isolation of any biomacromolecules of interest and their subpopulations if the suitable antibody is available for the IAC.

7. REFERENCES

1. Kalluri, R. & LeBleu, V. S. The biology, function, and biomedical applications of exosomes. *Science (80-.).* **367**, eaau6977 (2020).
2. Villa, F., Quarto, R. & Tasso, R. Extracellular Vesicles as Natural, Safe and Efficient Drug Delivery Systems. *Pharmaceutics* **11**, 557 (2019).
3. Zhuang, X. *et al.* Treatment of brain inflammatory diseases by delivering exosome encapsulated anti-inflammatory drugs from the nasal region to the brain. *Mol. Ther.* **19**, 1769–1779 (2011).
4. Castaman, G., Yu-Feng, L. & Rodeghiero, F. A bleeding disorder characterised by isolated deficiency of platelet microvesicle generation [25]. *Lancet* vol. 347 700–701 (1996).
5. Satta, N., Toti, F., Fressinaud, E., Meyer, D. & Freyssinet, J.-M. Scott syndrome: an inherited defect of the procoagulant activity of platelets. *Platelets* **8**, 117–124 (1997).
6. Hugel, B. *et al.* Elevated levels of circulating procoagulant microparticles in patients with paroxysmal nocturnal hemoglobinuria and aplastic anemia. *Blood* **93**, 3451–3456 (1999).
7. Gasecka, A., Nieuwland, R. & Siljander, P. R.-M. Platelet-Derived Extracellular Vesicles. *Platelets* 401–416 (2019) doi:10.1016/B978-0-12-813456-6.00022-9.
8. Lopez, E., Srivastava, A. K., Burchfield, J. & Wang, Y. W. Platelet-derived-extracellular Vesicles promote Hemostasis and prevent the Development of Hemorrhagic Shock. *Sci. Rep.* **9**, 1–10 (2019).
9. Zaldivia, M. T. K., McFadyen, J. D., Lim, B., Wang, X. & Peter, K. Platelet-Derived Microvesicles in Cardiovascular Diseases. *Frontiers in Cardiovascular Medicine* vol. 4 74 (2017).
10. Guo, S. C. *et al.* Exosomes derived from platelet-rich plasma promote the re-epithelization of chronic cutaneous wounds via activation of YAP in a diabetic rat model. *Theranostics* **7**, 81–96 (2017).
11. Dovizio, M., Bruno, A., Contursi, A., Grande, R. & Patrignani, P. Platelets and extracellular vesicles in cancer: diagnostic and therapeutic implications. *Cancer Metastasis Rev.* **37**, 455–467 (2018).
12. Tabas, I., Williams, K. J. & Borén, J. Subendothelial lipoprotein retention as the initiating process in atherosclerosis: Update and therapeutic implications. *Circulation* vol. 116 1832–1844 (2007).
13. Libby, P., Ridker, P. M. & Hansson, G. K. Progress and challenges in translating the biology of atherosclerosis. *Nature* **473**, 317–325 (2011).
14. Fan, J. *et al.* Small dense LDL cholesterol is associated with metabolic syndrome traits independently of obesity and inflammation. *Nutr. Metab.* **16**, 1–9 (2019).
15. Ivanova, E. A., Myasoedova, V. A., Melnichenko, A. A., Grechko, A. V. & Orekhov, A. N. Small Dense Low-Density Lipoprotein as Biomarker for Atherosclerotic Diseases. *Oxid. Med. Cell. Longev.* **2017**, (2017).
16. Gandham, S. *et al.* Technologies and Standardization in Research on Extracellular Vesicles. *Trends in Biotechnology* vol. 2020 (2020).
17. Colao, I. L., Corteling, R., Bracewell, D. & Wall, I. Manufacturing Exosomes: A Promising Therapeutic Platform. *Trends in Molecular Medicine* vol. 24 242–256 (2018).
18. Zhang, H. *et al.* Identification of distinct nanoparticles and subsets of extracellular vesicles by asymmetric flow field-flow fractionation. *Nat. Cell Biol.* **20**, 332–343 (2018).
19. Redgrave, T. G., Roberts, D. C. K. & West, C. E. Separation of plasma lipoproteins by density-gradient ultracentrifugation. *Anal. Biochem.* **65**, 42–49 (1975).
20. Araldi, R. P. *et al.* Bovine papillomavirus isolation by ultracentrifugation. *J. Virol. Methods* **208**, 119–124 (2014).
21. Momen-Heravi, F. Isolation of Extracellular Vesicles by Ultracentrifugation. *Methods Mol. Biol.* **1660**, 25–32 (2017).
22. Takov, K., Yellon, D. M. & Davidson, S. M. Comparison of small extracellular vesicles isolated from plasma by ultracentrifugation or size-exclusion chromatography: yield, purity and functional potential. *J. Extracell. Vesicles* **8**, 1560809 (2019).
23. Berensmeier, S. Magnetic particles for the separation and purification of nucleic acids. *Applied Microbiology and Biotechnology* vol. 73 495–504 (2006).
24. Hong, C. S., Muller, L., Boyiadzis, M. & Whiteside, T. L. Isolation and Characterization of CD34+ Blast-Derived Exosomes in Acute Myeloid Leukemia. *PLoS One* **9**, e103310 (2014).
25. Sharma, P., Diergaarde, B., Ferrone, S., Kirkwood, J. M. & Whiteside, T. L. Melanoma cell-derived exosomes in plasma of melanoma patients suppress functions of immune effector cells. *Sci. Rep.* **10**, 92 (2020).
26. Rodriguez, E. L. *et al.* Affinity chromatography: A review of trends and developments over the past 50 years. *Journal of Chromatography B: Analytical Technologies in the Biomedical and Life Sciences* vol. 1157 122332 (2020).
27. Petersen, K. E. *et al.* Exosome Isolation: Cyclical Electrical Field Flow Fractionation in Low-Ionic-Strength Fluids. *Anal. Chem.* **90**, 12783–12790 (2018).
28. Shiri, F. *et al.* Characterization of Human Glioblastoma versus Normal Plasma-Derived Extracellular Vesicles Preisolated by Differential Centrifugation Using Cyclical Electrical Field-Flow Fractionation. *Anal. Chem.* **92**, 9866–9876 (2020).
29. Heath, N. *et al.* Rapid isolation and enrichment of extracellular vesicle preparations using anion exchange chromatography. *Sci. Rep.* (2018) doi:10.1038/s41598-018-24163-y.
30. Notarangelo, M. *et al.* Ultrasensitive detection of cancer biomarkers by nickel-based isolation of polydisperse extracellular vesicles from blood. *EBioMedicine* **43**, 114–126 (2019).
31. Marczak, S. *et al.* Simultaneous isolation and preconcentration of exosomes by ion concentration polarization. *Electrophoresis* **39**, 2029–2038 (2018).
32. Yu, F., Zhao, Q., Zhang, D., Yuan, Z. & Wang, H. Affinity Interactions by Capillary Electrophoresis: Binding, Separation, and Detection. *Analytical Chemistry* vol. 91 372–387 (2019).
33. Zhang, Y. *et al.* High-Efficiency Separation of Extracellular Vesicles from Lipoproteins in Plasma by Agarose Gel Electrophoresis. *Anal. Chem.* **92**, 7493–7499 (2020).

34. Ayala-Mar, S., Perez-Gonzalez, V. H., Mata-Gómez, M. A., Gallo-Villanueva, R. C. & González-Valdez, J. Electrokinetically Driven Exosome Separation and Concentration Using Dielectrophoretic-Enhanced PDMS-Based Microfluidics. *Anal. Chem.* **91**, 14975–14982 (2019).

35. Lewis, J. *et al.* A Pilot Proof-Of-Principle Analysis Demonstrating Dielectrophoresis (DEP) as a Glioblastoma Biomarker Platform. *Sci. Rep.* (2019) doi:10.1038/s41598-019-46311-8.

36. Kim, Y. B., Yang, J. S., Lee, G. Bin & Moon, M. H. Evaluation of exosome separation from human serum by frit-inlet asymmetrical flow field-flow fractionation and multiangle light scattering. *Anal. Chim. Acta* **1124**, 137–145 (2020).

37. Oeyen, E. *et al.* Ultrafiltration and size exclusion chromatography combined with asymmetrical-flow field-flow fractionation for the isolation and characterisation of extracellular vesicles from urine. *J. Extracell. Vesicles* **7**, 1490143 (2018).

38. Roda, B. *et al.* Field-flow fractionation in bioanalysis: A review of recent trends. *Analytica Chimica Acta* vol. 635 132–143 (2009).

39. Woo, H.-K. *et al.* Exodisc for Rapid, Size-Selective, and Efficient Isolation and Analysis of Nanoscale Extracellular Vesicles from Biological Samples. *ACS Publ.* **11**, 1360–1370 (2017).

40. Liang, L. G. *et al.* An integrated double-filtration microfluidic device for isolation, enrichment and quantification of urinary extracellular vesicles for detection of bladder cancer. *Sci. Rep.* **7**, 1–10 (2017).

41. Tulkens, J., De Wever, O. & Hendrix, A. Analyzing bacterial extracellular vesicles in human body fluids by orthogonal biophysical separation and biochemical characterization. *Nat. Protoc.* **15**, 40–67 (2020).

42. Liu, F. *et al.* The Exosome Total Isolation Chip. *ACS Publ.* **11**, 10712–10723 (2017).

43. Coenen-Stass, A. M. L. *et al.* Extracellular microRNAs exhibit sequence-dependent stability and cellular release kinetics. *Taylor Fr.* **16**, 696–706 (2019).

44. Xu, X. *et al.* Management of Tamm–Horsfall Protein for Reliable Urinary Analytics. *Proteomics - Clin. Appl.* **13**, (2019).

45. Smith, J. T. *et al.* Integrated nanoscale deterministic lateral displacement arrays for separation of extracellular vesicles from clinically-relevant volumes of biological samples. *Lab Chip* **18**, 3913–3925 (2018).

46. Zeming, K. K., Salafi, T., Shikha, S. & Zhang, Y. Fluorescent label-free quantitative detection of nano-sized bioparticles using a pillar array. *Nat. Commun.* (2018) doi:10.1038/s41467-018-03596-z.

47. Hattori, Y., Shimada, T., Yasui, T., Kaji, N. & Baba, Y. Micro- and Nanopillar Chips for Continuous Separation of Extracellular Vesicles. *Anal. Chem.* **91**, 6514–6521 (2019).

48. Baranyai, T. *et al.* Isolation of exosomes from blood plasma: Qualitative and quantitative comparison of ultracentrifugation and size exclusion chromatography methods. *PLoS One* **10**, (2015).

49. Shukuya, T. *et al.* Circulating MicroRNAs and Extracellular Vesicle–Containing MicroRNAs as Response Biomarkers of Anti–programmed Cell Death Protein 1 or Programmed Death-Ligand 1 Therapy in NSCLC. *J. Thorac. Oncol.* **15**, 1773–1781 (2020).

50. Povero, D. *et al.* Characterization and Proteome of Circulating Extracellular Vesicles as Potential Biomarkers for NASH. *Hepatol. Commun.* **4**, 1263–1278 (2020).

51. Monguió-Tortajada, M. *et al.* Extracellular-Vesicle Isolation from Different Biological Fluids by Size-Exclusion Chromatography. *Curr. Protoc. Stem Cell Biol.* **49**, (2019).

52. Asghari, M. *et al.* Oscillatory Viscoelastic Microfluidics for Efficient Focusing and Separation of Nanoscale Species. *ACS Nano* **14**, 422–433 (2020).

53. Vicente, F. A., Plazl, I., Ventura, S. P. M. & Žnidaršič-Plazl, P. Separation and purification of biomacromolecules based on microfluidics. *Green Chemistry* vol. 22 4391–4410 (2020).

54. Wasserberg, D. & Jonkheijm, P. Acoustic Trapping of Proteins under Physiological Conditions. *ACS Central Science* vol. 4 950–951 (2018).

55. Ku, A. *et al.* Acoustic Enrichment of Extracellular Vesicles from Biological Fluids. *Anal. Chem.* **90**, 8011–8019 (2018).

56. Rezeli, M. *et al.* Comparative Proteomic Analysis of Extracellular Vesicles Isolated by Acoustic Trapping or Differential Centrifugation. *Anal. Chem.* **88**, 8577–8586 (2016).

57. Deregibus, M. C. *et al.* Charge-based precipitation of extracellular vesicles. *Int. J. Mol. Med.* **38**, 1359–1366 (2016).

58. Burstein, M., Scholnick, H. R. & Morfin, R. Rapid method for the isolation of lipoproteins from human serum by precipitation with polyanions. *J. Lipid Res.* **11**, 583–595 (1970).

59. Huang, S., Wang, L., Bruce, T. F. & Marcus, R. K. Isolation and quantification of human urinary exosomes by hydrophobic interaction chromatography on a polyester capillary-channeled polymer fiber stationary phase. *Anal. Bioanal. Chem.* **411**, 6591–6601 (2019).

60. Wang, L., Bruce, T. F., Huang, S. & Marcus, R. K. Isolation and quantitation of exosomes isolated from human plasma via hydrophobic interaction chromatography using a polyester, capillary-channeled polymer fiber phase. *Anal. Chim. Acta* **1082**, 186–193 (2019).

61. Coumans, F. A. W. *et al.* Methodological Guidelines to Study Extracellular Vesicles. *Circ. Res.* **120**, 1632–1648 (2017).

62. An, M., Wu, J., Zhu, J. & Lubman, D. M. Comparison of an Optimized Ultracentrifugation Method versus Size-Exclusion Chromatography for Isolation of Exosomes from Human Serum. *J. Proteome Res.* **17**, 3599–3605 (2018).

63. Cho, S., Yang, H. C. & Rhee, W. J. Development and comparative analysis of human urine exosome isolation strategies. *Process Biochem.* **88**, 197–203 (2020).

64. Karimi, N. *et al.* Detailed analysis of the plasma extracellular vesicle proteome after separation from lipoproteins. *Cell. Mol. Life Sci.* **75**, 2873–2886 (2018).

65. Mathieu, M., Martin-Jaular, L., Lavieu, G. & Théry, C. Specificities of secretion and uptake of exosomes and other extracellular vesicles for cell-to-cell communication. *Nature Cell Biology* vol. 21 9–17 (2019).

66. Liangsupree, T., Multia, E. & Riekkola, M.-L. Modern isolation and separation techniques for extracellular vesicles. *J. Chromatogr. A* **1636**, 461773 (2021).

67. German, J. B., Smilowitz, J. T. & Zivkovic, A. M. Lipoproteins: When size really matters. *Current Opinion in Colloid and Interface Science* vol. 11 171–183 (2006).

68. Walters, R. R. Affinity Chromatography. *Anal. Chem.* **57**, (1985).
69. Pfaunmiller, E. L. *et al.* Affinity Chromatography. in *Analytical Separation Science* 461–482 (Wiley-VCH Verlag GmbH & Co. KGaA, 2015). doi:10.1002/9783527678129.assep019.
70. Hage, D. *Handbook of affinity chromatography*. (CRC Press, 2005).
71. Reichelt, S. *Affinity Chromatography*. vol. 1286 (Springer New York, 2015).
72. Hage, D. S. & Matsuda, R. Affinity chromatography: A historical perspective. *Methods Mol. Biol.* **1286**, 1–19 (2015).
73. Starkenstein, E. Ferment action and the influence upon it of neutral salts. *Biochem. Z* **24**, 210–218 (1910).
74. D'Alessandro, G. & Sofia, F. The adsorption of antibodies from the sera of syphilitics and tuberculosis patients. *Z Immunitats* **84**, 237–250 (1935).
75. Meyer, K. & Pic, A. The Isolation of Antibody by Fixation to Adsorbant-Antigen System and Subsequent Dissociation. *Ann. Inst. Pasteur* **56**, 401–412 (1936).
76. Landsteiner, K. & Van Der Scheer, J. On cross reactions of immune sera to azoproteins. *J. Exp. Med.* **63**, 325–339 (1936).
77. Erhan, S., Northrup, L. & Leach, F. A method potentially useful for establishing base sequences in codewords. *Proc. Natl. Acad. Sci. U. S. A.* **53.3**, 646 (1965).
78. Sander, E. G., McCormick, D. B. & Wright, L. D. Column chromatography of nucleotides over thymidylatecellulose. *J. Chromatogr. A* **21**, 419–423 (1966).
79. Bautz, E. K. & Hall, B. D. The isolation of T4-specific RNA on a DNA-cellulose column. *Proc. Natl. Acad. Sci. U. S. A.* **48**, 400–408 (1962).
80. Cuatrecasas, P., Wilchek, M. & Anfinsen, C. B. Selective enzyme purification by affinity chromatography. *Proc. Natl. Acad. Sci. U. S. A.* **61**, 636–643 (1968).
81. Kubota, K., Kubo, T., Tanigawa, T., Naito, T. & Otsuka, K. New platform for simple and rapid protein-based affinity reactions. *Sci. Rep.* **7**, 178 (2017).
82. Mallik, R., Xuan, H. & Hage, D. S. Development of an affinity silica monolith containing α1-acid glycoprotein for chiral separations. *J. Chromatogr. A* **1149**, 294–304 (2007).
83. Cabrera, K. Applications of silica-based monolithic HPLC columns. *Journal of Separation Science* vol. 27 843–852 (2004).
84. Arora, S., Saxena, V. & Ayyar, B. V. Affinity chromatography: A versatile technique for antibody purification. *Methods* vol. 116 84–94 (2017).
85. Hollis, D. F., Suen, E., Shorr, R. G. L., Ralston, S. & Cooke, N. Fast affinity chromatography using small particle silica-based packing materials. *J. Liq. Chromatogr.* **10**, 2349–2368 (1987).
86. Jiang, T., Mallik, R. & Hage, D. S. Affinity monoliths for ultrafast immunoextraction. *Anal. Chem.* **77**, 2362–2372 (2005).
87. Mallik, R. & Hage, D. S. Affinity monolith chromatography. *Journal of Separation Science* vol. 29 1686–1704 (2006).
88. Pfaunmiller, E. L., Paulemond, M. L., Dupper, C. M. & Hage, D. S. Affinity monolith chromatography: A review of principles and recent analytical applications. *Analytical and Bioanalytical Chemistry* vol. 405 2133–2145 (2013).
89. Li, Z., Rodriguez, E., Azaria, S., Pekarek, A. & Hage, D. S. Affinity monolith chromatography: A review of general principles and applications. *Electrophoresis* **38**, 2837–2850 (2017).
90. Martinović, T. *et al.* Affinity chromatography on monolithic supports for simultaneous and high-throughput isolation of immunoglobulins from human serum. *Electrophoresis* **38**, 2909–2913 (2017).
91. Shin, M. J., Tan, L., Jeong, M. H., Kim, J. H. & Choe, W. S. Monolith-based immobilized metal affinity chromatography increases production efficiency for plasmid DNA purification. *J. Chromatogr. A* **1218**, 5273–5278 (2011).
92. Multia, E. Interpreting the biosensor data of biomolecular interactions. (2017).
93. Tear, J. Y. C. Isolation and Detection of Extracellular Vesicles. (2017).
94. Liangsupree, T. Affinity monolith chromatography in the isolation and separation of biomacromolecules. (2018).
95. Moser, A. C. & Hage, D. S. Immunoaffinity chromatography: An introduction to applications and recent developments. *Bioanalysis* vol. 2 769–790 (2010).
96. Phillips, T. High-performance immunoaffinity chromatography: an introduction. *LC Mag* **3**, 962–972 (1985).
97. Calton, G. J. Immunosorbent Separations. *Methods Enzymol.* **104**, 381–387 (1984).
98. Ehle, H. & Horn, A. Immunoaffinity chromatography of enzymes. *Bioseparation* **1**, 97–110 (1990).
99. Wilchek, M., Bocchinif, M., Becker, V. & Givol, D. A General Method for the Specific Isolation of Peptides Containing Modified Residues, Using Insoluble Antibody Columns. *Biochem.* **10**, 2828–2834 (1971).
100. Phillips, T. M. Isolation and recovery of biologically active proteins by high performance immunoaffinity chromatography. *Recept. Biochem. Methodol* **14**, 129–154 (1989).
101. Bailon, P., Roy, S. K. & Swapan, K. Recovery of Recombinant Proteins by Immunoaffinity Chromatography. **427**, 150–167 (1990).
102. Nakajima, M. & Yamaguchi, I. Purification of plant hormones by immunoaffinity chromatography. *Kagaku Seibutsu* **29**, 270–275 (1991).
103. Ueda, K. *et al.* Antibody-coupled monolithic silica microtips for highthroughput molecular profiling of circulating exosomes. *Sci. Rep.* **4**, (2014).
104. Trbojevic-Akmacic, I. *et al.* Chromatographic monoliths for high-throuput immunoaffinity isolation of transferrin from human plasma. *Croat. Chem. Acta* **89**, (2016).
105. Giddings, J. C. A New Separation Concept Based on a Coupling of Concentration and Flow Nonuniformities. *Sep. Sci.* **1**, 123–125 (1966).
106. Giddings, J. C., Yang, F. J. & Myers, M. N. Flow Field-Flow Fractionation: A Versatile New Separation Method. *Science (80-.).* **193**, 1244–1245 (1976).
107. Giddings, J. C., Yang, F. J. & Myers, M. N. Theoretical and Experimental Characterization of Flow Field-Flow Fractionation. *Anal. Chem.* **48**, 1126–1132 (1976).
108. Schimpf, M. E., Caldwell, K. & Giddings, J. C. *Field-flow fractionation handbook*. (John Wiley & Sons, 2000).

109. Liu, M.-K., Li, P. & Giddings, J. C. Rapid protein separation and diffusion coefficient measurement by frit inlet flow field-flow fractionation. *Protein Sci.* **2**, 1520–1531 (1993).

110. Granger, J., Dodds, J., Leclerc, D. & Midoux, N. Flow and diffusion of particles in a channel with one porous wall: Polarization chromatography. *Chem. Eng. Sci.* **41**, 3119–3128 (1986).

111. Wahlund1, K.-G. & Giddings, J. C. *Properties of an Asymmetrical Flow Field-Flow Fractionation Channel Having One Permeable Wall. Anal. Chem* vol. 59 https://pubs.acs.org/sharingguidelines (1987).

112. Sitar, S. *et al.* Size Characterization and Quantification of Exosomes by Asymmetrical-Flow Field-Flow Fractionation. *Anal. Chem.* **87**, 9225–9233 (2015).

113. Yohannes, G. *et al.* Thermal aggregation of bovine serum albumin studied by asymmetrical flow field-flow fractionation. *Anal. Chim. Acta* **675**, 191–198 (2010).

114. Litzén, A. & Wahlund, K. G. Improved separation speed and efficiency for proteins, nucleic acids and viruses in asymmetrical flow field flow fractionation. *J. Chromatogr. A* **476**, 413–421 (1989).

115. Yang, J. S., Lee, J. C., Byeon, S. K., Rha, K. H. & Moon, M. H. Size Dependent Lipidomic Analysis of Urinary Exosomes from Patients with Prostate Cancer by Flow Field-Flow Fractionation and Nanoflow Liquid Chromatography-Tandem Mass Spectrometry. *Anal. Chem.* **89**, 2488–2496 (2017).

116. Wu, B. *et al.* Separation and characterization of extracellular vesicles from human plasma by asymmetrical flow field-flow fractionation. *Anal. Chim. Acta* **1127**, 234–245 (2020).

117. Zhang, H. & Lyden, D. Asymmetric-flow field-flow fractionation technology for exomere and small extracellular vesicle separation and characterization. *Nat. Protoc.* **14**, 1027–1053 (2019).

118. Frank, J. *et al.* Extracellular vesicles protect glucuronidase model enzymes during freeze-drying. *Sci. Rep.* **8**, 12377 (2018).

119. Pužar Dominkuš, P. *et al.* PKH26 labeling of extracellular vesicles: Characterization and cellular internalization of contaminating PKH26 nanoparticles. *Biochim. Biophys. Acta - Biomembr.* **1860**, 1350–1361 (2018).

120. Yohannes, G. Asymmetrical flow field-flow fractionation in the study of water-soluble macromolecules. (2007).

121. Yohannes, G. *et al.* Thermal aggregation of bovine serum albumin studied by asymmetrical flow field-flow fractionation. *Anal. Chim. Acta* **675**, 191–198 (2010).

122. Yohannes, G. *et al.* Miniaturization of asymmetrical flow field-flow fractionation and application to studies on lipoprotein aggregation and fusion. *Anal. Biochem.* **354**, 255–265 (2006).

123. Moon, M. H. & Giddings, J. C. Size distribution of liposomes by flow field-flow fractionation. *J. Pharm. Biomed. Anal.* **11**, 911–920 (1993).

124. Korgel, B. A., Van Zanten, J. H. & Monbouquette, H. G. Vesicle size distributions measured by flow field-flow fractionation coupled with multiangle light scattering. *Biophys. J.* **74**, 3264–3272 (1998).

125. Wahlund, K. G. & Litzén, A. Application of an asymmetrical flow field-flow fractionation channel to the separation and characterization of proteins, plasmids, plasmid fragments, polysaccharides and unicellular algae. *J. Chromatogr. A* **461**, 73–87 (1989).

126. Pitkänen, L., Tuomainen, P. & Eskelin, K. Analysis of plant ribosomes with asymmetric flow field-flow fractionation Field-Flow Fractionation. *Anal. Bioanal. Chem.* **406**, 1629–1637 (2014).

127. D'Ulivo, L. Capillary electrochromatography : a versatile instrumental technique for nanodomain interaction studies. (2010).

128. Lipponen, K. Development of Modern Biosensing Methods and Systems for Biomolecular Interaction Studies. (2014).

129. Witos, J. Sophisticated Instrumental Techniques to Elucidate the Molecular Properties of Human Surface Nanodomains. (2015).

130. D'Ulivo, L., Yohannes, G., Öörni, K., Kovanen, P. T. & Riekkola, M. L. Open tubular capillary electrochromatography: A new technique for in situ enzymatic modification of low density lipoprotein particles and their protein-free derivatives. *Analyst* **132**, 989–996 (2007).

131. D'Ulivo, L. *et al.* In situ delipidation of low-density lipoproteins in capillary electrochromatography yields apolipoprotein B-100-coated surfaces for interaction studies. *Anal. Biochem.* **383**, 38–43 (2008).

132. D'Ulivo, L., Witos, J., Öörni, K., Kovanen, P. T. & Riekkola, M.-L. CEC: A tool for mimicking collagen–surface interactions with apolipoprotein B-100 peptides. *Electrophoresis* **30**, 3838–3845 (2009).

133. D'Ulivo, L., Saint-Guirons, J., Ingemarsson, B. & Riekkola, M. L. Quartz crystal microbalance, a valuable tool for elucidation of interactions between apoB-100 peptides and extracellular matrix components. *Anal. Bioanal. Chem.* **396**, 1373–1380 (2010).

134. D'Ulivo, L., Witos, J., Öörni, K., Kovanen, P. T. & Riekkola, M. L. Open tubular capillary electrochromatography: A useful microreactor for collagen I glycation and interaction studies with low-density lipoprotein particles. *Anal. Chim. Acta* **664**, 185–189 (2010).

135. Lipponen, K. *et al.* Three different approaches for the clarification of the interactions between lipoproteins and chondroitin-6-sulfate. *Anal. Chem.* **83**, 6040–6046 (2011).

136. Lipponen, K. *et al.* Capillary electrochromatography and quartz crystal microbalance, valuable techniques in the study of heparin-lipoprotein interactions. *Anal. Biochem.* **424**, 71–78 (2012).

137. Cilpa-Karhu, G. *et al.* Three complementary techniques for the clarification of temperature effect on low-density lipoprotein-chondroitin-6-sulfate interaction. *Anal. Biochem.* **443**, 139–147 (2013).

138. Wang, A.-J., Witos, J., D'Ulivo, L., Vainikka, K. & Riekkola, M.-L. Noncovalent poly(1-vinylpyrrolidone)-based copolymer coating for the separation of basic proteins and lipoproteins by CE. *Electrophoresis* **30**, 3939–3946 (2009).

139. Wang, A. J. *et al.* Partial filling affinity capillary electrophoresis with cationic poly(vinylpyrrolidone)-based copolymer coatings for studies on human lipoprotein-steroid interactions. *Anal. Biochem.* **399**, 93–101 (2010).

140. Witos, J. *et al.* Sugar treatment of human lipoprotein particles and their separation by capillary electrophoresis. *J. Sep. Sci.* **33**, 2528–2535 (2010).

141. Witos, J., Karesoja, M., Karjalainen, E., Tenhu, H. & Riekkola, M.-L. Surface initiated polymerization of a cationic monomer on inner surfaces of silica capillaries: Analyte separation by capillary electrophoresis

versus polyelectrolyte behavior. *J. Sep. Sci.* **36**, 1070–1077 (2013).

142. Witos, J. *et al.* Partial filling affinity capillary electrophoresis including adsorption energy distribution calculations-towards reliable and feasible biomolecular interaction studies. *Analyst* **140**, 3175–3182 (2015).

143. Zhou, S. *et al.* Carboxymethylchitosan covalently modified capillary column for open tubular capillary electrochromatography of basic proteins and opium alkaloids. *J. Chromatogr. A* **1217**, 8346–8351 (2010).

144. Gulcev, M. D., McGinitie, T. M., Bahnasy, M. F. & Lucy, C. A. Surfactant bilayer coatings in narrow-bore capillaries in capillary electrophoresis. *Analyst* **135**, 2688–2693 (2010).

145. Sebastiano, R., Mendieta, M. E., Contiello, N., Citterio, A. & Righetti, P. G. An N-methylpolyvinylpyridinium cationic polymer for capillary coating in electrophoresis of proteins and peptides. *Electrophoresis* **30**, 2313–2320 (2009).

146. Haselberg, R., de Jong, G. J. & Somsen, G. W. Capillary electrophoresis of intact basic proteins using noncovalently triple-layer coated capillaries. *J. Sep. Sci.* **32**, 2408–2415 (2009).

147. Yeung, K. K. C. & Lucy, C. A. Suppression of Electroosmotic Flow and Prevention of Wall Adsorption in Capillary Zone Electrophoresis Using Zwitterionic Surfactants. *Anal. Chem.* **69**, 3435–3441 (1997).

148. Lucy, C. A., MacDonald, A. M. & Gulcev, M. D. Non-covalent capillary coatings for protein separations in capillary electrophoresis. *Journal of Chromatography A* vol. 1184 81–105 (2008).

149. Wang, A. J. *et al.* Spermine-graft-dextran non-covalent copolymer as coating material in separation of basic proteins and neurotransmitters by capillary electrophoresis. *J. Chromatogr. A* **1217**, 5130–5136 (2010).

150. Bernal, J., Rodríguez-Meizoso, I., Elvira, C., Ibáñez, E. & Cifuentes, A. Fast and easy coating for capillary electrophoresis based on a physically adsorbed cationic copolymer. *J. Chromatogr. A* **1204**, 104–109 (2008).

151. He, Y., Wei, Y., Zheng, X. & Zheng, J. Capillary modified with covalently attached coating for enhanced CE separation of biopolymers. *Electrophoresis* **31**, 630–633 (2010).

152. Wiedmer, S. K., Andersson, T., Sündermann, M., Riekkola, M.-L. & Tenhu, H. Cationic poly(methacryl oxyethyl trimethylammonium) and its poly(ethylene glycol)-grafted analogue as capillary coating materials in electrophoresis. *J. Polym. Sci. Part B Polym. Phys.* **45**, 2655–2663 (2007).

153. Zhang, X. *et al.* Triamine-bonded stationary phase for open tubular capillary electrochromatography. *J. Sep. Sci.* **33**, 3184–3193 (2010).

154. Heintz, J., Hernandez, M. & Gomez, F. A. Use of a partial-filling technique in affinity capillary electrophoresis for determining binding constants of ligands to receptors. *J. Chromatogr. A* **840**, 261–268 (1999).

155. Nilsson, M., Johansson, G. & Isaksson, R. Determination of dissociation constants by competitive binding in partial filling capillary electrophoresis. *Electrophoresis* **25**, 1022–1027 (2004).

156. Amini, A. & Westerlund, D. Evaluation of Association Constants between Drug Enantiomers and Human α1-Acid Glycoprotein by Applying a Partial-Filling Technique in Affinity Capillary Electrophoresis. *Anal. Chem.* **70**, 1425–1430 (1998).

157. Amundsen, L. K. & Sirén, H. Determination of association constants between steroid compounds and albumins by partial-filling ACE. *Electrophoresis* **28**, 3737–3744 (2007).

158. Růžička, M. *et al.* Study of deoxyribonucleic acid-ligand interactions by partial filling affinity capillary electrophoresis. *J. Chromatogr. A* **1349**, 116–121 (2014).

159. Lipponen, K. *et al.* Partial-filling affinity capillary electrophoresis and quartz crystal microbalance with adsorption energy distribution calculations in the study of biomolecular interactions with apolipoprotein e as interaction partner. *Anal. Bioanal. Chem.* **406**, 4137–4146 (2014).

160. Ehala, S., Toman, P., Rathore, R., Makrlík, E. & Kašička, V. Affinity capillary electrophoresis and quantum mechanical calculations applied to the investigation of hexaarylbenzene-based receptor binding with lithium ion. *J. Sep. Sci.* **34**, 2433–2440 (2011).

161. Sandblad, P., Arnell, R., Samuelsson, J. & Fornstedt, T. Approach for reliable evaluation of drug proteins interactions using surface plasmon resonance technology. *Anal. Chem.* **81**, 3551–3559 (2009).

162. Tatke, S. S., Loong, C. K., D'Souza, N., Schoephoerster, R. T. & Prabhakaran, M. Large scale motions in a biosensor protein glucose oxidase: A combined approach by QENS, normal mode analysis, and molecular dynamics studies. *Biopolymers* **89**, 582–594 (2008).

163. Massolini, G., Temporini, C. & Calleri, E. Penicillin G acylase as chiral selector in LC and CE: Exploring the origins of enantioselectivity. *Journal of Chromatography B: Analytical Technologies in the Biomedical and Life Sciences* vol. 875 20–29 (2008).

164. Götmar, G., Samuelsson, J., Karlsson, A. & Fornstedt, T. Thermodynamic characterization of the adsorption of selected chiral compounds on immobilized amyloglucosidase in liquid chromatography. *J. Chromatogr. A* **1156**, 3–13 (2007).

165. Arnell, R., Ferraz, N. & Fornstedt, T. Analytical characterization of chiral drug-protein interactions: Comparison between the optical biosensor (surface plasmon resonance) assay and the HPLC perturbation method. *Anal. Chem.* **78**, 1682–1689 (2006).

166. Turner, A. P. F. Biosensors: Sense and sensibility. *Chem. Soc. Rev.* **42**, 3184–3196 (2013).

167. Thompson, M. & Hayward, G. L. Mass response of the thickness-shear mode acoustic wave sensor in liquids as a central misleading dogma. in *Proceedings of the Annual IEEE International Frequency Control Symposium* 114–119 (IEEE, 1997). doi:10.1109/freq.1997.638529.

168. Janshoff, A., Galla, H. J. & Steinem, C. Piezoelectric mass-sensing devices as biosensors - An alternative to optical biosensors? *Angewandte Chemie - International Edition* vol. 39 4004–4032 (2000).

169. Cooper, M. A. *et al.* Direct and sensitive detection of a human virus by rupture event scanning. *Nat. Biotechnol.* **19**, 833–837 (2001).

170. Pei, Y. *et al.* Photoderivatized polymer thin films at quartz crystal microbalance surfaces: Sensors for carbohydrate-protein interactions. *Anal. Chem.* **79**, 6897–6902 (2007).

171. Marx, K. A. Quartz crystal microbalance: A useful tool for studying thin polymer films and complex biomolecular systems at the solution - Surface interface. *Biomacromolecules* vol. 4 1099–1120 (2003).

172. Cooper, M. A. & Singleton, V. T. A survey of the 2001 to 2005 quartz crystal microbalance biosensor literature: Applications of acoustic physics to the analysis of biomolecular interactions. *Journal of Molecular Recognition* vol. 20 154–184 (2007).

173. Beckera, B. & Cooper, M. A. A survey of the 2006-2009 quartz crystal microbalance biosensor literature. *Journal of Molecular Recognition* vol. 24 754–787 (2011).

174. Speight, R. E. & Cooper, M. A. A Survey of the 2010 Quartz Crystal Microbalance Literature. *Journal of Molecular Recognition* vol. 25 451–473 (2012).

175. O'Neal, D., Grieve, G., Rae, D., Dragicevic, G. & Best, J. D. Factors influencing Lp[a]- particle size as determined by gradient gel electrophoresis. *J. Lipid Res.* **37**, 1655–1663 (1996).

176. Dominiczak, M. H. & Caslake, M. J. Apolipoproteins: Metabolic role and clinical biochemistry applications. *Annals of Clinical Biochemistry* vol. 48 498–515 (2011).

177. Yang, N. & Qin, Q. Apolipoprotein J: A new predictor and therapeutic target in cardiovascular disease? *Chin. Med. J. (Engl.)* **128**, 2530–2534 (2015).

178. Elovson, J. *et al.* Plasma very low density lipoproteins contain a single molecule of apolipoprotein B. *J. Lipid Res.* **29**, 1461–1473 (1988).

179. Prassl, R. & Laggner, P. Molecular structure of low density lipoprotein: current status and future challenges. *Eur. Biophys. J.* **38**, 145–158 (2009).

180. Badimon, L. & Vilahur, G. LDL-cholesterol versus HDL-cholesterol in the atherosclerotic plaque: Inflammatory resolution versus thrombotic chaos. *Ann. N. Y. Acad. Sci.* **1254.1**, 18–32 (2012).

181. Oorni, K., Pentikainen, M. O., Ala-Korpela, M. & Kovanen, P. T. Aggregation, fusion, and vesicle formation of modified low density lipoprotein particles: Molecular mechanisms and effects on matrix interactions. *Journal of Lipid Research* vol. 41 1703–1714 (2000).

182. Williams, K. J. & Tabas, I. Lipoprotein retention- and clues for atheroma regression. *Arteriosclerosis, Thrombosis, and Vascular Biology* vol. 25 1536–1540 (2005).

183. Madjid, M. *et al.* Thermal detection of vulnerable plaque. in *American Journal of Cardiology* vol. 90 L36–L39 (Elsevier Inc., 2002).

184. Sneck, M., Kovanen, P. T. & Öörni, K. Decrease in pH strongly enhances binding of native, proteolyzed, lipolyzed, and oxidized low density lipoprotein particles to human aortic proteoglycans. *J. Biol. Chem.* **280**, 37449–37454 (2005).

185. Nikolic, D. *et al.* Lipoprotein Subfractions in Metabolic Syndrome and Obesity: Clinical Significance and Therapeutic Approaches. *Nutrients* **5**, 928–948 (2013).

186. Carmena, R., Duriez, P. & Fruchart, J. C. Atherogenic lipoprotein particles in atherosclerosis. *Circulation* vol. 109 (2004).

187. Krauss, R. M. Lipoprotein subfractions and cardiovascular disease risk. *Curr. Opin. Lipidol.* **21**, 305–311 (2010).

188. Austin, M. A. *et al.* Low-Density Lipoprotein Subclass Patterns and Risk of Myocardial Infarction. *JAMA J. Am. Med. Assoc.* **260**, 1917–1921 (1988).

189. Berneis, K. K. & Krauss, R. M. Metabolic origins and clinical significance of LDL heterogeneity. *Journal of Lipid Research* vol. 43 1363–1379 (2002).

190. Rizzo, M. & Berneis, K. The Clinical Relevance of Low-Density-Lipoproteins Size Modulation by Statins. *Cardiovasc. drugs Ther.* **20**, 205–217 (2006).

191. Arai, H. *et al.* Small Dense Low-Density Lipoproteins Cholesterol can Predict Incident Cardiovascular Disease in an Urban Japanese Cohort: The Suita Study. *J. Atheroscler. Thromb.* **20**, 195–203 (2013).

192. Ai, M. *et al.* Small Dense LDL Cholesterol and Coronary Heart Disease: Results from the Framingham Offspring Study. *Clin. Chem.* **56**, 967–976 (2010).

193. Tsai, M. Y. *et al.* New automated assay of small dense low-density lipoprotein cholesterol identifies risk of coronary heart disease: The multi-ethnic study of atherosclerosis. *Arterioscler. Thromb. Vasc. Biol.* **34**, 196–201 (2014).

194. Gerber, P. A. *et al.* Small, Dense LDL Particles Predict Changes in Intima Media Thickness and Insulin Resistance in Men with Type 2 Diabetes and Prediabetes – A Prospective Cohort Study. *PLoS One* **8**, e72763 (2013).

195. Hirano, T. *et al.* Clinical Significance of Small Dense Low-Density Lipoprotein Cholesterol Levels Determined by the Simple Precipitation Method. *Arterioscler. Thromb. Vasc. Biol.* **24**, 558–563 (2004).

196. Fukushima, Y. *et al.* Small dense LDL cholesterol is a robust therapeutic marker of statin treatment in patients with acute coronary syndrome and metabolic syndrome. *Clin. Chim. Acta* **412**, 1423–1427 (2011).

197. Toledo, F. G. S., Sniderman, A. D. & Kelley, D. E. Influence of hepatic steatosis (fatty liver) on severity and composition of dyslipidemia in type 2 diabetes. *Diabetes Care* **29**, 1845–1850 (2006).

198. Cali, A. M. G. *et al.* Intrahepatic fat accumulation and alterations in lipoprotein composition in obese adolescents: A perfect proatherogenic state. *Diabetes Care* **30**, 3093–3098 (2007).

199. Chu, M., Wang, A. Y. M., Chan, I. H. S., Chui, S. H. & Lam, C. W. K. Serum small-dense LDL abnormalities in chronic renal disease patients. *Br. J. Biomed. Sci.* **69**, 99–102 (2012).

200. Berneis, K., Jeanneret, C., Muser, J., Felix, B. & Miserez, A. R. Low-density lipoprotein size and subclasses are markers of clinically apparent and non-apparent atherosclerosis in type 2 diabetes. *Metabolism.* **54**, 227–234 (2005).

201. Hirayama, S. & Miida, T. Small dense LDL: An emerging risk factor for cardiovascular disease. *Clinica Chimica Acta* vol. 414 215–224 (2012).

202. Griffin, B. A. Lipoprotein atherogenicity: an overview of current mechanisms. *Proc. Nutr. Soc.* **58**, 163–169 (1999).

203. Packard, C., Caslake, M. & Shepherd, J. The role of small, dense low density lipoprotein (LDL): A new look. in *International Journal of Cardiology* vol. 74 S17–S22 (Elsevier, 2000).

204. Steinberg, D. Modifications of low-density lipoprotein that increase its atherogenicity. *New Engl. J. Med.* **320**, 915–924 (1989).

205. Jaakkola, O. *et al.* Characteristics of low-density lipoprotein subfractions from patients with coronary artery disease. *Coron. Artery Dis.* **4**, 379–386 (1993).

206. Ohmura, H. *et al.* Lipid compositional differences of small, dense low-density lipoprotein particle influence its oxidative susceptibility: Possible implication of increased risk of coronary artery disease in subjects with phenotype B. *Metabolism.* **51**, 1081–1087 (2002).

207. Tribble, D. L. *et al.* Enhanced oxidative susceptibility and reduced antioxidant content of metabolic precursors of small, dense low-density lipoproteins. *Am. J. Med.* **110**, 103–110 (2001).

208. Anber, V., Griffin, B. A., McConnell, M., Packard, C. J. & Shepherd, J. Influence of plasma lipid and LDL-subfraction profile on the interaction between low density lipoprotein with human arterial wall proteoglycans. *Atherosclerosis* **124**, 261–271 (1996).

209. Younis, N., Charlton-Menys, V., Sharma, R., Soran, H. & Durrington, P. N. Glycation of LDL in non-diabetic people: Small dense LDL is preferentially glycated both in vivo and in vitro. *Atherosclerosis* **202**, 162–168 (2009).

210. Soran, H. & Durrington, P. N. Susceptibility of LDL and its subfractions to glycation. *Curr. Opin. Lipidol.* **22**, 254–261 (2011).

211. Griffin, B. A. *et al.* Rapid isolation of low density lipoprotein (LDL) subfractions from plasma by density gradient ultracentrifugation. *Atherosclerosis* **83**, 59–67 (1990).

212. Yee, M. S. *et al.* Lipoprotein separation in a novel iodixanol density gradient, for composition, density, and phenotype analysis. *J. Lipid Res.* **49**, 1364–1371 (2008).

213. Davies, I. G., Graham, J. M. & Griffin, B. A. Rapid Separation of LDL Subclasses by Iodixanol Gradient Ultracentrifugation. *Clin. Chem.* **49**, 1865–1872 (2003).

214. Ensign, W., Hill, N. & Heward, C. B. Disparate LDL Phenotypic Classification among 4 Different Methods Assessing LDL Particle Characteristics. *Clin. Chem.* **52**, 1722–1727 (2006).

215. Krauss, R. M. & Burke, D. J. Identification of multiple subclasses of plasma low density lipoproteins in normal humans. *J. Lipid Res.* **23**, 97–104 (1982).

216. Okazaki, M. *et al.* Identification of unique lipoprotein subclasses for visceral obesity by component analysis of cholesterol profile in high-performance liquid chromatography. *Arterioscler. Thromb. Vasc. Biol.* **25**, 578–584 (2005).

217. Sakurai, T. *et al.* Measurement of lipoprotein particle sizes using dynamic light scattering. *Ann. Clin. Biochem.* **47**, 476–481 (2010).

218. Caulfield, M. P. *et al.* Direct Determination of Lipoprotein Particle Sizes and Concentrations by Ion Mobility Analysis. *Clin. Chem.* **54**, 1307–1316 (2008).

219. Otvos, J. D., Jeyarajah, E. J., Bennett, D. W. & Krauss, R. M. Development of a Proton Nuclear Magnetic Resonance Spectroscopic Method for Determining Plasma Lipoprotein Concentrations and Subspecies Distributions from a Single, Rapid Measurement. *Clin. Chem.* **38**, 1632–1638 (1992).

220. Witte, D. R. *et al.* Study of agreement between LDL size as measured by nuclear magnetic resonance and gradient gel electrophoresis. *J. Lipid Res.* **45**, 1069–1076 (2004).

221. Hoefner, D. M. *et al.* Development of a Rapid, Quantitative Method for LDL Subfractionation with Use of the Quantimetrix Lipoprint LDL System. *Clin. Chem.* **47**, 266–274 (2001).

222. Ito, Y., Fujimura, M., Ohta, M. & Hirano, T. Development of a Homogeneous Assay for Measurement of Small Dense LDL Cholesterol. *Clin. Chem.* **57**, 57–65 (2011).

223. Albers, J. J., Kennedy, H. & Marcovina, S. M. Evaluation of a new homogenous method for detection of small dense LDL cholesterol: Comparison with the LDL cholesterol profile obtained by density gradient ultracentrifugation. *Clin. Chim. Acta* **412**, 556–561 (2011).

224. Théry, C. *et al.* Minimal information for studies of extracellular vesicles 2018 (MISEV2018): a position statement of the International Society for Extracellular Vesicles and update of the MISEV2014 guidelines. *J. Extracell. Vesicles* **7**, 1535750 (2018).

225. Colombo, M., Raposo, G. & Théry, C. Biogenesis, Secretion, and Intercellular Interactions of Exosomes and Other Extracellular Vesicles. *Annu. Rev. Cell Dev. Biol.* **30**, 255–289 (2014).

226. Yáñez-Mó, M. *et al.* Biological properties of extracellular vesicles and their physiological functions. *J. Extracell. Vesicles* **4**, 27066 (2015).

227. Zijlstra, A. & Di Vizio, D. Size matters in nanoscale communication. *Nat. Cell Biol.* **20**, 228–230 (2018).

228. Cheng, L., Zhao, W. & Hill, A. F. Exosomes and their role in the intercellular trafficking of normal and disease associated prion proteins. *Molecular Aspects of Medicine* vol. 60 62–68 (2018).

229. Meldolesi, J. Exosomes and Ectosomes in Intercellular Communication. *Current Biology* vol. 28 R435–R444 (2018).

230. Raposo, G. & Stahl, P. D. Extracellular vesicles: a new communication paradigm? *Nat. Rev. Mol. Cell Biol.* **20**, 509–510 (2019).

231. Konoshenko, M. Y., Lekchnov, E. A., Vlassov, A. V. & Laktionov, P. P. Isolation of Extracellular Vesicles: General Methodologies and Latest Trends. *BioMed Research International* vol. 2018 (2018).

232. Marleau, A. M., Chen, C. S., Joyce, J. A. & Tullis, R. H. Exosome removal as a therapeutic adjuvant in cancer. *J. Transl. Med.* **10**, 1–12 (2012).

233. Semple, J. W., Italiano, J. E. & Freedman, J. Platelets and the immune continuum. *Nat. Rev. Immunol.* **11**, 264–274 (2011).

234. Koupenova, M., Clancy, L., Corkrey, H. A. & Freedman, J. E. Circulating platelets as mediators of immunity, inflammation, and thrombosis. *Circulation Research* vol. 122 337–351 (2018).

235. van der Meijden, P. E. & Heemskerk, J. W. . Platelet biology and functions: new concepts and clinical perspectives. *Nat. Rev. Cardiol.* **16**, 166–179 (2019).

236. Selvadurai, M. V. & Hamilton, J. R. Structure and function of the open canalicular system–the platelet's specialized internal membrane network. *Platelets* vol. 29 319–325 (2018).

237. Ambrosio, A. L. & Di Pietro, S. M. Storage pool diseases illuminate platelet dense granule biogenesis. *Platelets* vol. 28 138–146 (2017).

238. Flaumenhaft, R. & Sharda, A. The life cycle of platelet granules. *F1000Research* vol. 7 (2018).

239. Chen, Y., Yuan, Y. & Li, W. Sorting machineries: How platelet-dense granules differ from α-granules. *Bioscience Reports* vol. 38 (2018).

240. Melki, I., Tessandier, N., Zufferey, A. & Boilard, E. Platelet microvesicles in health and disease. *Platelets* vol. 28 214–221 (2017).

241. Ridger, V. C. *et al.* Microvesicles in vascular homeostasis and diseases position paper of the european society of cardiology (ESC) working group on atherosclerosis and vascular biology. *Thromb. Haemost.* **117**,

1296–1316 (2017).

242. Garcia, B. A. *et al.* The platelet microparticle proteome. *J. Proteome Res.* **4**, 1516–1521 (2005).
243. Vasina, E. M. *et al.* Microparticles from apoptotic platelets promote resident macrophage differentiation. *Cell Death Dis.* **2**, e211–e211 (2011).
244. Arraud, N. *et al.* Extracellular vesicles from blood plasma: Determination of their morphology, size, phenotype and concentration. *J. Thromb. Haemost.* **12**, 614–627 (2014).
245. Antwi-Baffour, S. *et al.* Understanding the biosynthesis of platelets-derived extracellular vesicles. *Immunity, Inflamm. Dis.* **3**, 133–140 (2015).
246. Agbani, E. O. & Poole, A. W. Procoagulant platelets: Generation, function, and therapeutic targeting in thrombosis. *Blood* vol. 130 2171–2179 (2017).
247. Heijnen, H. F. *et al.* Multivesicular bodies are an intermediate stage in the formation of platelet alpha-granules. *Blood* **91**, 2313–25 (1998).
248. Dean, W. L., Lee, M. J., Cummins, T. D., Schultz, D. J. & Powell, D. W. Proteomic and functional characterisation of platelet microparticle size classes. *Thromb. Haemost.* **102**, 711–718 (2009).
249. Wei, H., Malcor, J. D. M. & Harper, M. T. Lipid rafts are essential for release of phosphatidylserine-exposing extracellular vesicles from platelets. *Sci. Rep.* **8**, 1–11 (2018).
250. Aatonen, M. T. *et al.* Isolation and characterization of platelet-derived extracellular vesicles. *J. Extracell. Vesicles* **3**, 24692 (2014).
251. Plé, H. *et al.* The Repertoire and Features of Human Platelet microRNAs. *PLoS One* **7**, e50746 (2012).
252. Lannan, K. L. *et al.* Breaking the mold: Transcription factors in the anucleate platelet and platelet-derived microparticles. *Frontiers in Immunology* vol. 6 48 (2015).
253. Weisser, N. E. & Hall, J. C. Applications of single-chain variable fragment antibodies in therapeutics and diagnostics. *Biotechnology Advances* vol. 27 502–520 (2009).
254. Zheng, X. *et al.* Analysis of biomolecular interactions using affinity microcolumns: A review. *Journal of Chromatography B: Analytical Technologies in the Biomedical and Life Sciences* vol. 968 49–63 (2014).
255. Sproß, J. & Sinz, A. Monolithic media for applications in affinity chromatography. *J. Sep. Sci.* **34**, 1958–1973 (2011).
256. Lipman, N. S., Jackson, L. R., Trudel, L. J. & Weis-Garcia, F. Monoclonal Versus Polyclonal Antibodies: Distinguishing Characteristics, Applications, and Information Resources. *ILAR J.* **46**, 258–268 (2005).
257. Urh, M., Simpson, D. & Zhao, K. Chapter 26 Affinity Chromatography. General Methods. *Methods in Enzymology* vol. 463 417–438 (2009).
258. Schiel, J. E. & Hage, D. S. Kinetic studies of biological interactions by affinity chromatography. *J. Sep. Sci.* **32**, 1507–1522 (2009).
259. González-González, M., González-Valdez, J., Mayolo-Deloisa, K. & Rito-Palomares, M. Monolithic chromatography: insights and practical perspectives. *J. Chem. Technol. Biotechnol.* **92**, 9–13 (2017).
260. Svec, F. & Lv, Y. Advances and recent trends in the field of monolithic columns for chromatography. *Analytical Chemistry* vol. 87 250–273 (2015).
261. Podgornik, A. Š., Yamamoto, S., Peterka, M. Ž. & Krajnc, N. L. Fast separation of large biomolecules using short monolithic columns. *Journal of Chromatography B: Analytical Technologies in the Biomedical and Life Sciences* vol. 927 80–89 (2013).
262. Jungbauer, A. & Hahn, R. Polymethacrylate monoliths for preparative and industrial separation of biomolecular assemblies. *Journal of Chromatography A* vol. 1184 62–79 (2008).
263. Wu, N. & Clausen, A. M. Fundamental and practical aspects of ultrahigh pressure liquid chromatography for fast separations. *Journal of Separation Science* vol. 30 1167–1182 (2007).
264. Tennikova, T. B. & Freitag, R. An Introduction to Monolithic Disks as Stationary Phases for High Performance Biochromatography. *J. High Resolut. Chromatogr.* **23**, 27–38 (2000).
265. Kumar, A. & Srivastava, A. Cell separation using cryogel-based affinity chromatography. *Nat. Protoc.* **5**, 1737–1747 (2010).
266. Martin, C., Coyne, J. & Carta, G. Properties and performance of novel high-resolution/high-permeability ion-exchange media for protein chromatography. in *Journal of Chromatography A* vol. 1069 43–52 (Elsevier, 2005).
267. Schachermeyer, S. & Zhong, W. Flow field-flow fractionation: Analysis of biomolecules and their complexes. in *Field-Flow Fractionation in Biopolymer Analysis* 127–138 (Springer-Verlag Wien, 2012). doi:10.1007/978-3-7091-0154-4_9.
268. Nilsson, M. *et al.* Determination of protein-ligand affinity constants from direct migration time in capillary electrophoresis. *Electrophoresis* **25**, 1829–1836 (2004).
269. Sauerbrey, G. Wagung dunner Schichten mit Schwingquarzen. *Angew. Chemie-International Ed.* **69**, 761–761 (1957).
270. Sauerbrey, G. Verwendung von Schwingquarzen zur Wägung dünner Schichten und zur Mikrowägung. *Zeitschrift für Phys.* **155**, 206–222 (1959).
271. Vashist, S. K. & Vashist, P. Recent advances in quartz crystal microbalance-based sensors. *Journal of Sensors* vol. 2011 (2011).
272. Huang, X., Bai, Q., Hu, J. & Hou, D. A Practical Model of Quartz Crystal Microbalance in Actual Applications. *Sensors* **17**, 1785 (2017).
273. Dubiel, E. A., Martin, B., Vigier, S. & Vermette, P. Real-time label-free detection and kinetic analysis of Etanercept—Protein A interactions using quartz crystal microbalance. *Colloids Surfaces B Biointerfaces* **149**, 312–321 (2017).
274. Forssén, P. *et al.* Reliable Strategy for Analysis of Complex Biosensor Data. *Anal. Chem.* **90**, 5366–5374 (2018).
275. Liangsupree, T. *et al.* Rapid affinity chromatographic isolation method for LDL in human plasma by immobilized chondroitin-6-sulfate and anti-apoB-100 antibody monolithic disks in tandem. *Sci. Rep.* **9**, 11235 (2019).
276. Forssen, P., Samuelsson, J., Lacki, K. & Fornstedt, T. Advanced analysis of biosensor data for SARS-COV-2 RBD and ACE2 interactions. *Anal. Chem.* **92**, 11520–11524 (2020).

277. Haynes, W. CRC handbook of chemistry and physics. *CRC Press* (2014).
278. Havel, R. J., Eder, H. A. & Bragdon, J. H. The distribution and chemical composition of ultracentrifugally separated lipoproteins in human serum. *J. Clin. Invest.* **34**, 1345–1353 (1955).
279. Radding, C. M., Steinberg, D., Allen, J. C. & Baxter, J. H. Studies on the synthesis and secretion of serum lipoproteins by rat liver slices. *J. Clin. Invest.* **39**, 1560–1569 (1960).
280. Lipponen, K., Tähkä, S., Kostiainen, M. & Riekkola, M.-L. Stable neutral double hydrophilic block copolymer capillary coating for capillary electrophoretic separations. *Electrophoresis* **35**, 1106–1113 (2014).
281. Williams, B. A. & Vigh, G. Fast, accurate mobility determination method for capillary electrophoresis. *Anal. Chem.* **68**, 1174–1180 (1996).
282. Hellqvist, A., Hedeland, Y. & Pettersson, C. Evaluation of electroosmotic markers in aqueous and nonaqueous capillary electrophoresis. *Electrophoresis* **34**, 3252–3259 (2013).
283. Rico, E., González, O., Blanco, M. E. & Alonso, R. M. Evaluation of human plasma sample preparation protocols for untargeted metabolic profiles analyzed by UHPLC-ESI-TOF-MS. *Anal. Bioanal. Chem.* **406**, 7641–7652 (2014).
284. Yoshida, K., Horii, K., Fujii, Y. & Nishio, I. Real-Time Observation of Liposome Bursting Induced by Acetonitrile. *ChemPhysChem* **15**, 2909–2912 (2014).
285. Helin, A. *et al.* Characterization of free amino acids, bacteria and fungi in size-segregated atmospheric aerosols in boreal forest: seasonal patterns, abundances and size distributions. *Atmos. Chem. Phys* **17**, 13089–13101 (2017).
286. Lowry, O. H., Rosebrough, N. J., Farr, A. L. & Randall, R. J. Protein measurement with the Folin phenol reagent. *J. Biol. Chem.* **193**, 265–275 (1951).
287. Smith, P. K. *et al.* Measurement of protein using bicinchoninic acid. *Anal. Biochem.* **150**, 76–85 (1985).
288. Puhka, M. *et al.* KeepEX, a simple dilution protocol for improving extracellular vesicle yields from urine. *Eur. J. Pharm. Sci.* **98**, 30–39 (2017).
289. Svitel, J., Balbo, A., Mariuzza, R. A., Gonzales, N. R. & Schuck, P. Combined affinity and rate constant distributions of ligand populations from experimental surface binding kinetics and equilibria. *Biophys. J.* **84**, 4062–4077 (2003).
290. Altschuh, D. *et al.* Deciphering complex protein interaction kinetics using Interaction Map. *Biochem. Biophys. Res. Commun.* **428**, 74–79 (2012).
291. Fang, N., Zhang, H., Li, J., Li, H. W. & Yeung, E. S. Mobility-based wall adsorption isotherms for comparing capillary electrophoresis with single-molecule observations. *Anal. Chem.* **79**, 6047–6054 (2007).
292. Do, D. D. *Adsorption Analysis: Equilibria and Kinetics. Series on Chemical Engineering* vol. 2 (1998).
293. Guiochon, G., Felinger, A. & Shirazi, D. *Fundamentals of preparative and nonlinear chromatography*. (Academic Press, 2006).
294. Agmo Hernández, V., Samuelsson, J., Forssén, P. & Fornstedt, T. Enhanced interpretation of adsorption data generated by liquid chromatography and by modern biosensors. *J. Chromatogr. A* **1317**, 22–31 (2013).
295. Stanley, B. J. & Guiochon, G. Numerical Estimation of Adsorption Energy Distributions from Adsorption Isotherm Data with the Expectation-Maximization Method. *J. Phys. Chem.* **97**, 8098–8104 (1993).
296. Shuman, C. F., Hämäläinen, M. D. & Danielson, U. H. Kinetic and thermodynamic characterization of HIV-1 protease inhibitors. *J. Mol. Recognit.* **17**, 106–119 (2004).
297. R Core Team. R: A language and environment for statistical computing. (2019).
298. Gan, N. *et al.* Tailor-made approach for selective isolation and elution of low-density lipoproteins by immunoaffinity sorbent on silica. *Anal. Biochem.* **514**, 12–23 (2016).
299. Lu, M. & Gursky, O. Aggregation and fusion of low-density lipoproteins in vivo and in vitro. *Biomolecular Concepts* vol. 4 501–518 (2013).
300. Hyötyläinen, T. & Riekkola, M. L. Approaches for on-line coupling of extraction and chromatography. *Analytical and Bioanalytical Chemistry* vol. 378 1962–1981 (2004).
301. Sódar, B. W. *et al.* Low-density lipoprotein mimics blood plasma-derived exosomes and microvesicles during isolation and detection. *Sci. Rep.* **6**, 1–12 (2016).
302. Witwer, K. W. & Théry, C. Extracellular vesicles or exosomes? On primacy, precision, and popularity influencing a choice of nomenclature. *Journal of Extracellular Vesicles* vol. 8 (2019).
303. Kowal, J. *et al.* Proteomic comparison defines novel markers to characterize heterogeneous populations of extracellular vesicle subtypes. *Proc. Natl. Acad. Sci. U. S. A.* **113**, E968-77 (2016).
304. Ramirez, M. I. *et al.* Technical challenges of working with extracellular vesicles. *Nanoscale* vol. 10 881–906 (2018).
305. Inuzuka, M., Hayakawa, M. & Ingi, T. Serine, an activity-regulated protein family, incorporates serine into membrane lipid synthesis. *J. Biol. Chem.* **280**, 35776–35783 (2005).
306. Skotland, T., Hessvik, N. P., Sandvig, K. & Llorente, A. Exosomal lipid composition and the role of ether lipids and phosphoinositides in exosome biology. *Journal of Lipid Research* vol. 60 9–18 (2019).
307. Dardevet, D. The molecular nutrition of amino acids and proteins: a volume in the molecular nutrition series. (2016).
308. Li, P., Yin, Y.-L., Li, D., Kim, S. W. & Wu, G. Amino acids and immune function. *Br. J. Nutr.* **98(2)**, 237–252 (2007).
309. Zhong, Z., Wheeler, M., Li, X., … M. F.-C. O. in & 2003, L-Glycine: a novel antiinflammatory, immunomodulatory, and cytoprotective agent. *Curr. Opin. Clin. Nutr. Metab. Care* **6(2)**, 229–240 (2003).